Advanced Steel Construction

an international journal

ISSN 1816-112X

Science Citation Index Expanded, Materials Science Citation Index and ISI Alerting

EDITORS-IN-CHIEF

Asian Pacific, African and organizing Editor
S.L. Chan
The Hong Kong Polyt. Univ., Hong Kong

American Editor
W.F. Chen
Univ. of Hawaii at Manoa, USA

European Editor
R. Zandonini
Trento Univ., Italy

INTERNATIONAL EDITORIAL BOARD

F.G. Albermani
The Univ. of Queensland, Australia

F.S.K. Bijlaard
Delft Univ. of Technology, The Netherlands

R. Bjorhovde
The Bjorhovde Group, USA

M.A. Bradford
The Univ. of New South Wales, Australia

D. Camotim
Technical Univ. of Lisbon, Portugal

C.M. Chan
Hong Kong Univ. of Science & Technology, Hong Kong

S.P. Chiew
Nanyang Technological Univ., Singapore

W.K. Chow
The Hong Kong Polyt. Univ., Hong Kong

K.F. Chung
The Hong Kong Polyt. Univ., Hong Kong

G.G. Deierlein
Stanford Univ., California, USA

L. Dezi
Univ. of Ancona, Italy

D. Dubina
The Politehnica Univ. of Timosoara, Romania

R. Greiner
Technical Univ. of Graz, Austria

G.W.M. Ho
Ove Arup & Partners Hong Kong Ltd., Hong Kong

B.A. Izzuddin
Imperial College of Science, Technology and Medicine, UK

J.P. Jaspart
Univ. of Liege, Belgium

S. A. Jayachandran
SERC, CSIR, Chennai, India

S. Kitipornchai
City Univ. of Hong Kong, Hong Kong

D. Lam
Univ. of Leeds, UK

G.Q. Li
Tongji Univ., China

J.Y.R. Liew
National Univ. of Singapore, Singapore

X. Liu
Tsinghua Univ., China

E.M. Lui
Syracuse Univ., USA

Y.L. Mo
Univ. of Houston, USA

J.P. Muzeau
CUST, Clermont Ferrand, France

D.A. Nethercot
Imperial College of Science, Technology and Medicine, UK

D.J. Oehlers
The Univ. of Adelaide, Australia

K. Rasmussen
The Univ. of Sydney, Australia

T.M. Roberts
Cardiff Univ., UK

J.M. Rotter
The Univ. of Edinburgh, UK

C. Scawthorn
Scawthorn Porter Associates, USA

P. Schaumann
Univ. of Hannover, Germany

G.P. Shu
Southeast Univ. China

J.G. Teng
The Hong Kong Polyt. Univ., Hong Kong

G.S. Tong
Zhejiang Univ., China

K.C. Tsai
National Taiwan Univ., Taiwan

C.M. Uang
Univ. of California, USA

B. Uy
University of Western Sydney

M. Veljkovic
Univ. of Lulea, Sweden

F. Wald
Czech Technical Univ. in Prague, Czech

Y.C. Wang
The Univ. of Manchester, UK

D. White
Georgia Institute of Technology, USA

E. Yamaguchi
Kyushu Institute of Technology, Japan

Y.B. Yang
National Taiwan Univ., Taiwan

B. Young
The Univ. of Hong Kong, Hong Kong

X.L. Zhao
Monash Univ., Australia

Cover: Skylight at MGM, Macau, China
designed by second-order $P\text{-}\Delta\text{-}\delta$ analysis without assumption of effective length

General Information
Advanced Steel Construction, an international journal

Aims and scope

The International Journal of Advanced Steel Construction provides a platform for the publication and rapid dissemination of original and up-to-date research and technological developments in steel construction, design and analysis. Scope of research papers published in this journal includes but is not limited to theoretical and experimental research on elements, assemblages, systems, material, design philosophy and codification, standards, fabrication, projects of innovative nature and computer techniques. The journal is specifically tailored to channel the exchange of technological know-how between researchers and practitioners. Contributions from all aspects related to the recent developments of advanced steel construction are welcome.

Instructions to authors

Submission of the manuscript. Authors may submit double-spaced manuscripts preferably in MS Word by emailing to one of the chief editors as follows for arrangement of review. Alternatively papers can be submitted on a diskette to one of the chief editors.

Asian Pacific , African and organizing editor : Professor S.L. Chan, Email: ceslchan@polyu.edu.hk
American editor : Professor W.F. Chen, Email: waifah@hawaii.edu
European editor : Professor R. Zandonini, Email: riccardo_zandonini@ing.unitn.it

All manuscripts submitted to the journal are recommended to accompany with a list of four potential reviewers suggested by the author(s). This list should include the complete name, address, telephone and fax numbers, email address, and at least five keywords that identify the expertise of each reviewer. This scheme will improve the process of review.

Style of manuscript

General. Author(s) should provide full postal and email addresses and fax number for correspondence. The manuscript including abstract, keywords, references, figures and tables should be in English with pages numbered and typed with double line spacing on single side of A4 or letter-sized paper. The front page of the article should contain:

a) a short title (reflecting the content of the paper);
b) all the name(s) and postal and email addresses of author(s) specifying the author to whom correspondence and proofs should be sent;
c) an abstract of 100-200 words; and
d) 5 to 8 keywords.

The paper must contain an introduction and a conclusion. The length of paper should not exceed 25 journal pages (approximately 15,000 words equivalents).

Tables and figures. Tables and figures including photographs should be typed, numbered consecutively in Arabic numerals and with short titles. They should be referred in the text as Figure 1, Table 2, etc. Originally drawn figures and photographs should be provided in a form suitable for photographic reproduction and reduction in the journal.

Mathematical expressions and units. The Systeme Internationale (SI) should be followed whenever possible. The numbers identifying the displayed mathematical expression should be referred to in the text as Eq. (1), Eq. (2).

References. References to published literature should be referred in the text, in the order of citation with Arabic numerals, by the last name(s) of the author(s) (e.g. Zandonini and Zanon [3]) or if more than three authors (e.g. Zandonini et al. [4]). References should be in English with occasional allowance of 1-2 exceptional references in local languages and reflect the current state-of-technology. Journal titles should be abbreviated in the style of the Word List of Scientific Periodicals. References should be cited in the following style [1, 2, 3].

Journal: [1] Chen, W.F. and Kishi, N., "Semi-rigid Steel Beam-to-column Connections, Data Base and Modelling", Journal of Structural Engineering, ASCE, 1989, Vol. 115, No. 1, pp. 105-119.
Book: [2] Chan, S.L. and Chui, P.P.T., "Non-linear Static and Cyclic Analysis of Semi-rigid Steel Frames", Elsevier Science, 2000.
Proceedings: [3] Zandonini, R. and Zanon, P., "Experimental Analysis of Steel Beams with Semi-rigid Joints", Proceedings of International Conference on Advances in Steel Structures, Hong Kong, 1996, Vol. 1, pp. 356-364.

Proofs. Proof will be sent to the corresponding author to correct any typesetting errors. Alternations to the original manuscript at this stage will not be accepted. Proofs should be returned within 48 hours of receipt by Express Mail, Fax or Email.

Copyright. Submission of an article to "Advanced Steel Construction" implies that it presents the original and unpublished work, and not under consideration for publication nor published elsewhere. On acceptance of a manuscript submitted, the copyright thereof is transferred to the publisher by the Transfer of Copyright Agreement and upon the acceptance of publication for the papers, the corresponding author must sign the form for Transfer of Copyright.

Permission. Quoting from this journal is granted provided that the customary acknowledgement is given to the source.

Page charge and Reprints. There will be no page charges if the length of paper is within the limit of 25 journal pages. A total of 30 free offprints will be supplied free of charge to the corresponding author. Purchasing orders for additional offprints can be made on order forms which will be sent to the authors. These instructions can be obtained at the Hong Kong Institute of Steel Construction, Journal website: http://www.hkisc.org

The International Journal of Advanced Steel Construction is published quarterly by non-profit making learnt society, The Hong Kong Institute of Steel Construction, c/o Department of Civil & Structural Engineering, The Hong Kong Polytechnic University, Hung Hom, Kowloon, Hong Kong.

Subscription inquiries and change of address. Address all subscription inquiries and correspondence to Member Records, IJASC. Notify an address change as soon as possible. All communications should include both old and new addresses with zip codes and be accompanied by a mailing label from a recent issue. Allow six weeks for all changes to become effective.

The Hong Kong Institute of Steel Construction
HKISC
c/o Department of Civil and Structural Engineering,
The Hong Kong Polytechnic University,
Hunghom, Kowloon, Hong Kong, China.
Tel: 852- 2766 6047 Fax: 852- 2334 6389
Email: *ceslchan@polyu.edu.hk* Website: *http://www.hkisc.org/*
ISSN 1816-112X
Science Citation Index Expanded, Materials Science Citation Index and ISI Alerting

ISSN 1816-112X

Science Citation Index Expanded, Materials Science Citation Index and ISI Alerting

Advanced Steel Construction

an international journal

VOLUME 5 NUMBER 2 JUNE 2009

Technical Papers (Special Issue)

Conference Announcements

GUEST EDITORIAL

R G Beale, BSc, PhD
Department of Mechanical Engineering, Oxford Brookes University, Oxford, UK

The papers in this special edition are extended versions of eight of the papers presented at the Sixth International Conference on Steel and Aluminium Structures (ICSAS'07) held at St Catherine's College, Oxford, UK between June 24th-27th July. At the conference 137 papers were presented by authors from . The conference series takes place every four years and has been held in Finland and Australia. The next one will take place in Malaysia in 2011.

All the papers in this special edition were selected by members of the UK Committee for the conference and were reviewed by the normal procedures for the journal. Of the eight papers two of them refer to aluminium structures but the principles contained therein are applicable to steel structures. The paper by Maljaars and Soetens details experimental and computational analyses of aluminium structures exposed to fire with particular concentration on the heat affected zone. The paper by de Matteis et al describes the experimental verification of an aluminium shear panel which is designed to be used as a method of protecting medium rise structures against seismic actions. The papers by Dubina et al, Gehring and Saal, and Ádány et al are concerned with thin-walled steel structures, their production and analysis especially with regard to the influence of imperfections. The paper by Melcher et al is concerned with applying reliability theory to obtain estimates of the resistance of steel girders to imperfections. The final paper by Lopéz-Castro et al is concerned with estimating springback after forming loads are released.

BRACING TYPE PURE ALUMINIUM STIFFENED SHEAR PANELS: AN EXPERIMENTAL STUDY

Gianfranco De Matteis[1,*], Giuseppe Brando[1], Simeone Panico[2] and Federico M. Mazzolani[2]

[1] *Department of Design Rehabilitation and Control of Architectural Structures (PRICOS), University of Chieti-Pescara "G d'Annunzio", Italy*
[2] *Department of Engineering Structures (DIST), University of Naples "Federico II" , Italy*
**(Corresponding author: E-mail: demattei@unina.it)*

ABSTRACT: Shear panels represent nowadays one of the most suitable devices for protecting steel medium-high rise buildings subjected to both seismic and aeolian actions. In particular, the employment of stiffened plates made of low yield strength material provides an effective dissipative capability to the whole structure, which can be controlled as a design parameter by choosing appropriate panel dimensions and varying the stiffeners arrangement. The main purpose of this paper is to illustrate the principal results of an experimental campaign carried out on two bracing type pure aluminium shear panels (BTPASPs) tested under a diagonal cyclic force. Selected specimens are stiffened by means of welded aluminium ribs and are characterized by different aspect ratio values. A comparison between the obtained structural responses, in terms of experimental evidences, energy dissipation capability, hardening ratio, secant global stiffness and equivalent viscous damping ratio, is provided.

Keywords: Pure aluminium, shear panels, dissipative devices, passive seismic control, cyclic response, FEM model

---

1. INTRODUCTORY REMARKS

The use of passive energy dissipation (PED) metallic devices, placed in the primary framed structures of both steel and r.c. medium-high buildings for their protection during a seismic event, has found a lot of application in the last few decades. Among these, shear panels represent one of the most suitable tool to improve the structural performance in terms of both energy dissipation capability and lateral stiffness (Dargush and Soong [1]). In fact, the possibility of exploiting their effective post-buckling behaviour, which develops by means of a tension field shear mechanism, allows to get benefit from the ductile feature of the base material. In addition, the dissipative capability of these devices can be improved by using a low yield strength base material and applying adequate flexural stiffeners to the basic plate in order to have a very good hysteretic behaviour, with the energy dissipation function activated already for very small drift angles and pinching effects arising only when high plastic shear strain demands occur. Furthermore, it has to be considered that due to moderate initial shear stiffnesses, these systems could also improve the global structural performances with reference to the serviceability limit state requirements.

Many researches have been performed in order to find suitable analytical and physical hysteretic models able to simulate the dissipative features of stiffened shear plates (Chen et al. [2]). However, the main efforts have been devoted to solve two crucial aspects. The former concerns the technological choice of a base material characterized by a low yielding point, in such a way, consistently with the "capacity design" criteria, hysteretic properties of dampers could be activated when the primary structure is still in the elastic field. The latter is related to the pursuit of design charts finalized to optimise the geometry of the device in terms of type and location of the stiffeners. From both these points of view, the studies carried out in Japan in the earlier nineties should be mentioned (Nakashima [3-5]). In particular, the choice of a steel with a low carbon content, characterized by both a low yield stress point and a high ductility value, has been proposed, leading to the use of the well known LYSW (Low Yield Strength Wall) devices.

On the other hand, this type of material is not produced and commercialised in the European market and research of alternative solutions has been carried out. In particular, an innovative type of full-bay shear panels (see Figure 1-a and Figure 1-b) made of pure aluminium alloy as base material has been recently proposed at the University of Naples “Federico II”, where several studies, from both the experimental (De Matteis et al. [6]) and the numerical (De Matteis et al. [7 – 8]) points of view, have been implemented. Such a material is characterized by a nominal yield strength significantly lower than the LYS steel, with a similar elongation at rupture, provided that preliminarily heat treatment processes are applied. The obtained results have shown a very attractive performance, with a high dissipative capability, which is testified by the large hysteretic cycles obtained. From the other hand, some slipping phenomena for low lateral displacement values have been observed limiting the performance of the systems.

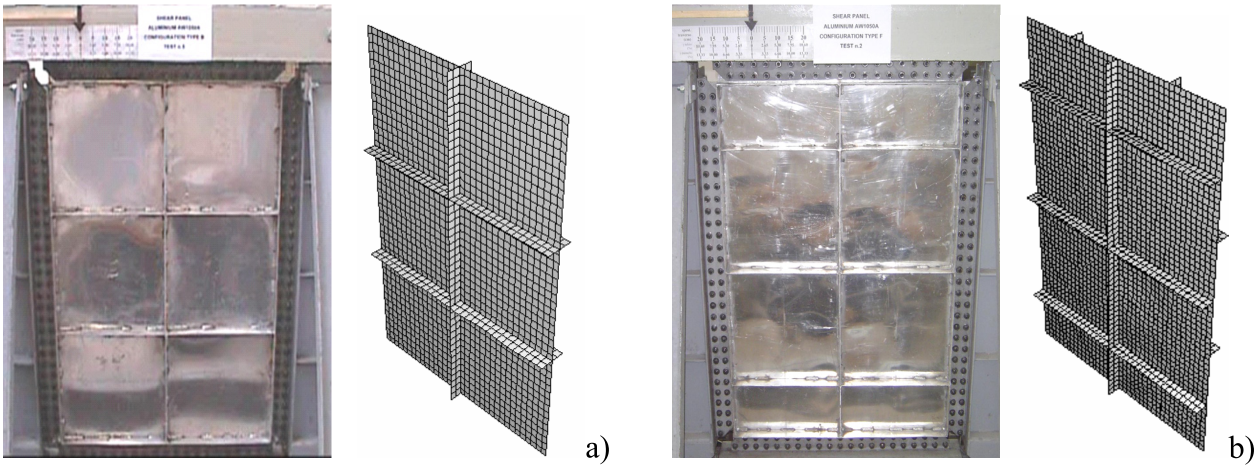
a) b)

Figure 1. Experimental and Numerical Models of Tested Full-bay Pure Aluminium Shear Panels

In order to increase the local deformation demand of shear panels for reduced inter-story drifts of the primary framed structure, exploiting the high ductility of the base material, the bracing type configuration of shear panel has been adopted (see Figure 2). It is characterised by reduced dimensions of shear panels respect to the surrounding frame field, so to increase the ratio between the shear deformation of the panel and the developed interstory drift.

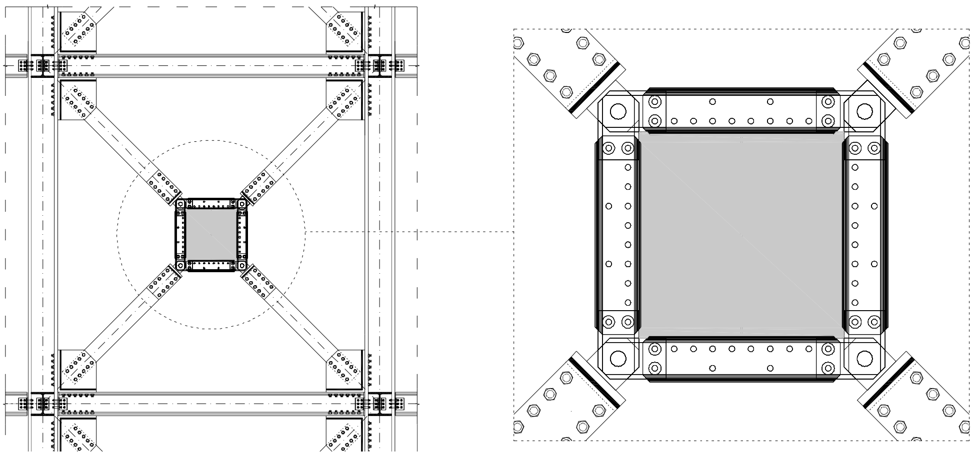

Figure 2. Bracing Type Shear Panel Configuration

Bracing type pure aluminium shear panels (BTPASPs) may therefore be effectively used as passive protection device in both steel and r.c. moment resisting frames. In order to evaluate the influence of the main geometrical parameters on the cyclic behaviour, two shear panel specimens characterises by different aspect ratio values have been experimentally tested by applying a diagonal cyclic loading procedure. The main obtained results and the experimental evidences of the tests are shown in the current paper.

2. THE PROPOSED SYSTEMS

2.1 Basis

The innovative aspects of the proposed material, which is an alloy characterized by a high percentage of pure aluminium never employed before in the structural engineering field, lead to a deep investigation of its mechanical features with the aim of attaining a better knowledge of its behaviour for both monotonic and cyclic loading.

On the other hand, as far as the design process of the shear panels is concerned, the choice of stiffener configuration represents a key aspect to determine the device performance. In fact, a shear plate where ribs are correctly arranged provides a better hysteretic behaviour, the response of the system being mainly characterised, at least for a huge part of the plastic field, by a pure shear resistant mechanism. Moreover the flexural stiffness of the stiffeners must be set in appropriate way, so that global buckling phenomena, which negatively influence the system response, do not occur. On the basis of the above considerations, a study based on a twofold approach has been developed: (1) inspection of the mechanical behaviour of the base material, (2) investigation on the most appropriate stiffener configuration to be adopted in relation to the expected structural demand.

2.2 The Adopted Material

The tested bracing type pure aluminium shear panels have been fabricated with plates and stiffeners made of aluminium alloy AW1050 A H24, having a thickness of 5 mm. The chemical composition and nominal mechanical properties of the adopted material are listed in Table 1.

Table 1. Chemical Composition and Mechanical Properties of the Adopted Aluminium Alloy 1050A H24

Commercial denomination		**Impurities**
Aluminium 99.50%		0.02%Cu, 0.40%Fe, 0.31%Si, 0.07%Zn, o.o2%Tl, 0.02%other
	Mechanical properties	
Tensile Strength [Mpa]	Yield Strength [0.2% offset, MPA]	Elongation on 5cm [%]
70-100	30-70	20-40

Preliminary uniaxial tensile tests have been performed according to the specifications provided by RILEM [9]. The obtained results (De Matteis et al. [6]) have shown a higher conventional yielding strength (f_{02}) and a lower ductility than the nominal ones. To enhance the desirable ductile property and reduce the yield stress, a heat treatment process has been therefore carried out. The specimens have been submitted to a cycle of heat treatment characterized by different phases with constant temperature, each one having a duration of four hours. Successive tensile tests have shown a considerable improvement of ductile properties with a significant reduction of yield strength and an increase of ultimate elongation. In particular a conventional yield stress f_{02} of 18 MPa and a ductility of around 50% have been registered. For the sake of clarity, the comparison, in terms of strain-stress relationship, between the adopted pure aluminium alloy after the applied heat treatment, a common aluminium alloy (AW5154 A) and a typical low strength steel is shown in Figure 3.

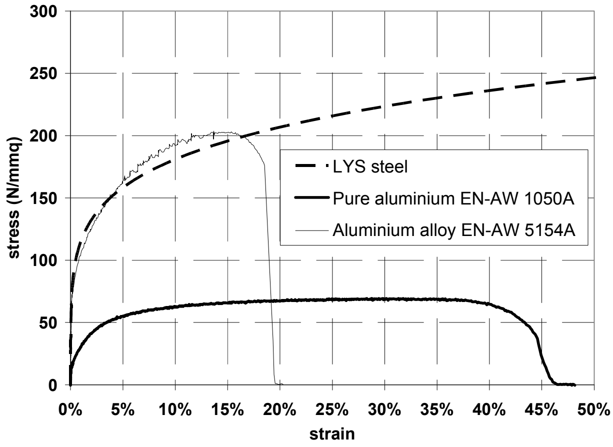

Figure 3. Comparison of Stress-strain Relationship Between Considered Low-strength Materials

In addition, as already emphasised in previous studies (Nakashima [3], Katayama [10]), the characterization of the cyclic behaviour of a low yield strength material is very important, as the isotropic hardening component could influence favourably the dissipative effect of the devices made of this type of material, since a reinflating of the hysteretic cycles is usually detectable. For this reason, specific tensile-compression cyclic tests have been carried out on pure aluminium specimens equipped with a steel “jacket” able to inhibit out-of-plane deformations due to buckling phenomena in compression (see Figure 4). The obtained results have shown an important dissipative behaviour (see Figure 5-a) characterized by full hysteretic cycles, a substantial iso-resistance for each displacement level and the existence of an isotropic hardening component (see Figure 5-b). However, as far as the cyclic degradation is concerned, performed tests did not allow to yield final conclusions, since testing specimens showed unexpected local buckling phenomena, which invalidated the experimental results for displacements higher than +15 mm (see Figure 5-c, 5-d, 5-e).

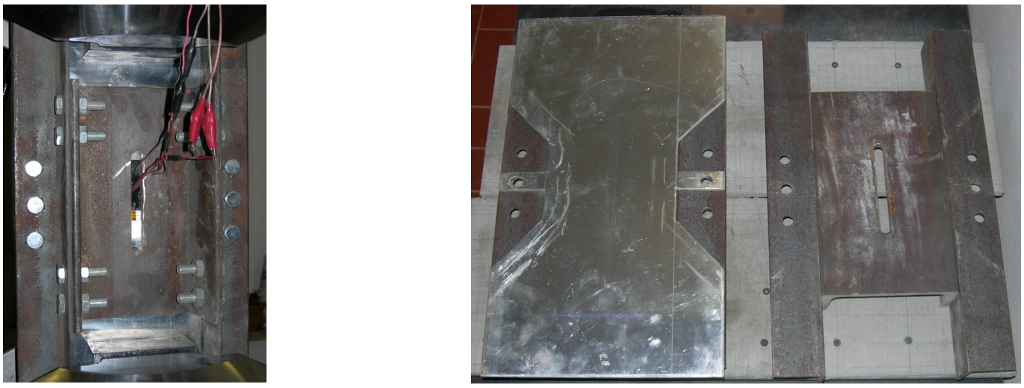

Figure 4. Buckling Inhibited Pure Aluminium Specimen

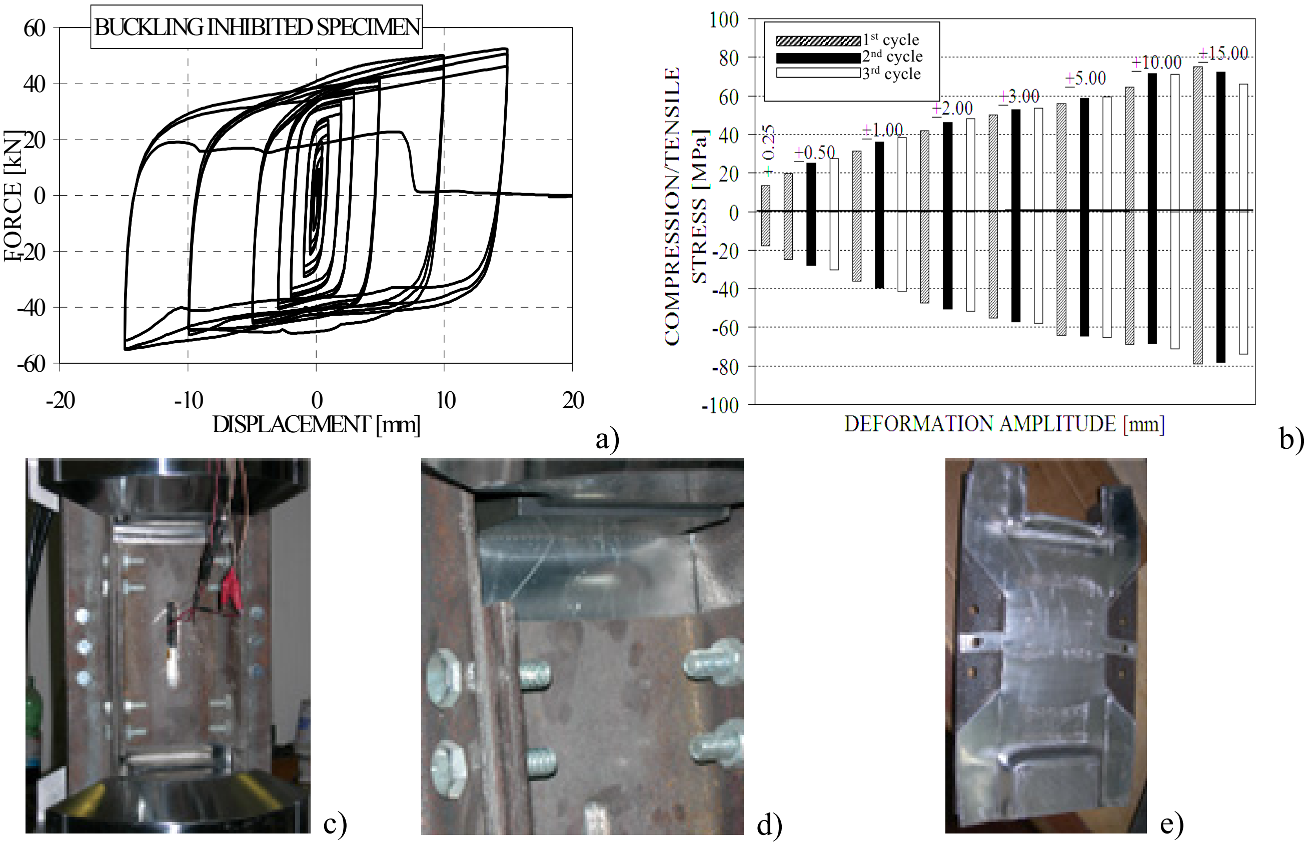

Figure 5. Buckling Inhibited Pure Aluminium Specimen: (a) Hysteretic Behaviour; (b) Strength for Each Cycle; (c-d-e) Collapse Mode

2.3 The Tested Specimens

The two tested shear panels, which henceforth will be indicate as “type 1” and “type 2”, are both characterized by global dimensions of 500 by 500 mm and a plate thickness of 5 mm. They are equipped with welded rectangular-shaped ribs, equally placed on the two faces of the panels, whose depth is 60 mm and which are made of the same material and thickness of the basic plates. The two specimens have been inserted into a pin jointed steel framework and are linked to its channel elements along their edge by means of tightened steel bolts. The stiffeners arrangement has been chosen in such a way to have a slenderness ratio a_w/t_w equal to 100 and 50 for shear panel “type 1” and “type 2”, respectively (see Figure 6). The spacing and depth of the ribs have been selected to fulfil the requirements provided by the European Standard to ensure shear buckling of the plate after shear yielding (Höglund et al. [11]). In fact, Eurocode 9 [12] provides the following limit value (Eq. 1) of a slenderness parameter l_w under which shear buckling resistance is higher than the yielding resistance:

$$\bar{\lambda}_w = \frac{0.83}{\eta} = 0.69 \qquad (1)$$

where the η factor, for which Eurocode 9 fixes a superior limit value of 1.2, is given by the following expression (Eq. 2):

$$\eta = 0.7 + 0.35 \cdot \frac{f_{aw}}{f_{ow}} \qquad (2)$$

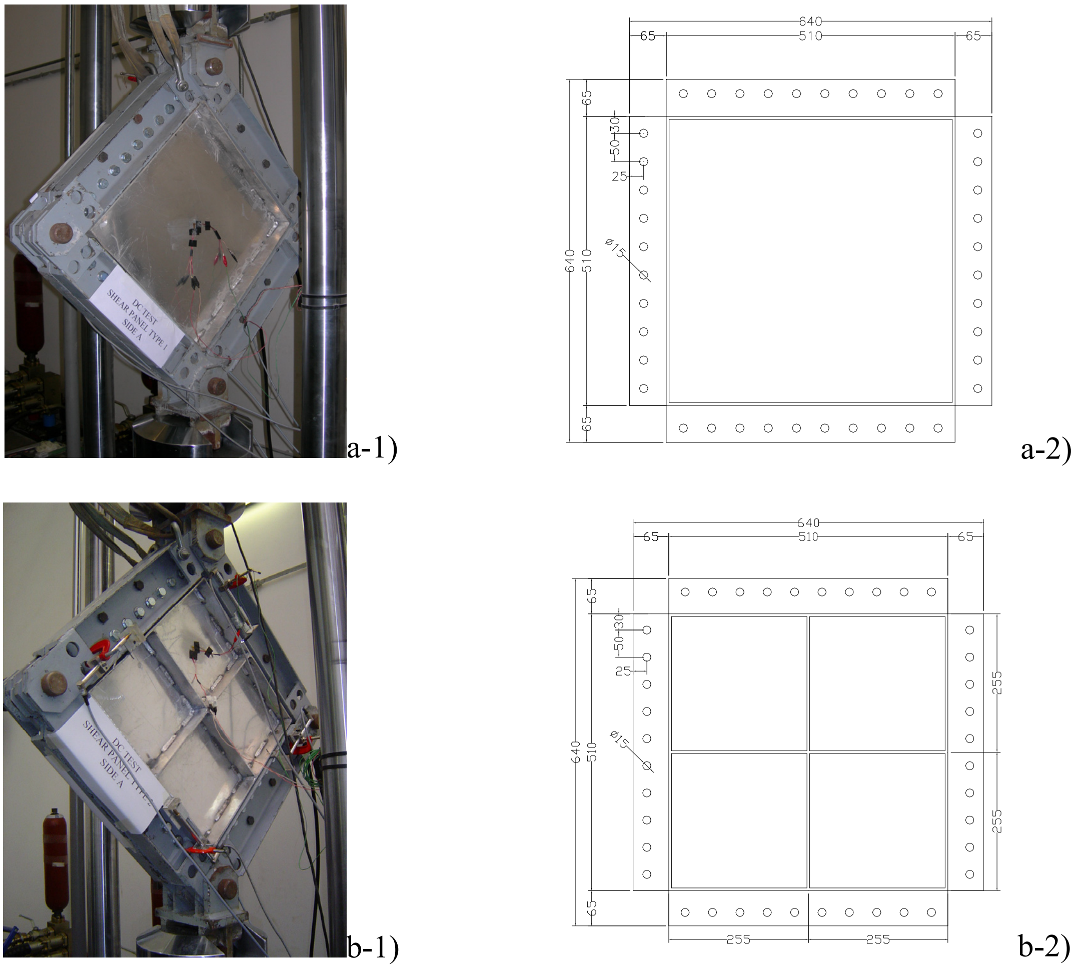

a-1) a-2)

b-1) b-2)

Figure 6. Testing Specimens: (a) Shear Panel “type 1”; (b) Shear Panel “type 2”

In the case being, the η factor has been conventionally assumed equal to 1.2, even though the hardening ratio a (f_{aw}/f_{ow})= 3 would lead to a corresponding h value equal to 1.75.

Hence, it is possible to observe that studied shear panels in such design assumptions guarantee a slenderness parameter value lower than the limit one. In particular, the slenderness parameters for the proposed panels, considering that panel "type 1" could be related to a "plate girders with web stiffeners at support" while panel "type 2" to a "plate girders with intermediate web stiffeners", are given by Eq. 3 and Eq. 4, respectively:

- Shear panel "type1": $$\lambda_{w,1} = 0.35 * \frac{b_w}{t_w} * \sqrt{\frac{f_0}{E}} = 0.66 \tag{3}$$
- Shear panel "type2": $$\lambda_{w,2} = \frac{0.81}{\sqrt{k_\tau}} * \frac{b_w}{t_w} * \sqrt{\frac{f_0}{E}} = 0.55 \tag{4}$$

As far as the effectiveness of the flexural stiffness of panel type 2 longitudinal and intermediate ribs is concerned, it is possible to observe that the adopted depth of 60 mm fulfils the Eurocode 9 requirements in order to classify them as rigid supports. In particular, since the panel has an aspect ratio a/h_w equal to 0.5 (smaller than the limit value of $\sqrt{2}$), the minimum second moment of area of the ribs to be not involved in global buckling phenomena of the shear plate is:

$$I_{st,\lim,2} = 1.5 \cdot \frac{h_w^3 \cdot t_w^3}{a^2} = 375000 mm^4 \tag{5}$$

It is worthy noting that in the case being the second moment of area is equal to 720000 mm^4, therefore about twice the above limit value.

On the other hand, similar considerations are not necessary for the panel "type 1", since the rigid end posts are realized on the four edges by means of the rigid perimeter beams of the frame in which the plate is installed.

3. THE EXPERIMENTAL TESTS

3.1 Loading Protocol and Applied Measurement Devices

The loading protocol used for tests has been set on the basis of the ECCS-CECM [13], which, for cyclic procedures, retrieves a load history essentially based on some cycles in the elastic range and then on three cycle repetitions for progressively increasing displacement amplitudes, defined as integer multiples of v_y, which is the displacement corresponding to the attainment of yielding. In the case being, the conventional yielding tangential stress can be fixed on the based of the conventional yielding tangential stress stated as in (Eq. 6)

$$\tau_y = \frac{f_{0.2}}{\sqrt{3}} = 10.39 MPa \tag{6}$$

Such a stress value corresponds to a shear strain equal to g=0.04%, hence the diagonal displacement v_y corresponding to the attainment of yielding can be evaluate as about 0.5 mm. Since this value is very small, the first steps of the above procedure have been eliminated, while the other ones have been left unvaried, so that the adopted testing protocol for each panel type is the one shown in Figure 7-a, where the ordinate indicates the applied diagonal displacement on the top of the surrounding frame (see Figure 7-b).

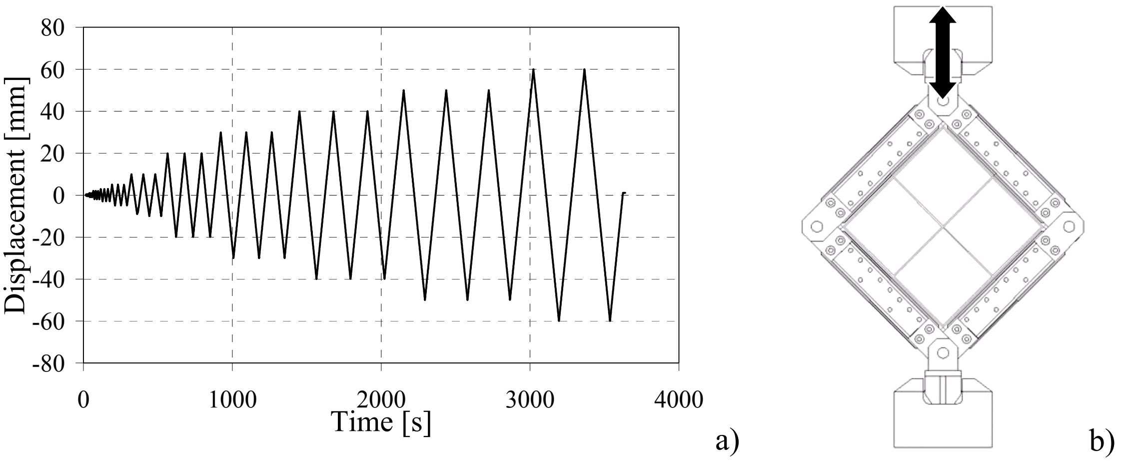

a) b)

Figure 7. Loading Scheme (a) and Applied Displacement History (b)

Such a displacement was measured by means of a mechanical transducer whose signal was fed back in real time to the controller as an instrument of supervision of the jack motion. Also, four mechanical transducer have been placed on the perimeter of the panels, to measure the relative motion between the panel edges and the frame elements and therefore to understand which is the influence of the frame-to-plate bolted connections on the behaviour of the whole system. This is a very important aspect, as previous experimental campaigns carried out on similar devices shown that bolted connections may represent the weak point of the system. To monitor the strain behaviour of tested shear panels, a pair of uniaxial strain gauges were also glued at the centre of the panel for panel "type 1" and at the centre of a sub panel of panel "type 2". The applied measurement instrumentation and its arrangement and location can be observed in Figure 6.

4. TEST RESULTS, EXPERIMENTAL EVIDENCES AND DISCUSSION

In this section, a careful presentation and discussion of both the obtained test results and experimental evidence is provide. In Figure 8, the response of the two shear panel types is shown in terms of obtained force-displacement hysteretic cycles, while the relevant collapse modes are given in Figure 9.

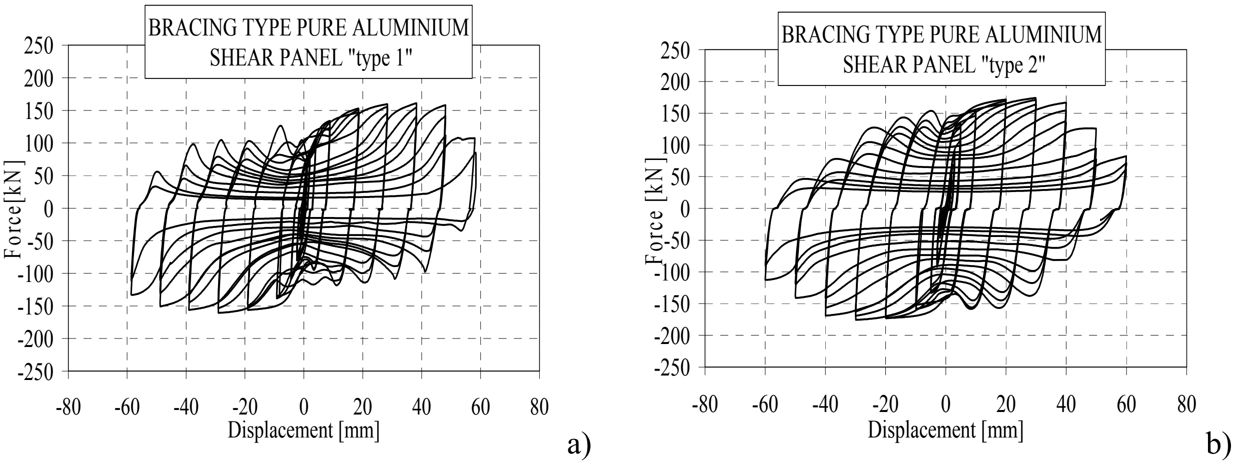

a) b)

Figure 8. Hysteretic Cycles: (a) Shear Panel "type 1"; (b) Shear Panel "type 2"

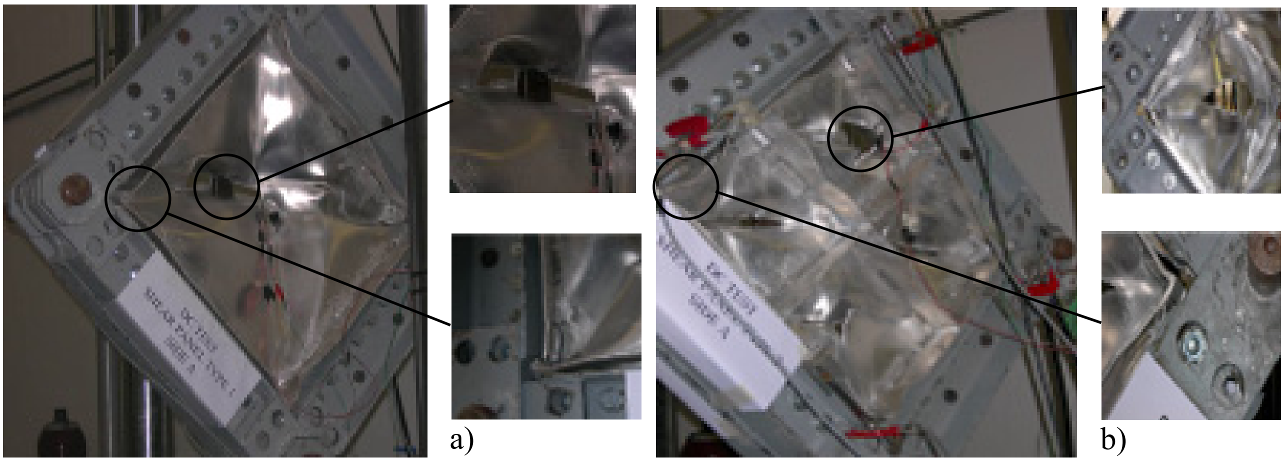

Figure 9. Collapse Modes: (a) Shear Panel “type 1”; (b) Shear Panel “type 2”

It should be noted that the two shear panels exhibited unexpected, but not so important slipping phenomena for very small force levels, which were probably due to the initial arrangement of the testing system. Anyway, it is evident that shear panel “type 2” provides a better hysteretic behaviour, with fatter cycles and larger resistant capacity. In fact, more important pinching effects characterize the obtained hysteretic cycles for shear panel “type 1”. These aspects are clearly emphasised considering the comparisons of the two panel types in terms of energy dissipation, hardening ratio, secant global stiffness and equivalent viscous damping ratio, as shown in Figure 10, where these parameters are expressed as function of the applied shear strain value.

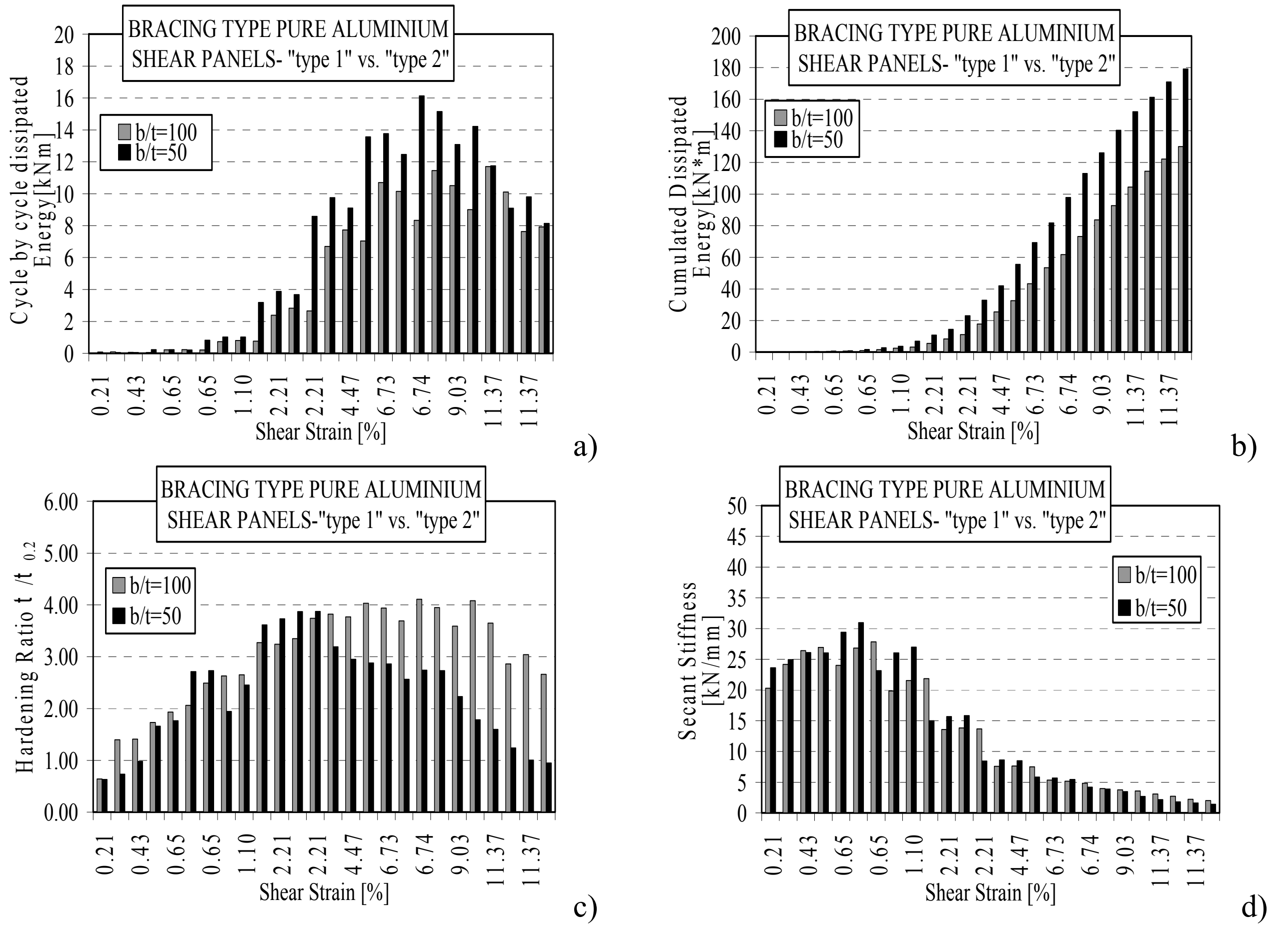

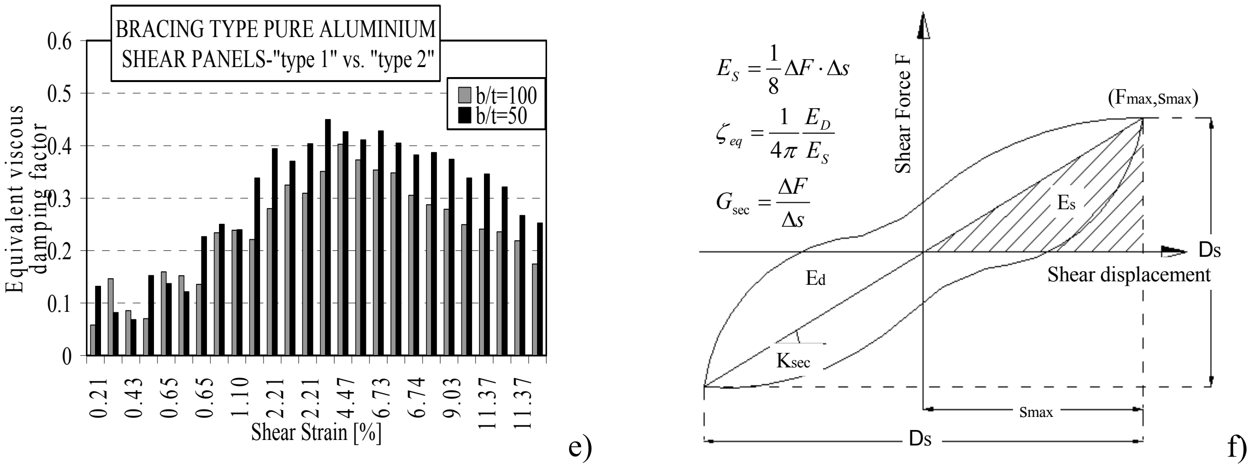

e) f)

Figure 10. Comparison of Results: (a) Dissipated Energy Per Cycle; (b) Cumulated Energy; (c) Hardening Ratio; (d) Secant Shear Stiffness; (e) Equivalent Viscous Damping Factor; (f) Definition of Dissipated Energy (E_s), Equivalent Viscous Damping (ζ_{eq}) and Secant Shear Stiffness (G_{sec})

It is worthy noting that both systems provide a very high dissipative capability, testified by maximum equivalent viscous damping ratio values of around 0.4 which are achieved for a shear strain of 6.73% (corresponding to a diagonal displacement amplitude of 30 mm). However, the panel configuration “type 1” exhibited a higher value at collapse of both the hardening ratio and the secant shear stiffness. This was mostly due to the influence provided by the perimeter connecting system. In fact, it has to be observed that panel “type 2” is characterized by a higher resistant peak, which is correlated directly to a secondary resistant mechanism in which both the transversal and longitudinal intermediate ribs operate as a sort of framework axially stressed working in parallel with the shear plate. It means that bolted connections are more stressed, anticipating their failure respect to shear panel configuration “type 1”. Obviously, a better performance of the proposed devices could be obtained by applying an improvement to the connection manufacture. Anyway, it is apparent that in terms of cumulated energy and equivalent viscous damping factor, the panel “type 2” behaved better than panel “type 1”, due to the beneficial effect of the stiffeners. On the other hand, this aspect is partly balanced by the higher fabrication cost of panel “type 2”.

As far as the experimental evidences are concerned, three principal behavioural phases can be recognised. In the first one no buckling phenomena occurred and a pure shear resisting mechanism was developed. Analyzing the strain gauges measurements in Figure 11, which are expressed as a function of time, it is clearly evident that the first buckling phenomena arose after about 100 seconds and 200 seconds from the test starting, for panel “type 1” and panel “type 2”, respectively.

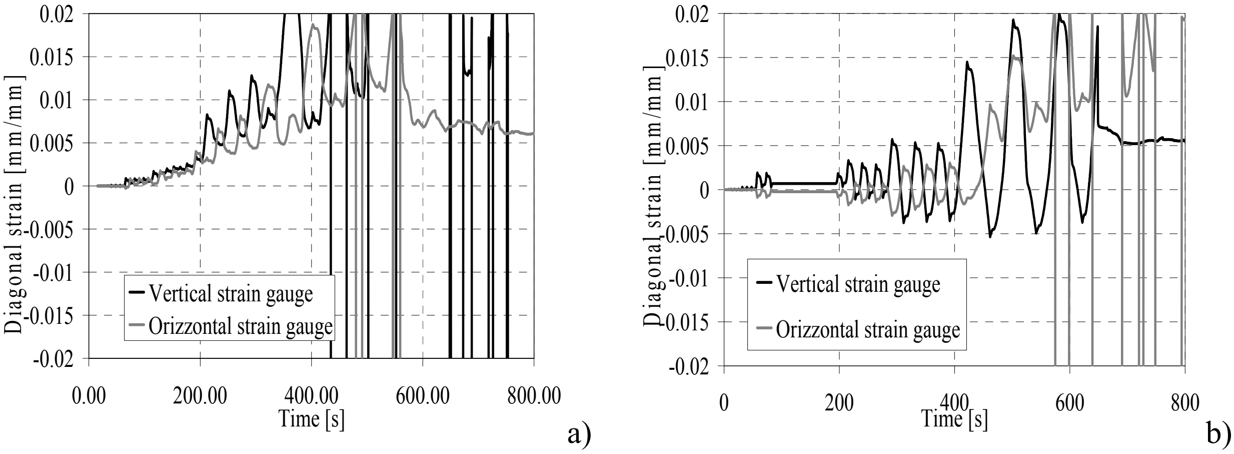

a) b)

Figure 11. Strain Gauges Measurements: (a) Shear Panel “type 1”; (b) Shear Panel “type 2”

Considering the experimental layout shown in Figure 7a, it is possible to determine the diagonal displacements corresponding to the above mentioned testing times, they corresponding to a displacement amplitude equal to ±2.00 mm and ±5.00 mm for panel "type 1" and panel "type 2", respectively. The detailed analysis of the initial phase of the test as shown in Figure 11-a and Figure 11-b gives an additional information on the yielding achievement (see Figure 12). In fact, considering a linear elastic behaviour of the base material with a Young's modulus E=66000 MPa, it is possible to fix a strain level corresponding to the attainment of the conventional yielding stress (18 MPa) equal to:

$$\varepsilon_y = \frac{f_{0.2}}{E} = \frac{18}{66000} = 0.000272 \tag{7}$$

Such a strain value is achieved after 40-60 seconds of time testing, which correspond to a diagonal displacement of 0.5 mm, this being the value of the elastic displacement (v_y) assumed to define the applied loading protocol discussed in Section 3.

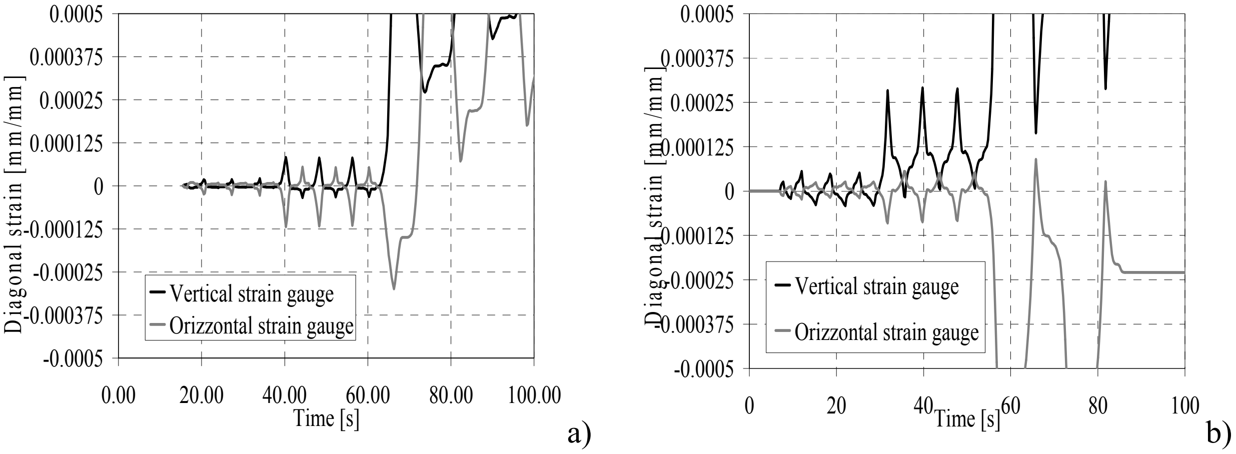

Figure 12. Elastic Strain Gauges Measurements: (a) Shear Panel "type 1"; (b) Shear Panel "type 2"

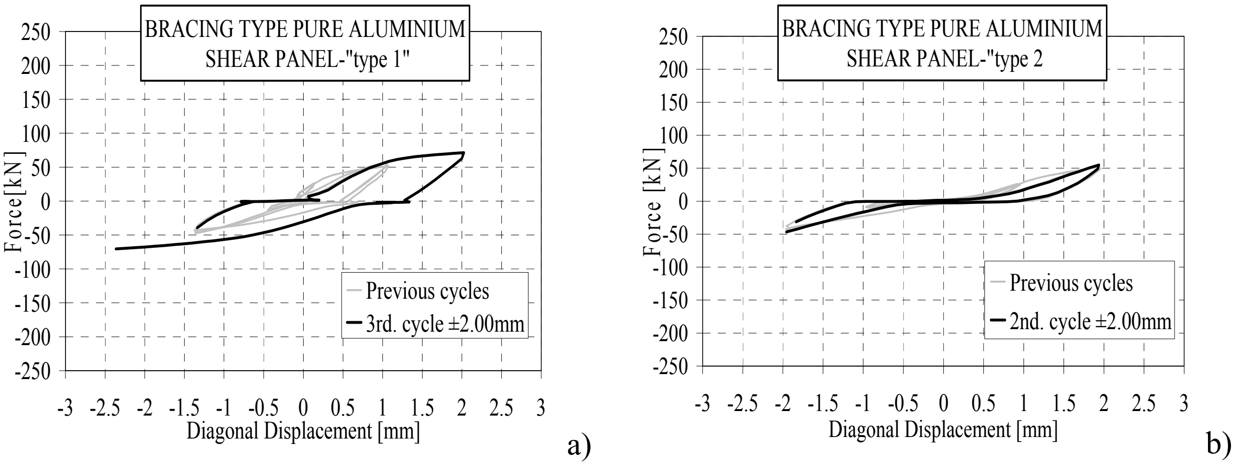

Figure 13. First Behavioural Phase; ±2.00 mm Amplitude Hysteretic Cycles :
(a) Shear Panel "type 1"; (b) Shear Panel "type 2"

In Figure 13, two characteristic hysteretic cycles of the first behavioural phase, corresponding to a diagonal displacement of ±2.00 mm, are shown for both panel “type1” and panel “type 2”. These cycles allow the determination of the initial slipping of ±0.70 mm for shear panel “type 1” and ±1.25 mm for shear panel “type 2”, respectively.

The second behavioural phase ranges between diagonal displacement amplitudes of ±5.00 mm and ±40.00 mm. In this case, buckling phenomena are triggered off and develop along two diagonal bands, where significant out of plane deformations are produced. Pinching effects are clearly visible in the hysteretic cycles starting from a diagonal displacement amplitude of ±10.0 mm for panel “type 1” (Figure 14-a) and 20.0 mm for panel “type 2” (Figure 14-b). In Figure 14-c and Figure 14-d two characteristic hysteretic cycles registered at the end of the above second behavioural phase are shown, while in Figure 14-e and Figure 14-f buckle configurations of the panels for a displacement amplitude of ±30.0 mm are depicted.

In the third behavioural phase, the diagonal displacement amplitude ranges between ±40.0 mm and ±50.0 mm. The collapse of the perimetric connection system, whose bearing capacity was exceeded in the previous behavioural phase, is evidenced as well as the failure of the shear plate in the zone where the buckled bands developed in the second behavioural phase intersected each other (see Figures 8 and 9). A significant loss of resisting strength, up to 50%, is detectable when the collapse of the whole systems is attained.

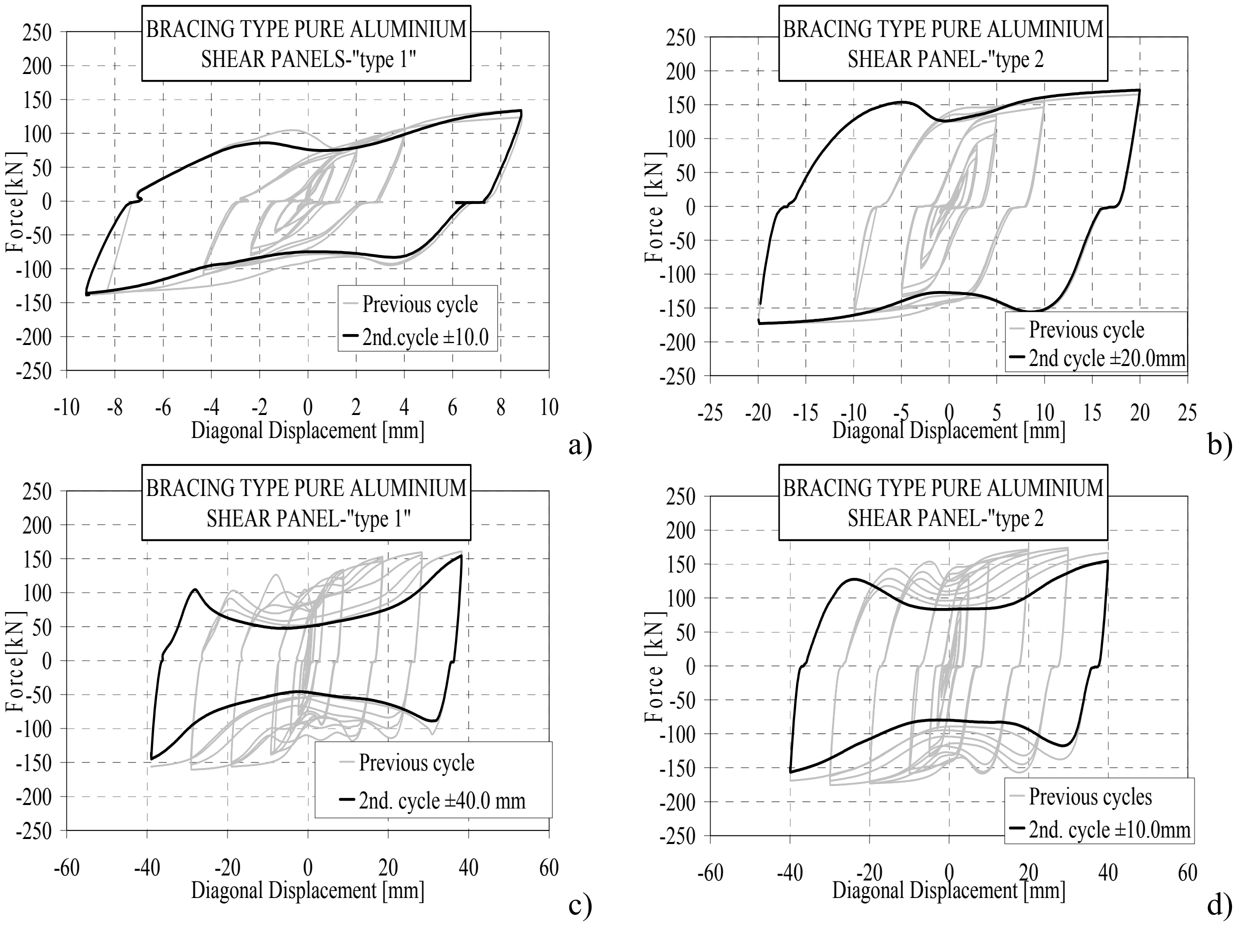

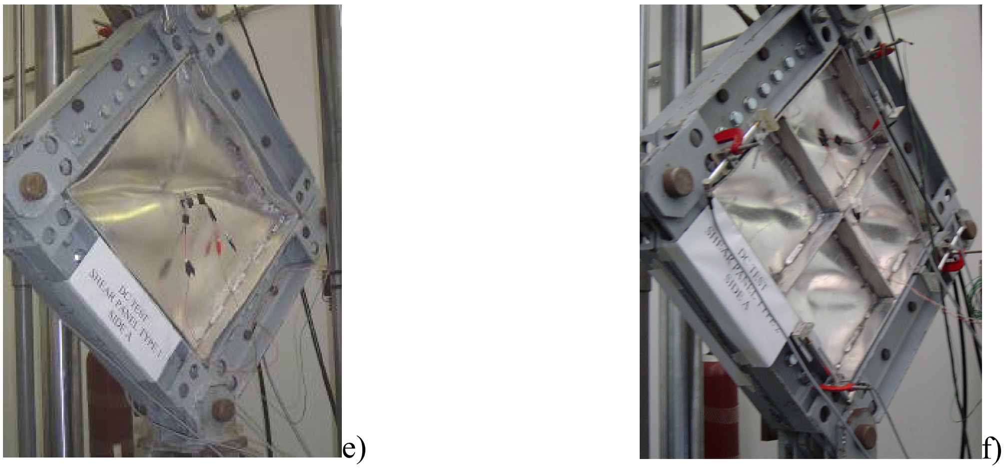

e)

f)

Figure 14. Second Behavioural Phase; Hysteretic Cycles: (a-c) Shear Panel “type 1”; (b-d) Shear Panel “type 2”. Buckled Shapes for Displacement Amplitude of ±30.00: (e) Shear Panel “type 1”; (f) Shear Panel “type 2”

5. CONCLUSIONS

In the current paper, experimental tests on two bracing type pure aluminium shear panels have been presented and deeply analyzed. In addition, considering the innovative features of the proposed base material, monotonic and cyclic tests on the adopted pure aluminium alloy have been also shown.

The tests were carried out in order to assess the suitability of the shear panels to be used as passive control systems in frame structures. It has been ascertained that, compared with a full bay type solution, the bracing type AW 1050A aluminium alloy shear panels provide a better dissipative behaviour, which is characterized by maximum equivalent viscous damping ratios up to 0.4, for inter-story drift values which are of concern for common structural applications. Hence it has been emphasised that the response of both systems is characterised by three main behavioural phases (initial elastic, plastic shear buckling and collapse). Such phases have been detected qualitatively, on the basis of the exhibited resisting mechanism, but also quantitatively, by the measured diagonal displacement amplitudes corresponding to the attainment of the yielding stress and the first buckling phenomenon. In particular, the obtained experimental results have evidenced that the shear panel configuration having a geometric slenderness a_w/t_w=50 presents more stable and larger hysteretic cycles, while the shear panel with a_w/t_w=100 is characterised by a higher value of ultimate hardening ratio and shear global stiffness, as the presence of internal ribs in shear panel “type 2” determines higher stresses for the connecting system.

From this point of view further developments could be addressed to investigate more refined solutions, characterised by shear panels with different stiffener arrangements and with improved connection details.

REFERENCES

[1] Dargush, G.F. and Soong T.T., “Behaviour of Metallic Plate Dampers in Seismic Passive Energy Dissipation Systems”, Earthquake Spectra, 1995, Vol. 11, pp. 545-568.

[2] Chen, Z., Ge, H. and Usami, T., “Hysteretic Models of Stiffened Shear Panel Dampers”, Journ. Struct. Engrg., ASCE, 2006, Vol. 3, pp. 478-483.

[3] Nakashima, M., “Strain-Hardening Behaviour of Shear Panels Made of Low-Yield Steel. I: Model”, Journ. Struct. Engrg., ASCE, 1995 (a), Vol. 121, No. 12, pp. 1742-1749.

[4] Nakashima, M., Akazawa, T. and Tsuji, B., “Strain-Hardening Behaviour of Shear Panels Made of Low-Yield Steel. II: Test”, J. Struct. Engrg, ASCE, 1995 (b), Vol. 121, No. 12, pp. 1750-1757.

[5] Nakagawa, S., Kihara, H., Torii, S., Nakata, Y., Matsuoka, Y., Fujisawa, K. and Fukuda, K., “Hysteretic Behaviour of Low Yield Strength Panel Shear Walls-Experimental Investigation”, Proceedings of the 11th WCEE, 1996, Acapulco, Mexico.

[6] De Matteis, G., Mazzolani, F.M. and Panico, S., “Pure Aluminium Shear Panels as Passive Control System for Seismic Protection of Steel Moment Resisting Frames”, Proceedings of the IV International Conference STESSA ’03 (Behaviour of Steel Structures in Seismic Areas), Balkema, 2003, pp. 609-614, Naples, Italy.

[7] De Matteis, G., Formisano, A., Panico S. and Mazzolani, F.M., “Numerical and Experimental Analysis of Pure Aluminium Shear Panels with Welded Stiffeners”, Computers & Structures, 2008, Vol. 86, No. 6, pp. 545-555.

[8] De Matteis, G., Mazzolani, F.M. and Panico, S., “Pure Aluminium Shear Panels as Dissipative Devices in Moment-Resisting Steel Frames”, in Earthquake Engineering and Structural Dynamics, Wiley InterScience, DOI: 10.21002/eqe, Vol. 36, pp. 841-859, 2007b.

[9] RILEM TC 83-CUS Testing Recommendation, “Tension Testing of Metallic Structural Material for Determining Stress-Strain Relations under Monotonic and Uniaxial Tensile Loading”, Material and Structures, 1989, Vol. 23, No. 133, pp. 35-46.

[10] Katayama, T., Ito, S., Kamura, H., Ueki, T. and Okamoto, H., “Experimental Study on Hysteretic Damper with Low Yield Strength Steel Under Dynamic Loading”, Proceedings of the 12th WCEE, 2000, Auckland, New Zealand.

[11] Höglund, T., “Shear Buckling Resistance of Steel and Aluminium Plate Girders”, Thin-Walled Structures, 1997, Vol. 29, No. 1-4, pp 13-30.

[12] EUROCODE 9, “Design of Aluminium Structures prEN 1999-1-1, Final Draft”, 2006.

[13] ECCS-CECM, “Recommended Testing Procedure for Assessing the Behaviour of Structural Steel Elements Under Cyclic Loads”, 1985.

SENSITIVITY AND STATISTICAL ANALYSIS WITHIN THE ELABORATION OF STEEL PLATED GIRDER RESISTANCE

J. Melcher[1,]*, M Škaloud[2], Z. Kala[1], M. Karmazínová[1]

[1]Brno University of Technology, CZ-602 00 Brno, Czech Republic,
[2]Professor, Academy of Sciences of the Czech republic, Prague
**(Corresponding author: E-mail: melcher.j@fce.vutbr.cz)*

ABSTRACT: The objective of the paper is to analyse the influence of initial imperfections on the behaviour of thin-walled girders welded of slender plate elements. The girder was modelled, using the geometrically and materially non-linear variant of the shell finite element method, by the ANSYS program. The ultimate static load-carrying capacity and the state of stress were considered as the output analysed quantities. The influence of the variability of initial imperfections on the variability of ultimate static load-carrying capacity and on the variability of the state of stress studied was calculated by sensitivity analysis. The sensitivity analysis was evaluated on a computer by applying the numerical simulation LHS method and statistical characteristics evaluated, based on the experiments. Real tests of girders with random initial imperfections the occurrence frequency of which is equivalent to experimental results are simulated numerically. In each LHS method run, both load-carrying capacity and state of stress are evaluated on the model based on nonlinear variant of shell finite elements. The stress state was evaluated by bending stresses developing in the crack-prone areas of a web "breathing" under repeated loads, which – as it was demonstrated by the experiments - occurred at the toes of the fillet welds connecting the "breathing" web with the girder flanges and stiffeners.

Keywords: Steel structures, fatigue, imperfection, sensitivity, reliability, plated girder

---

1. INTRODUCTION

Thin-walled structures, i.e. systems made of slender plate elements are nowadays very frequently encountered in both building and bridge construction. Among their most frequently used types are steel plate girders having a slender web, such as the girder shown in Figure 1.

The behaviour of steel girders is substantially affected by the buckling of the girder web, which for the kind of loading considered, is characterized by a diagonal buckled pattern the width and inclination of which depend on the rigidity of the peripheral elements of the web, i.e. of the flanges and stiffeners.

When the loading is quasi-constant, the failure mechanism consists of a diagonal plastic band in the web sheet and a system of more or less developed plastic areas in its boundary elements.

When the loading is repeated in a great number of cycles, then the web buckling is many times repeated, this phenomenon being now usually termed “web breathing”. In this case the failure mechanism (Figure 2) is made more complex by the initiation and propagation of fatigue cracks occurring at the toes of the fillet welds that connect the breathing web with its peripheral elements. The experiments and the theoretical analysis have demonstrated that this phenomenon is influenced by a number of factors, among them a significant role being played by unavoidable initial imperfections (Kala [1]). As it is in their nature that the initial imperfections are random variables, stochastic sensitivity analysis seems to be an ideal tool for an analysis of their effect (Kala [2-3]).

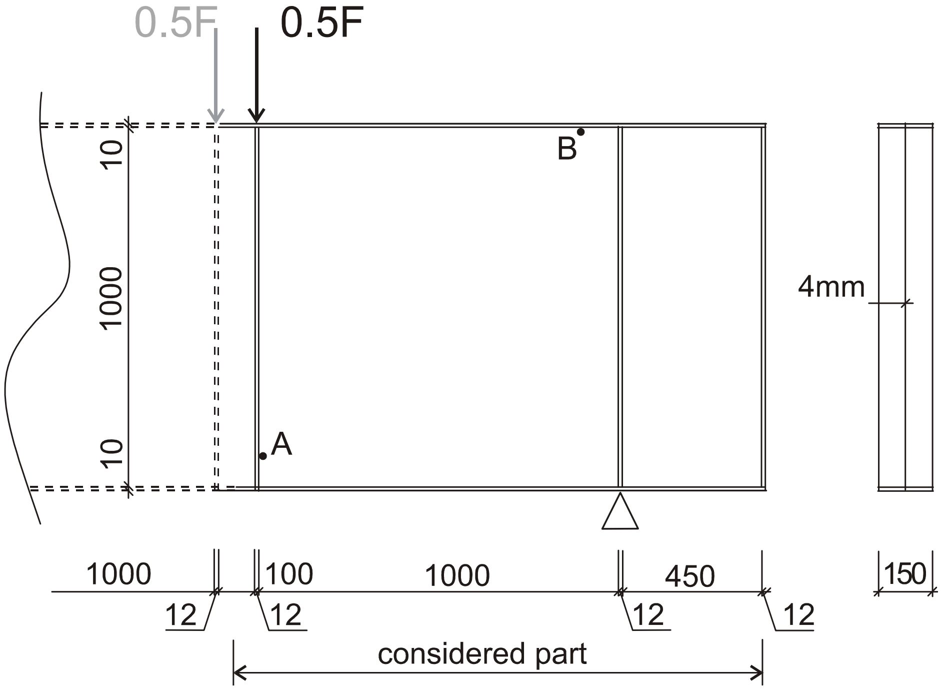

Figure 1. Geometry of the Tested Girder

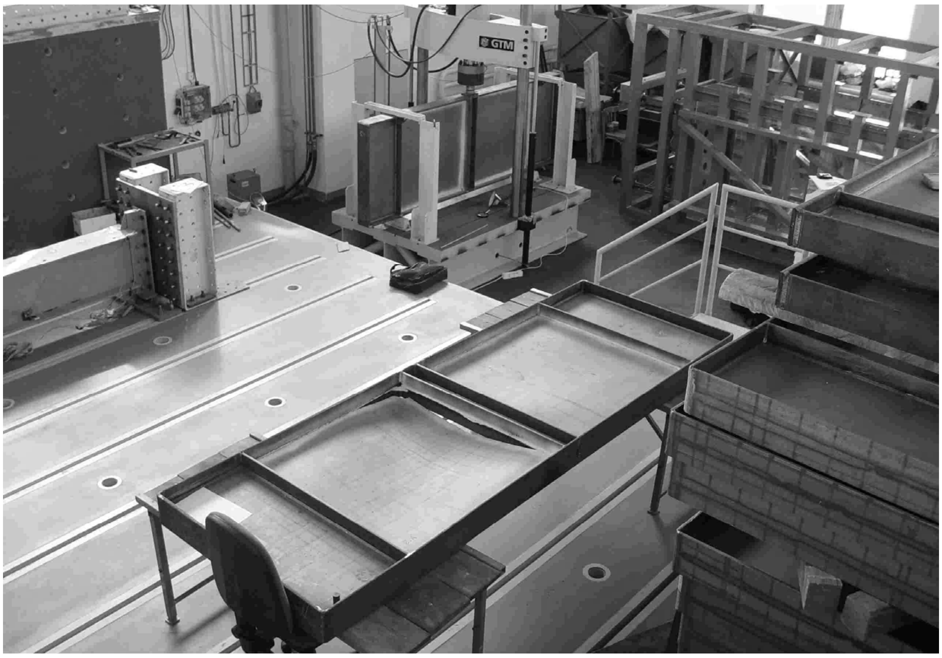

Figure 2. Test Specimen After Failure

2. SENSITIVITY ANALYSIS METHODS

The objective of this paper is therefore a stochastic sensitivity analysis which provides more extended information about the problem studied. The random input quantities are considered as if they were obtained by measurements, this enabling us to get quantified information about the influence of the scatter of individual parameters involved. This procedure can be employed with advantage in connection with the numerical simulation method Latin Hypercube Sampling Method (LHS), such as suggested in the review paper (Novák [4-5]) where also other variants of the stochastic sensitivity analysis are described. The LHS method makes it possible to simulate the realizations of input random quantities as if they were obtained by measurements.

A comprehensive review of various sensitivity analysis methods is given in (Saltelli [6]). For our research, the methods which can be applied for the sensitivity analysis evaluation can be divided as follows:

a) The methods based on the correlation coefficient study (Kala [2] and [7]).
b) The methods based on the study of variability coefficient ratios (Novák [4] and Kala [2]).
c) The methods based on the study of variances coefficient ratios (Kala [3] and [8]).
d) Special methods and methods for the probability analysis (Mang [9] and Juozapaitis [10]).

The first method can be applied practically to all numerical simulation methods of the Monte Carlo type. The method described is based on the assumption that there will be higher correlation degree with the output in case of the quantities relatively more sensitive to the output.

The so-called Spearman rank-order correlation r_i is frequently applied within the framework of a simulation method (Kala [2]). The Spearman rank-order correlation can be defined as:

$$r_i = 1 - \frac{6\sum_j \left(m_{ji} - n_j\right)^2}{N\left(N^2 - 1\right)} \qquad r_i \in [-1,1] \tag{1}$$

where r_i is the order representing the value of random variable X_i in an ordered sample among N simulated values applied in the j_{th} simulation (the order m_{ji} equals the permutation at LHS), n_j is the order of an ordered sample of the resulting variable for the j_{th} run of the simulation process ($m_{ji} - n_j$ is the difference between the ranks of two samples). If the coefficient r_i had the value near to 1 or -1, it would suggest a very strong dependence of the output on the input. Opposite to this, the coefficient with its value near to zero will signalise a low influence.

The second method is based on the comparison of sensitivity coefficients k_i, defined on behalf of variation coefficients by the relation:

$$k_i = 100\frac{v_{yi}^2}{v_y^2}\,[\%] \tag{2}$$

v_{yi} is the variation coefficient of the output quantity, assuming that all the input quantities except the i_{th} one ($i = 1, 2, \ldots, M$; where M is number of input variables) are considered to be deterministic (during the simulation, they are equal to the mean value);

v_y is the variation coefficient of the output quantity, assuming that all the input quantities are considered to be random ones.

3. INPUT RANDOM QUANTITIES

Experimental research with statistical evaluation of results can serve as the basic information source of the statistical distribution of input random quantities (Melcher [11]). In the problem solved in our research, we started from the large experimental research of the material and geometrical characteristics of steel products made by a dominant Czech producer (Melcher [12]).

A further random quantity which cannot be considered deterministically is Young's modulus *E*. The influence of the deviation of physical-mechanical material characteristics (of heterogeneousness above all) has been taken into consideration by the variability of this quantity. The Gaussian distribution with mean value m_E = 210 GPa and standard deviation S_E = 12.6 GPa was supposed (Soares [13] and Fukumoto [14]).

Table 1. Input Random Quantities

No.	Name of random quantity	Type of distribution	Dimension	Mean	Standard deviation
1.	Amplitude of sine initial web curvature	Rectangular	mm	0	2.887
2.	Web thickness	Gauss	mm	4	0.2
3.	Web yield strength	Gauss	MPa	284.5	21.5
4.	Web Young's modulus	Gauss	GPa	210	12.6
5.	Thickness of upper flange	Gauss	mm	10	0.7
6.	Yield strength of upper flange	Gauss	MPa	284.5	21.5
7.	Young's modulus of upper flange	Gauss	GPa	210	12.6
8.	Thickness of lower flange	Gauss	mm	10	0.7
9.	Yield strength of lower flange	Gauss	MPa	284.5	21.5
10.	Young's modulus of lower flange	Gauss	GPa	210	12.6
11.	Thickness of left-hand stiffener	Gauss	mm	12	0.84
12.	Yield strength of left-hand stiffener	Gauss	MPa	284.5	21.5
13.	Young's modulus of left-hand stiffener	Gauss	GPa	210	12.6
14.	Thickness of central stiffener	Gauss	mm	12	0.84
15.	Yield strength of central stiffener	Gauss	MPa	284.5	21.5
16.	Young's modulus of central stiffener	Gauss	GPa	210	12.6
17.	Thickness of right-hand stiffener	Gauss	mm	12	0.84
18.	Yield strength of right-hand stiffener	Gauss	MPa	284.5	21.5
19.	Young's modulus of right-hand stiffener	Gauss	GPa	210	12.6

The initial curvature of the web was introduced as one half-wave of the sine function both in the horizontal and vertical directions. The considered initial curvature variability is determined by the maximum amplitude value as a random quantity.

4. STATISTICAL ANALYSIS

The girder presented in Figure 1 was modelled by the finite element method, by applying the ANSYS program. The girder was modelled, in a very minute manner, by means of a mesh of shell four-nodes elements SHELL43. The girder symmetry and that of loading were made use of. For steel grade S235, bilinear cinematic material hardening was supposed. Further on, it was assumed that the onset of plastification occurred when the Mises stress exceeded the yield stress.

Within the framework of each run of the LHS method, the load-carrying capacity was found out by the geometrically and materially non-linear solution FEM. The Euler method based on proportional loading in combination with the Newton-Raphson method was used. The loading test is simulated by the incrementation of a loading step in the Euler method. The load-carrying capacity was determined as the loading rate at which the matrix of tangential toughness determinant K_t of the structure approaches zero with accurateness of 0.1 %. The incrementation run was decremented automatically. 200 "real tests" on girders according to Figure 1 with random imperfections were simulated by runs of the LHS method.

Second part of the study was focused on analysing bending stresses which occur at the edges of the girder web and are perpendicular to these edges, and are generated by a load = 420 kN. This value of the load corresponds to 60% of the mean load – bearing capacity determined with used LHS method, See Figure 3.

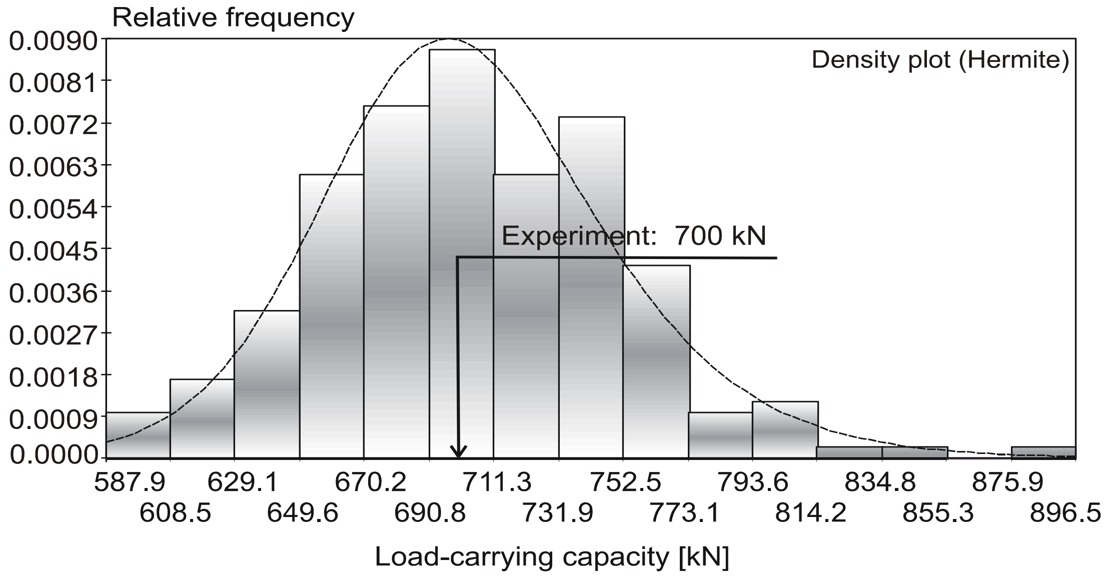

Figure 3. Distribution of Load-Carrying Capacity

5. SENSITIVITY ANALYSIS RESULTS

The stochastic sensitivity analysis enabled us to assess the relative sensitivity of random variability of the phenomenon studied to the random variability of individual input quantities. Figure 4 gives the results of an analysis of the sensitivity of the load-bearing capacity to initial imperfections. As long as the value of the correlation coefficient increases, the load-carrying capacity increases when also the value of the input quantity grows. A negative value of the coefficient heralds a negative effect of the quantity on the load-bearing capacity (e.g. quantity No I).

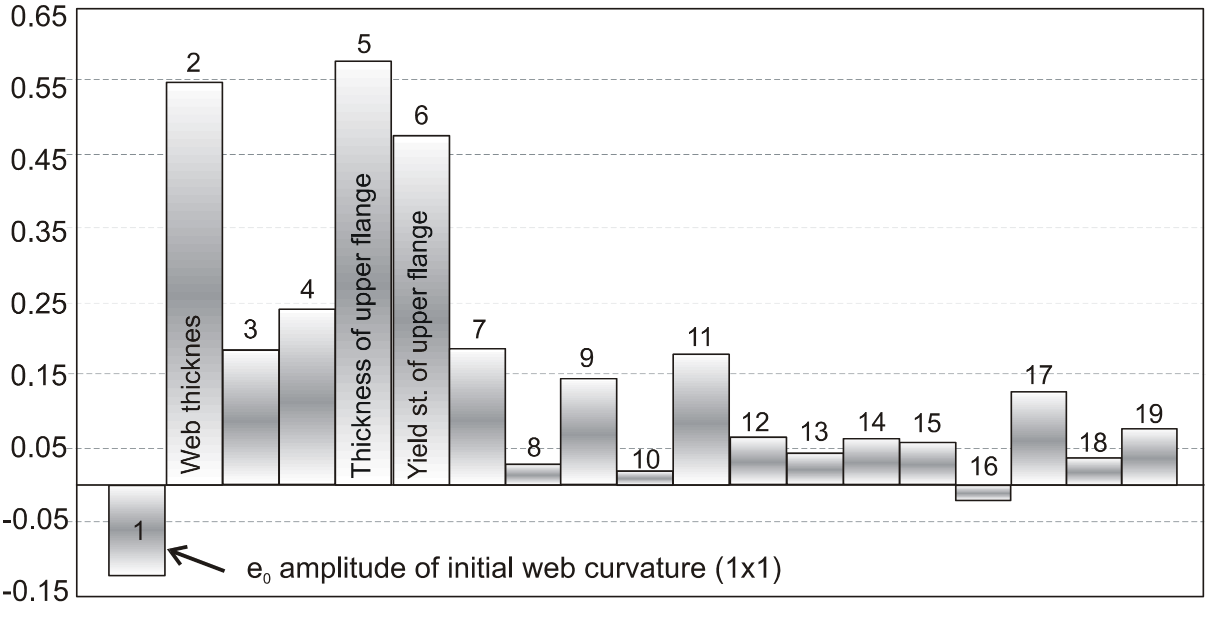

Figure 4. Sensitivity Analysis of the Load-Carrying Capacity

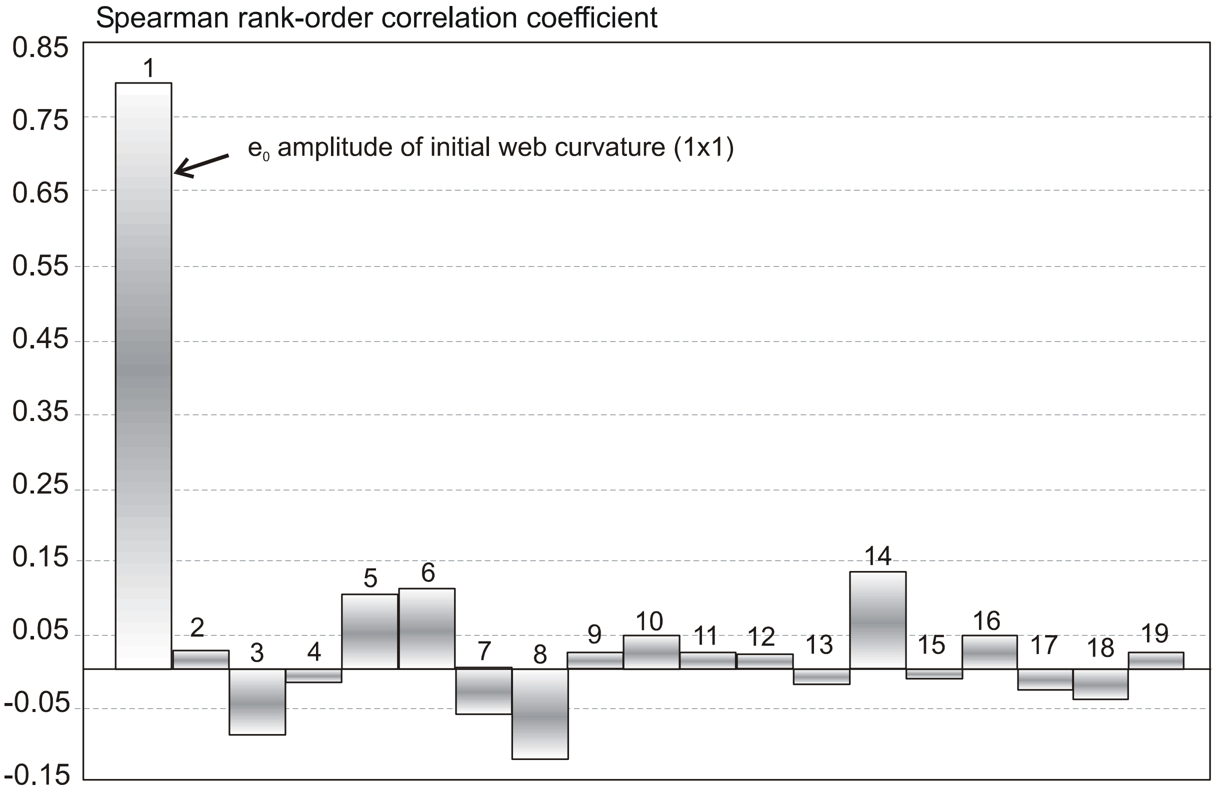

Figure 5. Sensitivity Analysis of the Bending Stress at Points A and B

6. CONCLUSIONS

It has been determined by the sensitivity analysis of static ultimate load carrying capacity that the girder upper flange thickness, web thickness and also upper flange yield strength influence the load-carrying capacity in the dominant way.

So long as the value of the quantities mentioned increases, the load-carrying capacity value increases, too. On the contrary, the variability influence of the web initial curvature e_0 on the girder load-carrying capacity is relatively low. The negative correlation coefficient value means that as long as the value of the amplitude of initial curvature e_0 increases, the ultimate load-carrying capacity decreases.

The results of the authors' sensitivity analysis confirmed a great influence of the initial curvature of a slender web on the variability of bending stresses occurring at points A and B, i.e. in the crack-prone areas of the web if the girder is subjected to repeated loading. On the contrary, if the same girder is under the action of a quasi-constant load, the influence of the initial out-of-flatness of the web on the ultimate strength of the girder (where the web is in the case studied exposed to combined shear and bending) is slight.

ACKNOWLEDGEMENTS

The presented research was supported by grants 103/07/1067 of GACR and IAA201720901 of AVCR and by research project Reg. No. MSM 0021630519.

REFERENCES

[1] Kala, Z., “Fuzzy Probability Analysis of the Fatigue Resistance of Steel Structural Members under Bending“, International Journal of Civil Engineering and Management, Vol 14, Issue 1, 2008, pp.67-72, ISSN 1392–3730.

[2] Kala, Z., “Sensitivity Analysis of the Stability Problems of Thin-walled Structures“, Journal of Constructional Steel Research 61 (2005), pp.415–422, ISSN 0143–974X.

[3] Kala, Z., “Sensitivity Assessment of Steel Members under Compression“, Engineering Structures (2008), doi:10.1016/j.engstruct.2008.04.001.

[4] Novák, D., Teplý, B. and Shiraishi, N., “Sensitivity Analysis of Structures - A Review”, Proc. of The Fifth International Conference on Civil and Structural Engineering Computing, Edinburgh, 1993, pp.201–207.

[5] Novák, D., Teplý, B. and Keršner, Z., “The Role of Latin Hypercube Sampling Method in Reliability Engineering”, Proc. of ICOSSAR’97 - The 7th Int. Conf. on Structural Safety and Reliability, Kyoto/Rotterdam: Balkema, 1997, Vol. 1, pp.403-409.

[6] Saltelli, A., Ratto, M., Andress, T., Camplolongo, F., Cariboni, J., Gatelli, D., Saisana, M. and Tarantola, S., “Global Sensitivity Analysis Guiding the Worth of Scientific Models”, New York: John Wiley and Sons, 2007.

[7] Kala, Z., Kala, J., Škaloud, M. and Teplý, B., “Sensitivity Analysis of the Effect of Initial Imperfections on the (i) Ultimate Load and (ii) Fatigue Behaviour of Steel Plate Girders”, International Journal of Civil Engineering and Management, Vol XI, No 2, 2005, pp.99–107, ISSN 1392–3730.

[8] Kala, Z., “Sensitivity Analysis of Carrying Capacity of Steel Plane Frames to Imperfections“, In Proc. of Int. Conf. of Numerical Analysis and Applied Mathematics, Psalidi (Greece), 2008, pp.298-301, ISBN 978-0-7354-0576-9, ISSN 0094-243X.

[9] Mang, H. A., Jia, X., Hoefinger., G. “Hilltop Buckling as the Alfa and Omega in Sensitivity Analysis of the Initial Postbuckling Behavior of elastic structures“, International Journal of Civil Engineering and Management, Volume 15, Number 1, 2009, p. 35-46, ISSN 1392–3730.

[10] Juozapaitis, A., Norkus, A., Vainiūnas P. “Shape Stabilization of Steel Suspension Bridge“, The Baltic Journal of Road and Bridge Engineering, Vilnius: Technika, 2008, Vol III, No 3, p. 137-144, ISSN 1822-427X.

[11] Melcher, J., “On some problems of analytical and probability approaches to structural design”, In Proc. of the 3rd International Conference on Advances in Steel Structures, VOLS I & II, Hong-Kong (China), 2002, pp. 1185-1192.

[12] Melcher, J., Kala, Z., Holický, M., Fajkus, M. and Rozlívka, L., “Design Characteristics of Structural Steels Based on Statistical Analysis of Metallurgical Products”, Journal of Constructional Steel Research, 2004, Vol. 60, pp.795-808, ISSN 0143-974X.

[13] Guedes Soares, C., “Uncertainty Modelling in Plate Buckling”, Journal Structural Safety, 1998, Vol. 5, pp. 17-34.

[14] Fukumoto, Y., Kajita, N. and Aoki, T., “Evaluation of Column Curves Based on Probabilistic Concept”, In Proc. of International Conference on Stability, Prelim. Rep., Gakujutsu Bunken Fukyu – Kai Publ., 1976, Tokyo, pp. 1-37.

A CLOSED FORM SOLUTION FOR PREDICTING SPRINGBACK IN BENDING OF BEAMS INCLUDING HARDENING EFFECT

A. López Castro, J.F. Durodola* and N.A. Fellows

School of Technology, Oxford Brookes University,
Wheatley Campus, Wheatley, Oxon OX33 1HX, U.K.
**(Corresponding author: E-mail: jdurodola@brookes.ac.uk)*

ABSTRACT: Springback is an implicit phenomenon in most forming processes and needs to be accounted for in the design of forming tools. This is essential in order to limit the number of iterations required during the design and fabrication of forming tools and dies. This work presents a closed form solution for predicting springback in bending including hardening effect. Springback was also determined using experimental testing. The results obtained are compared with analytical results and the influence of hardening on springback is analysed.

1. INTRODUCTION

Sheet metal forming is one of the most important manufacturing processes for mass production in industry. Several sheet-forming processes include bending. In these processes, plastic deformation is followed by some elastic recovery upon unloading. This change in shape is known as springback and its extent depends on material properties, geometry and tooling dimensions. Springback can be particularly significant in structures, panels and components formed into large radii.

Springback results in the deviation of a component from a desired shape after the forming load is removed. This means that additional geometric adjustments have to be made to account for it in the design of forming tools and dies. The phenomenon has been analysed using different procedures over the last few decades. Early works by researchers developed correction curves using empirical relations based on experimental testing [1-2]. Many analytical solutions have subsequently been derived [3-6]. A good review of these previous works can be found in references [7-9]. Other workers have used the finite element method [10-11].

The earliest attempt to find an analytical solution for springback correction was started by Sturm and Fletcher [3] in the aircraft industry in the early 1940s. The solution developed was however cumbersome to apply. It requires explicit determination of distances from the neutral plane to beam surfaces as well as surface stresses. Schroeder [5] presented another analytical solution in 1943 but this was also rather complex to implement. It was not until the late 1950s when by examining narrow beams of an elastic-perfectly plastic material that Gardiner [6] developed a solution for determining springback after bending that was far simpler to use. Gardiner's formula has been embraced by the metals forming community for decades as a very good approximation for the calculation of springback.

As highlighted in the foregoing, Gardiner's solution assumes elastic perfectly plastic material behaviour. Most engineering materials however exhibit strain hardening with significant increase in strength in the post yield regime. It will therefore be helpful to obtain a more general and accurate closed form equation for predicting springback that account for this factor. This work presents a closed form solution for predicting springback in bending including hardening effect. Springback was also determined by experimental testing and the results obtained are compared with analytical results. The effect of hardening is discussed in the light of the results obtained.

2. SPRINGBACK PREDICTION IN BENDING INCLUDING HARDENING EFFECT IN BEAMS

Suppose a beam is subjected to bending, it is possible to obtain its radius of curvature if the surface strain and thickness of the specimen are known. The radius of curvature after loading and unloading can be obtained using Eq. 1 and Eq. 2.

$$R_o = \frac{h}{2\varepsilon_o} \tag{1}$$

$$R_f = \frac{h}{2\varepsilon_F} \tag{2}$$

where *h* is the depth of the beam and ε_o and ε_f are the surface strains on loading and unloading states respectively. The radii of curvature can also be determined by using Eq. 3.

$$R = \frac{(X_c^{\ 2} + \delta^2)}{2\delta} \tag{3}$$

where δ is the deflection at the middle of the beam and X_c is the distance from the centre of the beam to the outer support point in the case of a four point bend loading configuration. The difference between δ corresponding to loading and unloading gives the springback.

The external moment M is equal to the internal moment [12] which is given by Eq. 4.

$$M = 2\int_0^{h/2} \sigma b y dy \tag{4}$$

Let the surface strain after bending be ε_1 as illustrated in Figure 1. The figure also illustrates the stress distribution across the depth of the beam for a general material with hardening behaviour.

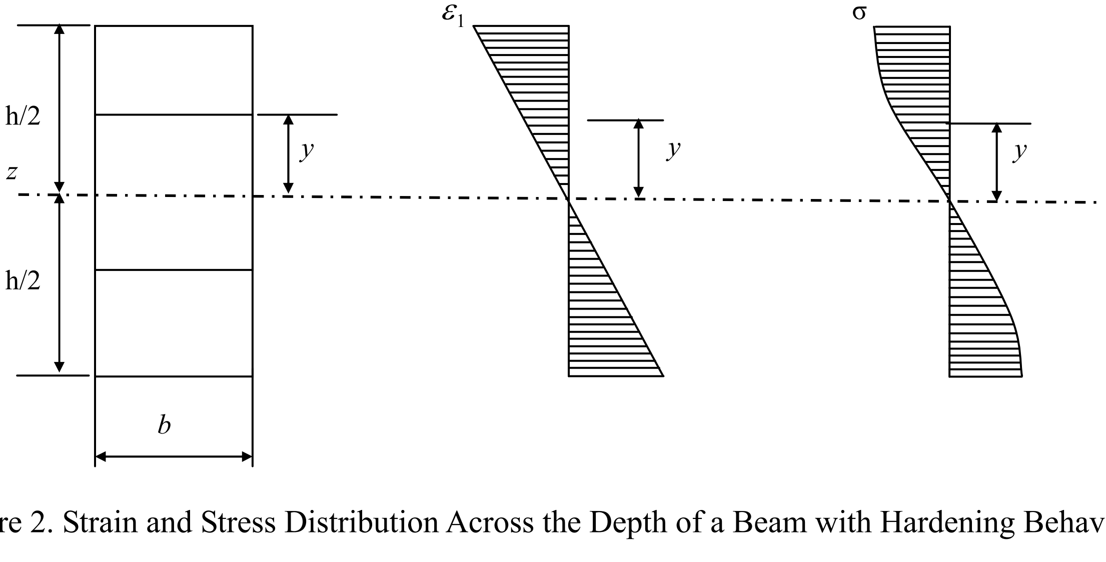

Figure 2. Strain and Stress Distribution Across the Depth of a Beam with Hardening Behaviour

By transforming from the independent variable y to strain ε we have from Figure 2 $y = h\varepsilon/(2\varepsilon_1)$ and $dy = hd\varepsilon/(2\varepsilon_1)$. Eq. 4 can now be written as Eq. 5:

$$M = \frac{bh^2}{2\varepsilon_1^2}\int_0^{\epsilon_1} \sigma\varepsilon d\varepsilon \tag{5}$$

Let the stress strain for a general material behaviour be represented by a form of the Ludwik equation [13] as given in Eq. 6 below.

$$\sigma = \begin{cases} E\varepsilon & \varepsilon \le \varepsilon_y \\ Y \quad \text{for} & \varepsilon_y < \varepsilon \le \varepsilon_t \\ K\varepsilon^n & \varepsilon_t \le \varepsilon \le \varepsilon_1 \end{cases} \tag{6}$$

Then the moment can be re-written as:

$$M = \frac{bh^2}{2\varepsilon_1^2}\left[\int_0^{\epsilon_y}(E\varepsilon)\varepsilon d\varepsilon + \int_{\epsilon_y}^{\epsilon_t} Y\varepsilon d\varepsilon + \int_{\varepsilon_t}^{\varepsilon_1}(K\varepsilon^n)\varepsilon d\varepsilon\right] \tag{7}$$

By using $\varepsilon_y = Y/E$, $\varepsilon_1 = h/(2R)$ and simplifying Eq. 7 we have Eq. 8

$$M = 2bR^2E\left[-\frac{1}{6}\left(\frac{Y}{E}\right)^3 + \frac{1}{2}\left(\frac{Y}{E}\right)\varepsilon_t^2 + \frac{K}{(n+2)E}\left(\frac{h}{2R}\right)^{n+2} - \frac{K}{(n+2)E}\varepsilon_t^{n+2}\right] \tag{8}$$

where ε_t is strain at the end of the yield transition zone. The moment due to springback is also obtained from the relationship $M = EI(1/R_E)$ where E is the Young's modulus of the material, I is the second moment of area and $(1/R_E)$ is the change in curvature. This gives Eq. 9 for a rectangular section.

$$M = E\frac{bh^3}{12}\left(\frac{1}{R} - \frac{1}{R_F}\right) \tag{9}$$

Equating Eqs. 8 and 9 and simplifying gives the ratio of the initial radius, R, to the final springback radius as in Eq. 10.

$$\frac{R}{R_F} = \frac{24K_E R_h^3}{n+2}\left(\varepsilon_E^{n+2} - h_R^{n+2}\right) + 4(R_h Y_E)^3 - 12R_h^3 Y_E \varepsilon_t^2 + 1 \tag{10}$$

Where $K_E = K/E$, $R_h = R/h$, $Y_E = Y/E$ and $h_R = h/(2R)$. Eq. 10 can be shown for $K = Y$ and n = 0 and ε_t equal to strain at first yield (Y/E) to reduce to Eq. 11, which is the elastic perfectly plastic solution derived by Gardiner [6]. For materials such as the EN3B 3 mm thick given in Figure 2, there is no yield transition zone therefore ε_t is also equal to strain at first yield i.e. (Y/E).

$$\frac{R}{R_F} = 4\left(\frac{RY}{Eh}\right)^3 - 3\left(\frac{RY}{Eh}\right) + 1 \tag{11}$$

Eq. 11, together with the knowledge of the dimensions and the properties of the material, i.e. *h*, *E* and Y and the initial radius of curvature, *R*, can be used to find the final radius R_F.

The limitations of the equations derived in this paper lie primarily in the assumptions of the underlining theory. The theory assumes that the strain at any point in the beam is proportional to the distance of the point from the neutral axis. This assumption holds provided that the cross-sectional dimensions of the beam are much smaller than the radius of curvature [14], typically less than one-tenth. It should be noted that none of the bending analysis considered in this work exceeded 5% surface strain on the beams. Beyond this limit anti-clastic effect becomes pronounced.

3. MATERIAL

Beams with thicknesses of 1, 3 and 5 mm made of two different materials, CR4 and EN3B steels were tested. All the specimens were annealed in order to relieve any previous residual stresses caused by processing and fabrication. The effects of oxidation were reduced by placing the specimens in a steel foil jacket and wrapped closely to expel air. The annealing was carried out at 660 °C for one hour. The annealing carried out eliminated the need to consider residual stress and Bauschinger effects in the analytical formulation.

Table 1 gives a summary of the Young's modulus E, yield strength σ_y, and the hardening strength and exponent *K* and *n* respectively for the materials. The hardening strength and exponent were determined from the stress strain curves according to ASTM standards [12]. The strain ranges considered were between the end of the yield transition zone and the ultimate tensile strength. This applied particularly to the EN3B 5 mm thick and CR4 1 mm thick materials that have long yield transition zones as can be seen in Figure 1.

The constants *K* and *n* in equation were determined from simple graphical data processing of the stress strain curve for the material of interest. This was done by plotting $\log\sigma$ against $\log\varepsilon$. The slope of the resulting line gives *n* and the intercept is $\log K$ from which *K* can then be found. The value of *n* varies between 0 and 1 for real materials. The values of elastic and hardening properties for the materials used are summarised in Table 1.

Table 1. Summary of the Properties of the Materials Used for Springback Tests in Bending

Material	Thickness	E (GPa)	Y (MPa)	ε_y	ε_t	K(MPa)	n
CR-4	1mm	211	250	0.0011848	0.02699	413	0.1282
EN-3B	3mm	190	450	0.00225	0.00858	708	0.0764
EN-3B	5mm	195	320	0.00164	0.02636	588	0.1530

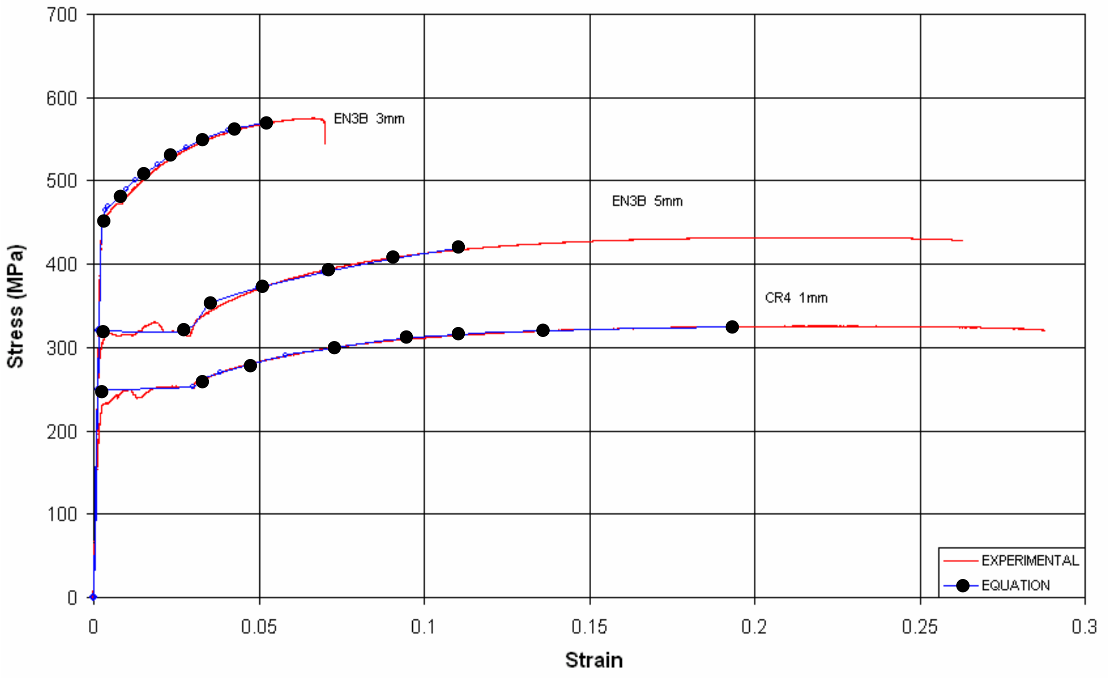

Figure 2. Stress-strain Graphs for the Materials Considered Compared with Those Obtained Using the Material Models in Eq. 6 and K and n Properties Given in Table 1

4. EXPERIMENTAL PROCEDURE FOR THE BEND TESTS

The beams were tested in a four point bending configuration. The internal and external support distances of the four point bend rig were 100 and 200 mm respectively. The beams were nominally loaded to 25 mm deflection which led to plastic deformation in all the beams.

The bending tests were carried out using displacement control. The loading and unloading rate was 0.03mm/sec up to the maximum deflection desired. The specimens were loaded at the maximum deflection for a period of 30 sec and then unloaded at the same rate as for the loading. After bending, the load was released to enable springback to take place. An LVDT was used to determine the deflection during loading and unloading.

5. RESULTS

This section presents the effects of elastic plastic and hardening material behaviour models on the prediction of the springback and on springback ratio R / R_F. However, the effect of these material models on beam response to loading are considered first. The results of experimental tests carried out are also compared with predictions for springback based on the material models. Details are included to assist with the explanation of the observations made. The properties of the materials used in the analyses are as given in Table 1.

5.1 Predicted Effect of Material Models on Beam Response and Springback Ratio

The stress strain curve for the EN3B 3 mm material lends itself to ease of use for comparison of prediction of the effect of hardening using Eqs. 10 and 11. It is helpful to first compare the moments developed based on elastic perfectly plastic and hardening material behaviours. The moments are normalised by dividing by flexural stiffness *EI*, where *E* is Young's modulus and *I* is second moment of area. The results are presented in Figure 3 against different extents of surface strain during bending. The difference between results for both is compared in percentage relative to that of the hardening behaviour also in Figure 3. The difference between both moments can be seen to increase with increasing load or surface strain as to be expected.

Figure 4 shows the prediction of springback ratio R / R_F against R/h. The prediction based on elastic perfectly plastic behaviour is very similar to that of the hardening behaviour and can hardly be differentiated in a plot of both results. The figure shows the difference to vary from about -8% to 4% relative to the prediction based on the hardening model. This difference is relatively low compared to the difference seen in the values of moments for a given level of surface strain. This apparent anomaly can be explained by expressing the difference in springback ratios in terms of the moment based on the two material models. This is given by Eq. 12.

$$\left(\frac{R}{R_f}\right)_h - \left(\frac{R}{R_f}\right)_{ep} = \frac{R\Delta M}{EI} \tag{12}$$

where subscripts *h* and *ep* are used to denote hardening and elastic perfectly plastic material behaviour models. The term on the right hand side of Eq. 12 is a product of two components *R* and *ΔM* that vary inversely as surface strain increases. Whereas *ΔM* increases as surface strain increases, *R* decreases. This implies that increasing value of the moment does not necessarily translate to high values in R_F.

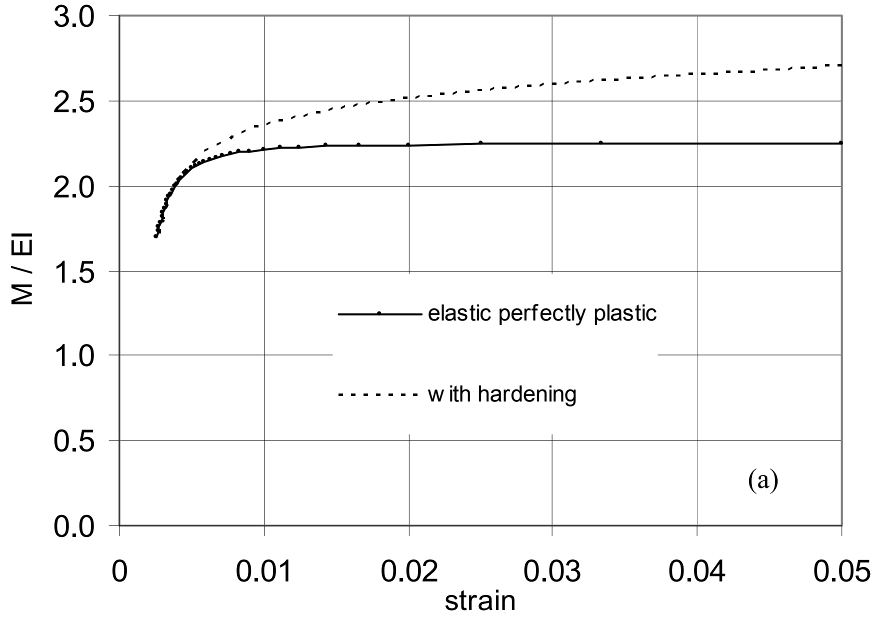

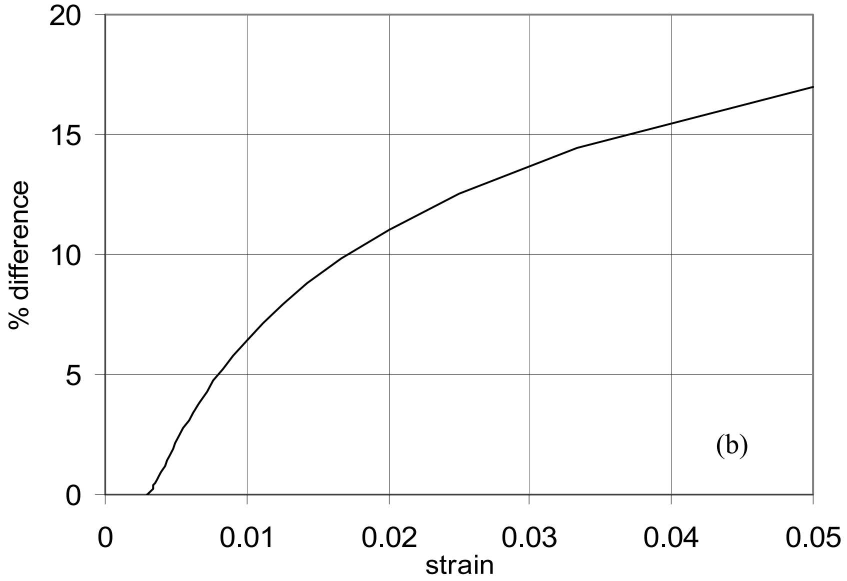

Figure 3. The Plot of Comparison of Results of Elastic Plastic and Hardening Material Models with Increasing Loading or Surface Strain for (a) Normalised Moments and (b) Percentage Difference Between the Moments

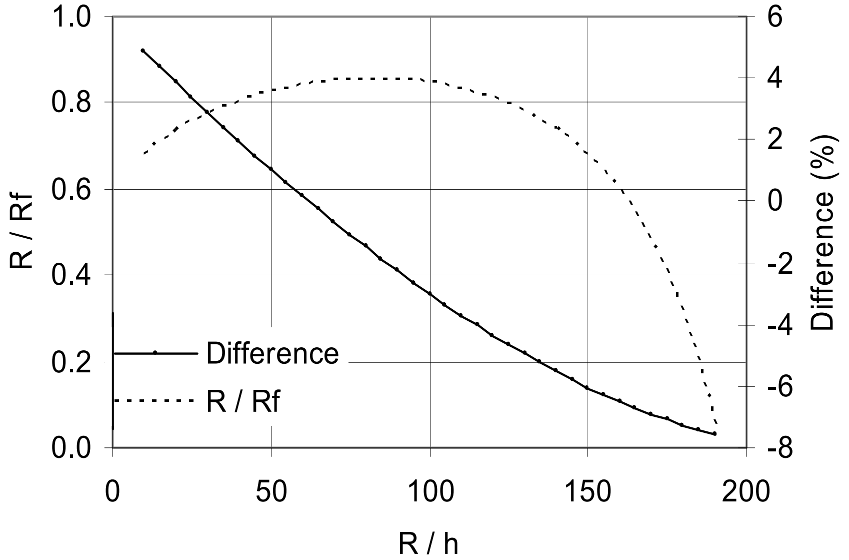

Figure 4. Prediction of Springback Ratio Using the Hardening Equation for EN3B 3 mm Thick

6. COMPARISON OF PREDICTED SPRINBACK RATIO WITH EXPERIMENTAL RESULTS

The main aim of this paper is to test the new general solution presented in this work for material behaviour for springback in beams using theoretical and experimental analyses. Three sets of tests were carried out on specimens with thicknesses of 1, 1.5 and 3 mm.

The radius of curvature obtained using Eq. 11 based on deflection after loading and unloading and taking ratios is plotted in Figure 5 for the three materials considered. Three experimental test results are also plotted in the figure and shows good agreement. Table 2 also shows comparison of experimental and prediction for springback using the hardening equation.

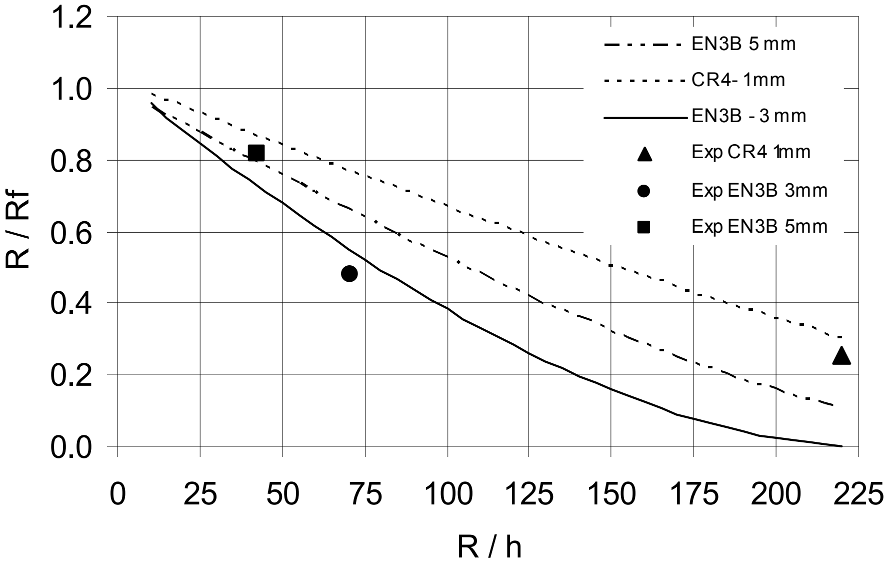

Figure 5. Prediction of Springback Ratio Using the Hardening Equation and Experimental Results

As results in Table 2 show, both Gardiner's solution and the new solution give same results for the CR-4 and EN-3B 5 mm thick materials. In these cases, the surface strains were below the yield transition strain limit. This means that the materials were still in the elastic perfectly plastic range. Hence the two solution methods being the same in this state gave the same prediction. The results are however different for the EN-3B 3 mm material that exhibits negligible yield transition strain and the surface strain extends into the hardening stage. In this case the new solution is about 5% more accurate compared to the experimental result. It can also be observed from Figure 5 that springback increases with increasing yield strength, thickness and curvature. This is in agreement with work previously reported by other authors [7,11].

Table 2. Comparison of Predicted and Experimental Results for Springback

Material	Thickness (mm)	Surface strain after bending	Experi-mental (mm)	Predicted Gardiner (mm)	Predicted New (mm)	Error Gardiner (%)	Error New (%)
CR-4	1	0.0023	18.2	17.7	17.7	-2.7	-2.7
EN-3B	3	0.0071	13.6	12.1	12.7	-11.0	-6.6
EN-3B	5	0.0118	5.1	5.6	5.6	9.8	9.8

7. CONCLUSIONS

An equation for predicting springback in bending including the effect of hardening has been presented. For a given bend radius R, the new equation presented provides a means to predict the springback radius R_F more accurately for a general non-linear material behaviour than the existing elastic perfectly plastic solution. However, although the result of the analyses carried out shows that hardening increases the moment required for forming the materials considered, it also shows that this does not translate proportionally to as much change in springback ratio. Experimental results obtained show good agreement generally with the predictions made for springback especially in the case where the material deformed beyond the yield transition strain into the hardening regime.

ACKNOWLEDGEMENTS

A López Castro will like to acknowledge the support of the Mexican Government through CONACyT, for his scholarship.

REFERENCES

[1] Chapman, F.B., Hazlett, T.H. and Schroeder, W.M., “Springback in Flanging”, Product Engineering, 1942, Vol. 13, pp. 382-383.
[2] Carden, W.D., Geng, L.M., Matlock, D.K. and Wagoner, R.H., “Measurement of Springback”, International Journal of Mechanical Sciences, 2002, Vol. 44, pp. 79-101.
[3] Sturm, R.G. and Fletcher, B.J., “Determining Springback-I”, Product Engineering, Oct. 1941, pp. 526-528.
[4] Sturm, R.G. and Fletcher, B.J., “Determining Springback-II”, Product Engineering, Nov. 1941, pp. 590-594.
[5] Schroedes, W., “Mechanics of Sheet-Metal Bending”, Transaction of ASME, Nov. 1943, pp. 817-827.
[6] Gardiner, F.J., “The Spring Back of Metals. Transaction of ASME, Jan. 1957, pp. 1-9.
[7] Hosford, W.F. and Caddell, Robert M., “Metal Forming Mechanics and Metallurgy. Englewood Cliffs”, N.J. 07632, Prentice-Hall, Inc. 1983.
[8] Kalpajian, Serope, “Manufacturing Engineering and Technology”, Illinois Institute of technology, Addison-Welsey Publishing Company, 1989.
[9] Johnson, W. and Mellor, P.B., “Engineering Plasticity”, London, Van Nostra Reinhold company, 1980.
[10] Taylor, L., Cao, J., Karafillis, A.P. and Boyce, M.C., “Numerical Simulation of Sheet-metal Forming”, Journal of Materials Processing Technology, 1995; Vol. 50, pp. 168-179.
[11] Esat, V., Darendelier, H. and Gocler, M.I., “Finite Element Analysis of Springback in Bending of Aluminium Sheets”, Materials & Design, 2002; Vol. 23, pp. 223-229.
[12] Gere, J.M. and Timoshenko, S.P., “Mechanics of Materials”, PWS Publishing Company, 20 Park Plaza, Boston, Ma. 1997.
[13] Dieter, G.E., “Mechanical Metallurgy”, McGraw Hill, Singapore, 1984.
[14] Ryder, G.H., “Strength of Materials”, Macmillan, London, 1992.

STRENGTH OF MIG WELDED CONNECTIONS IN FIRE EXPOSED ALUMINIUM STRUCTURES

J. Maljaars[1,]* and F. Soetens[2]

[1]*TNO Built Environment*
and Geosciences. Address: TNO; P.O. Box 49; 2600 AA Delft; The Netherlands
Tel +31 15 2763464. Fax. +31 15 2763018
[2]*Eindhoven University of Technology / TNO Built Environment and Geosciences. Address: TNO;*
P.O. Box 49; 2600 AA Delft; The Netherlands
Tel +31 15 2763468. Fax. +31 15 2763018
**(Corresponding author: E-mail: johan.maljaars@tno.nl)*

ABSTRACT: Aluminium alloy structures are sensitive to fire exposure, which is mainly due to the low melting temperature. Yet a complete knowledge of the structural behaviour of aluminium alloys when exposed to fire is not available. This paper focuses on one of the main knowledge gaps, being the strength of aluminium welded connections in fire. Uniaxial tensile tests were carried out at elevated temperatures on welded and unwelded aluminium samples of alloys 5083-H111, 6060-T66 and 6082-T6. All welded samples failed outside the weld itself. It is concluded that the difference in strength between the heat affected zone and the parent metal decreases with increasing temperature.

Keywords: Fire design, heat affected zone, treatment, precipitation hardening

---

1. INTRODUCTION

Aluminium alloys are widely used in structures such as boats, trains, parts of drill platforms (mainly the helicopter deck and the living quarters) and roofs with large spans. The main reason for applying aluminium alloys in these structures is often the high ratio between strength and density. One of the aspects that should be checked in the design of these structures is fire resistance.

The strength of most commercially applied aluminium alloys reduces from 90 % to 20 % of the strength at room temperature at temperatures between 150 ºC and 350 ºC (Lundberg [1]). These temperatures are low for fire exposure: the standard temperature-time curve (ISO 834) gives a gas temperature after 30 minutes of 840 ºC. Besides, aluminium alloy members heat up relatively fast, mainly because of the high thermal conductivity (110-250 W/mK for most alloys, Kammer [2]). This makes aluminium alloy structures sensitive to fire exposure. Many aluminium structures have to be insulated in order to meet fire resistance requirements (Maljaars et al. [3]).

Because of the sensitivity to fire of aluminium alloys, fire design is a major aspect in the total design of aluminium structures for which requirements are set on the fire resistance (such as the structures mentioned above). The most up-to-date standard for structural fire design of aluminium structures is Eurocode 9, Part 1-2 (EN 1999-1-2 [4]). However, the standard does not give a complete set of verification rules for all possible failure mechanisms of structures and structural components. This is due to a lack of fundamental research concerning these failure mechanisms.

This paper focuses on one of the knowledge gaps, being the strength of welds when exposed to fire. If the design is performed applying simple calculation models, EN 1999-1-2 [4] states that the connection need not be checked, provided that the thermal resistance of the fire protection at the connection is equal to or larger than the thermal resistanceof the fire protection of the adjacent member (It is implicitly assumed that the design of the members and connections at ambient temperature is correct, e.g. based on EN 1999-1-1 [5], and that the utilisation of the connection is not higher than the utilisation of the connected members). Research has been carried out to verify

this statement for welded aluminium structures.
The paper starts with the state-of-the-art design of welded connections. Subsequently, results of a literature survey into the strength of alloys at elevated temperature are discussed. Finally, results of tests carried out on the strength of welded aluminium alloy specimens at elevated temperature are given and discussed.

In order to comprehend the data and discussions in this paper, background information on the treatment options and strength enhancement of aluminium alloys is a prerequisite. This information is provided in text books such as Altenpohl [6], or articles such as Gitter [7].

2. STATE OF THE ART: STRENGTH OF ALUMINIUM MIG WELDED CONNECTIONS AT ROOM TEMPERATURE

2.1 Qualitative Explanation of the Relative Strength of the Heat Affected Zone and the Weld Metal

MIG welding is currently the most commonly used welding process for the structures mentioned in the introduction. In this welding process, two members are joined by melting the parent metal, while adding a suitable filler metal. The MIG welding process results in two potentially weak parts of the connection, being:

1. The weld metal itself, which is a mixture of parent metal and filler metal. This weld metal may have a lower strength than the parent metal.
2. The zone that is affected by the heat input of the welding process (the heat affected zone, HAZ). Due to the heat input of the welding process, recovery and overageing or annealing reduce the strength compared to treated (hardened) parent metal (see the Annex).

Figure 1 gives an overview of the hardness of the HAZ.

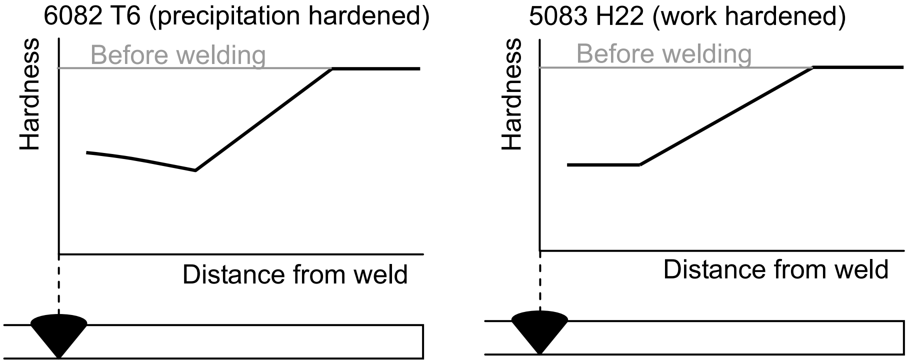

Figure 1. Hardness of the HAZ of Alloys 6082-T6 and 5083 H22 (After Dwight [8])

2.2 Strength Design Values in Eurocode 9, Part 1-1

Aluminium alloys have a curved stress-strain (σ-ε) relationship. In most standards, the value of the 0.2 % proof stress $f_{0.2}$ (i.e. the stress at a plastic strain of 0.2 %) is applied in the verification rules for the structural design of aluminium structures at room temperature. Among these standards is Eurocode 9, Part 1-1 (EN 1999-1-1 [5]).

For the weld metal and the HAZ at connections, however, the ultimate tensile strength f_u may be applied in the verification rules in EN 1999-1-1. Thus, plastic deformation is allowed over the small length of the weld zone and the HAZ. As an example, Figure 2 gives the stress-strain curves resulting from tests for the parent metal, the HAZ and the weld metal of alloy 6082-T6. Especially for precipitation hardened alloys, f_u of the HAZ (or weld metal) is in many cases lower than $f_{0.2}$ of the parent metal.

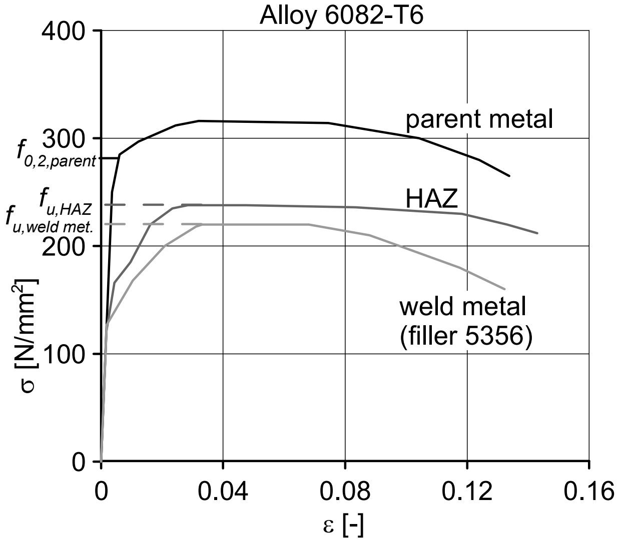

Figure 2. σ-ε Relationship of Parent Metal, Heat Affected Zone and Weld Metal According to Tests on Alloy 6082-T6 (Thickness 4 mm, Filler Metal 5356. Source: Soetens [9])

3. LITERATURE SURVEY: STRENGTH OF PARENT METAL AT ELEVATED TEMPERATURE

3.1 Data Sources

In order to determine the constitutive properties at elevated temperature, two types of (uniaxial tensile) tests can be carried out:

1. *Steady state tests.* The specimen is subjected to a constant, elevated temperature in time, while a certain strain rate is applied (i.e. a displacement-controlled test). The actual test is preceded by a period with a constant temperature equal to the test temperature (the thermal exposure period).
2. *Transient state tests.* The test is carried out at a certain stress level and an increasing temperature in time. The deformation (strain) is monitored. Usually, a constant heating rate and a constant stress level in time are applied.

Although transient state tests are widely considered as being more appropriate for fire design, only the results of steady state tensile tests are found in literature for aluminium alloys. The strength data in EN 1999-1-2 are also based on steady state tests (Lundberg [1]). Steady state tensile tests on various alloys with various exposure periods are reported in Voorhees and Freeman [10] and Kaufman [11]. The alloys incorporated in these reports are limited to those frequently applied in the USA. Tensile tests on alloy 6082, frequently applied in Europe, are reported in Hepples and Wale [12] and Langhelle [13]. These test results are discussed in this section, separately for precipitation hardened (6xxx series) and for work hardened (5xxx series) alloys.

It has been shown in many tests, e.g. Kumar and Swaminathan [14] and Van den Boogaard [15], that the stress-strain relation depends on the strain rate applied in a steady state tensile test, especially at elevated temperatures. At elevated temperatures, a higher strain rate results in a higher strength. The strain rate applied in the tests mentioned above is in most cases approximately 0.005 / min up to yielding and 0.05 to 0.10 / min up to rupture.

Maljaars et al (Heron [16]) showed that the strength degradation is approximately equal for alloys in the same series and temper.

3.2 Precipitation Hardened Alloys

As an example, the reduction of $f_{0.2}$ as a function of the temperature θ of the precipitation hardened alloy 6063 is given in Figure 3a. The strength of artificially aged tempers (T5-T9, see the Annex) reduces fast with temperature. Contrarily, the strength of naturally aged tempers (T1-T4) increases at moderately elevated temperatures, which is attributed to artificial ageing. At higher temperatures, the strength of artificially and of naturally aged tempers are (almost) equal to one another. At even higher temperatures, the strength of precipitation hardened tempers approaches that of the alloy in annealed temper.

The data in the literature show that the strength depends on the thermal exposure period in case of precipitation hardened alloys. This is due to the fact that the influence of overageing is a function of the time at elevated temperature.

3.3 Work Hardened Alloys

An example of the reduction of $f_{0.2}$ as a function of θ of the work hardened alloy 5052 is given in Figure 3b. The strength of the work hardened temper reduces faster than the strength of the annealed temper. The difference in strength for different tempers reduces as the temperature increases. This is attributed to recovery and annealing. The data in literature show that the strength of most work hardened alloys is independent of the thermal exposure period, for the tests carried out with a thermal exposure period of 30 up to 600 minutes.

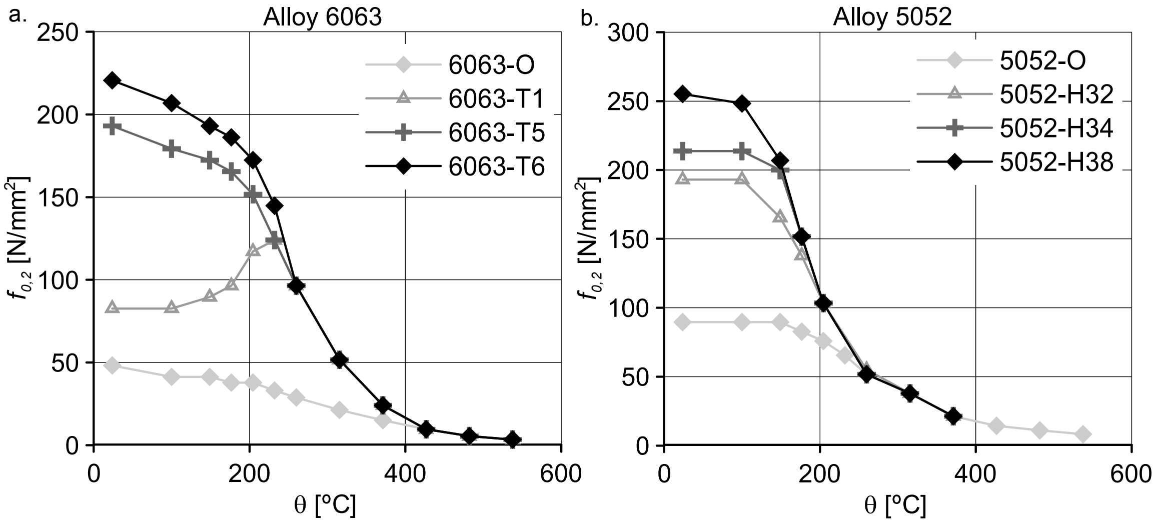

Figure 3. $f_{0.2}$ as Function of θ for a. Alloy 6063-T6 and b. Alloy 5052 (Data source: Kaufman [11]. The Data Shown are Average Values Resulting from a Large Number of Tests. The Design Values for $f_{0.2}$ are Lower. The Results for Temper T1 are also Representative for T4.)

Considering all the data found in literature, it is concluded that work hardening and/or precipitation hardening may increase the strength in a substantial way at room temperature, but it has almost no effect at temperatures above 150-200 ºC (i.e. the relevant temperatures for fire design). The favourable metal structure obtained by the treatment is (partially) destroyed when exposed to an elevated temperature either during a minimum period of time or at a sufficiently high temperature. This is similar to the influence of welding.

4. TESTS: STRENGTH OF WELDS AT ELEVATED TEMPERATURE

4.1 Fire Resistance of Connections According to Standards

A simple calculation model in EN 1999-1-2 [4] states that the fire resistance of the connections need not be checked, provided that the thermal resistance of the fire protection at the connection is equal to or larger than the thermal resistance of the fire protection of the adjacent member, as mentioned before in the introduction. A similar statement is made in Eurocode 3, Part 1-2 (EN 1993-1-2 [17]) for the fire design of steel structures. The statement is based on the fact that, if the above condition of the fire protection is fulfilled, the temperature development of, for example, beam to column connections is usually behind the temperature development of the adjacent members (Franssen and Zacharia [18]).

This statement may be justified for simple calculation models of steel members. The specific strength characteristics of aluminium welds, with its filler metal and heat affected zones, however, may require a different approach. Besides, in the case of advanced calculation models, restrained thermal expansion and changing stiffness ratios of the adjacent members have to be taken into account. In such cases it is necessary to know the strength of the connection in more detail.

In order to determine the strength of the HAZ and the weld metal in relation to the parent metal, uniaxial tensile tests need to be carried out on specimens with and without welds.

4.2 Test Programme

Three types of specimens were used in the test programme:

a) *Specimens without welds*. The specimens are flat, so-called disproportional specimens, with dimensions according to Figure 5a. The tests on these specimens are referred to as "reference tests".

b) *Specimens with fillet welds*. The specimens consist of two parts, with a horizontal plate welded in between (Figure 5b). The fillet welds are overmatched, so that rupture does not take place at the weld itself. These specimens are indicated with "fillet weld specimens".

c) *Specimens with butt welds*. The specimens consist of two parts, welded together with an X-shaped weld (Figure 5c). Due to the MIG welding process, the weld throat is slightly larger than the specimen thickness. In conformity with custom practice for the structures mentioned in the introduction, the welds are as fabricated. The indication is "butt weld specimens".

All welded specimens were cut from a larger, welded plate (Figure 6), so that start-stop positions are not present in the specimens.

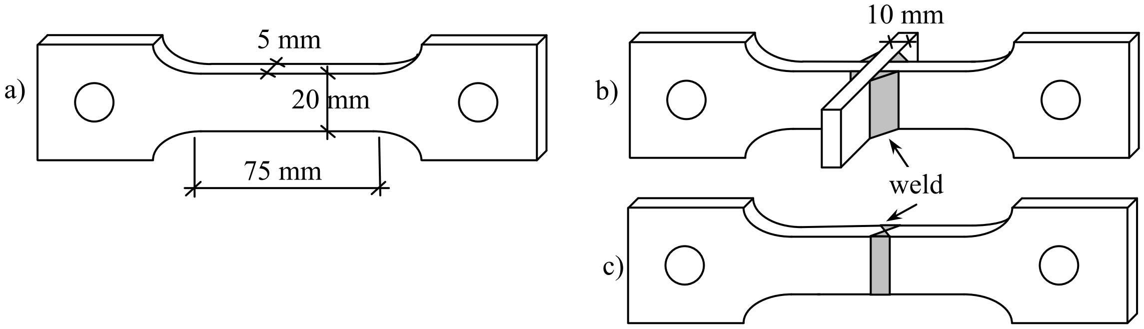

Figure 5. Overview of Tested Specimens for the Strength Measurements

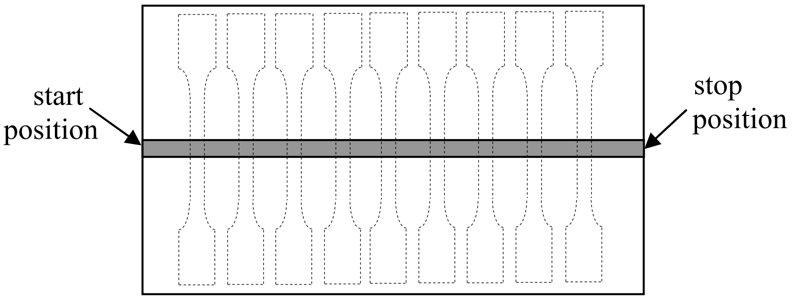

Figure 6. Production of the Specimens from a Larger, Welded Plate

Two types of tests were applied:

- Steady state tests carried out at 20 ºC, 200 ºC and 300 ºC. The elevated temperatures were selected such that the temperature range relevant for fire design was covered. The test procedure applied in the tests was as follows:

  1. Heating the specimen from room to test temperature in approximately 25 minutes.
  2. Maintaining the test temperature constant for approximately 15 minutes.
  3. Applying a certain strain rate (cross-head motion) until rupture occurred. In agreement with EN 10002-5 [19], the strain rate measured over the parallel length was 0.006 /min in the elastic range and then gradually increased to 0.03 /min at the ultimate resistance.

- Transient state tests, carried out with constant heating rates of 6 and 12 ºC/min. These heating rates are representative for heating of fire exposed insulated aluminium members. The stress applied in the transient state test was equal to the ultimate tensile strength determined in the steady state tests on the reference specimens at 300 ºC. Only a limited number of transient state tests were carried out. The purpose of these tests was to check whether the conclusions of the steady state tests also apply to transient state conditions.

Three alloys were used in the test programme:

- Alloy 5083-H111. Temper H111 indicates that this alloy is almost in annealed temper (O). The filler weld metal is alloy 5356;
- Alloy 6060-T66. This is a fully heat treated (precipitation hardened, artificially aged) alloy, with higher strength values than the alloy in temper T6. The filler metal is alloy 4043;
- Alloy 6082-T6. The filler metal is alloy 4043. Only steady state tests on reference specimens and butt weld specimens were carried out on this alloy.

The test program is summarised in tables 1 and 2. The number of tests is indicated between brackets

Table 1. Overview of Steady-state Test Program

Test temp.	a) reference spec.	b) fillet weld spec.	c) butt weld spec.
20 ºC	5083 (3) 6060 (3) 6082 (2)	5083 (3) 6060 (3)	5083 (2) 6060 (2) 6082 (2)
200 ºC	5083 (4) 6060 (3) 6082 (2)	5083 (3) 6060 (2)	5083 (2) 6060 (2) 6082 (2)
300 ºC	5083 (3) 6060 (3) 6082 (2)	5083 (2) 6060 (2)	5083 (2) 6060 (2) 6082 (2)

Table 2 Overview of transient state test program

Heating rate	a) reference spec.	b) fillet weld spec.	c) butt weld spec.
6 ºC/min	5083 (1) 6060 (1)	6060 (1)	5083 (1)
12 ºC/min	5083 (1) 6060 (1)	5083 (1) 6060 (1)	

4.3 Test Set-up

The tests were carried out in a conventional electrical furnace, with an actuator supplied with a 100 kN load cell outside the furnace. The force was transmitted by means of a bar that penetrates the furnace wall. Figure 7 gives an overview of the test set-up.

Thermocouples were used for measuring the temperature at the upper part, the centre and the lower part of the parallel length of the specimens. The furnace temperature was controlled in such a way, that the measured temperature of the specimen was in accordance with the specifications in tables 1 and 2. The temperature of the upper part of the parallel length was approximately 2 ºC warmer than the lower part in all tests at elevated temperature.

4 linear variable differential transformers (LVDTs) outside the furnace were used for determining the axial deformation. The measured length was equal to 50 mm, applied at the upper part of the parallel length of 75 mm (Figure 8). The measured length was outside the centre of the specimen, because rupture was expected in the upper part of the specimen due to the slightly higher temperature in the upper part. A clamp was applied around the specimen, in such a way that the displacements of the lower and the upper side of the measured length were measured at both sides of the specimen (i.e. 4 displacement measurements per specimen). Invarsteel pins were applied between the clamp inside the furnace and the 4 LVDTs outside the furnace (Figure 8).

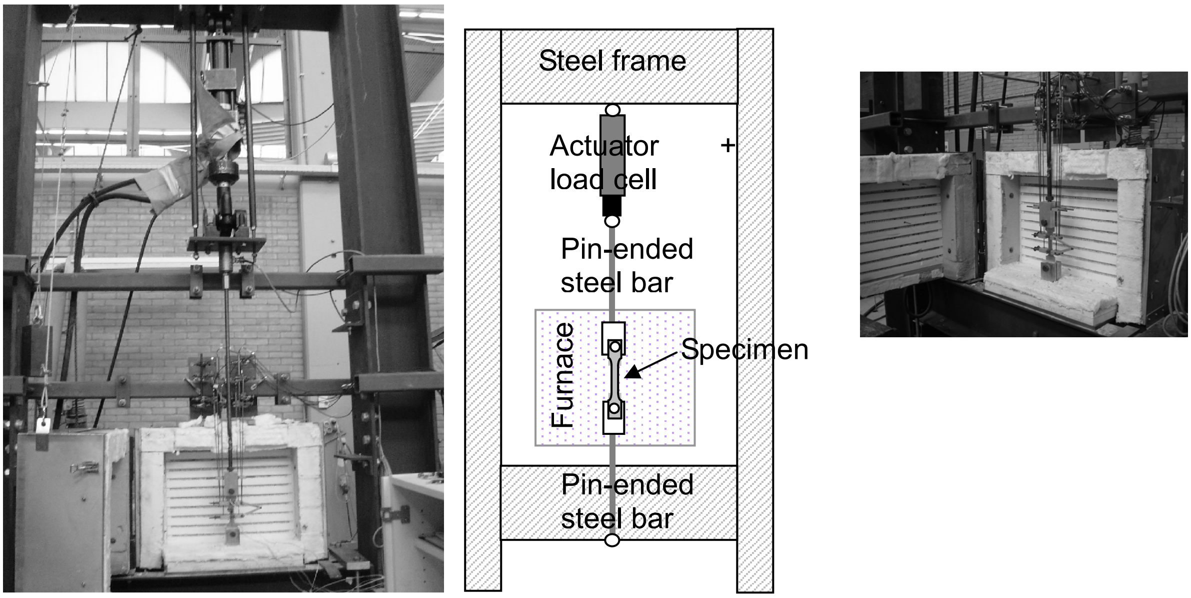

Figure 7. Overview of the Test Set-up

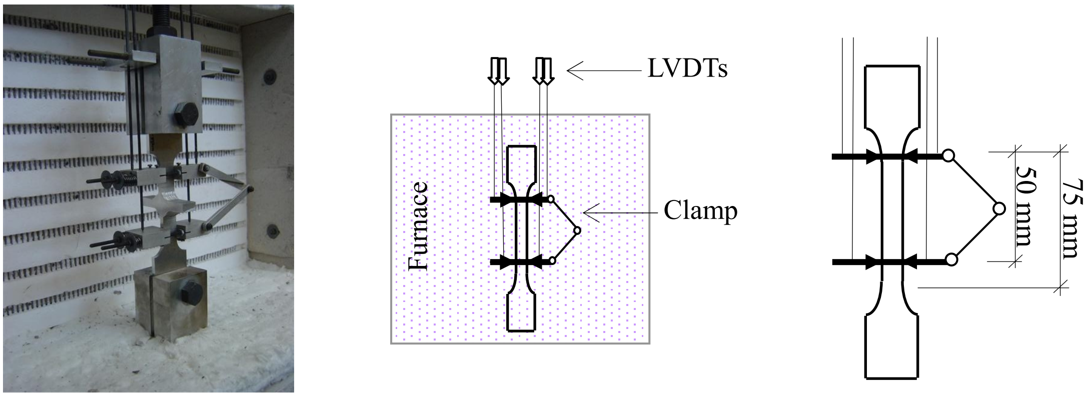

Figure 8. Specimen with the Clamp for the LVDTs

With this measurement system, the displacements of the steady state tests could be determined with sufficient accuracy, as the temperature was constant during these tests. For transient state tests, however, the measurements on the mechanical displacements of the specimens was less accurate, due to the thermal expansion of the measurement devices and specimens during these tests.

The strain at rupture could not be determined accurately, as the clamp lost contact with the specimens due to thermal expansion of the clamp and lateral contraction of the specimen. However, this research focused on the ultimate tensile strength.

4.4 Test Results

Steady State Tests

The tests carried out at the same temperature resulted in equal σ-ε relationships. The difference in ultimate tensile strength between the steady state tests carried out was on average 4 N/mm^2 (2.5 %) and maximum 11 N/mm^2. Thus the tests are well reproducible.

Figure 9 gives the σ-ε relationships of a selection of the steady-state tests on alloy 5083-H111. As the temperature increased, the amount of strain hardening and the homogeneous strain decreased. This was found for all specimens and all alloys of the test program.

Figure 10a. gives the ultimate tensile strength f_u as a function of the temperature θ for the reference and the welded specimens of alloy 5083-H111. For reasons of comparison, the Figure also gives the strength data of the parent metal of alloy 5083-O according to Kaufman [11].

Note that alloy 5083-H111 is (almost) not treated. Both at room and at elevated temperature, the strength of the welded specimens was approximately equal to that of the reference specimens.
At room temperature, rupture took place in the centre of the specimens, both for the reference and the welded specimens. At elevated temperatures (200 and 300 ºC), rupture occurred in the upper part of the specimens, where the temperature was slightly higher (Figure 10b.). This means that the welded specimens failed outside the HAZ at elevated temperature.

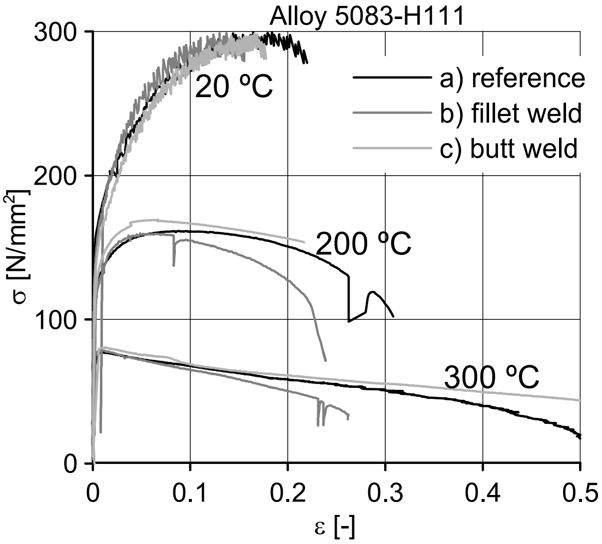

Figure 9. σ-ε Relationships for Alloy 5083-H111

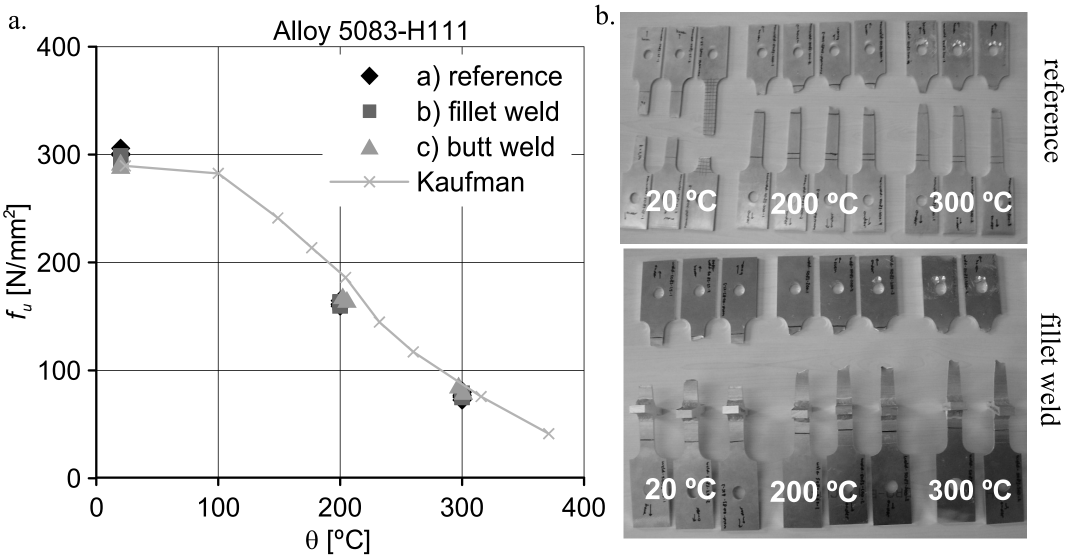

Figure 10. Test Results of Specimens of Alloy 5083-H111
(a. f_u as Function of θ; b. Specimens after Testing)

Figure 11a gives f_u as a function of θ for the specimens of the artificially aged alloy 6060-T66. There was a substantial difference in f_u between the welded and reference specimens at room temperature. This difference in strength decreased with increasing temperature. At 300 ºC, the strength of the welded specimens was approximately equal to that of the unwelded specimens. There was no significant difference in strength between the fillet weld specimens and the butt weld specimens.

All specimens failed near to the centre of the specimen (i.e. in the HAZ) at room temperature. At 200 ºC, rupture took place in the upper part of the parallel length for the reference specimens, whereas the welded specimens failed in the HAZ. Rupture took place at the upper part of the parallel length (i.e. outside the HAZ) in the case of welded and reference specimens at 300 ºC (Figure 11b.)

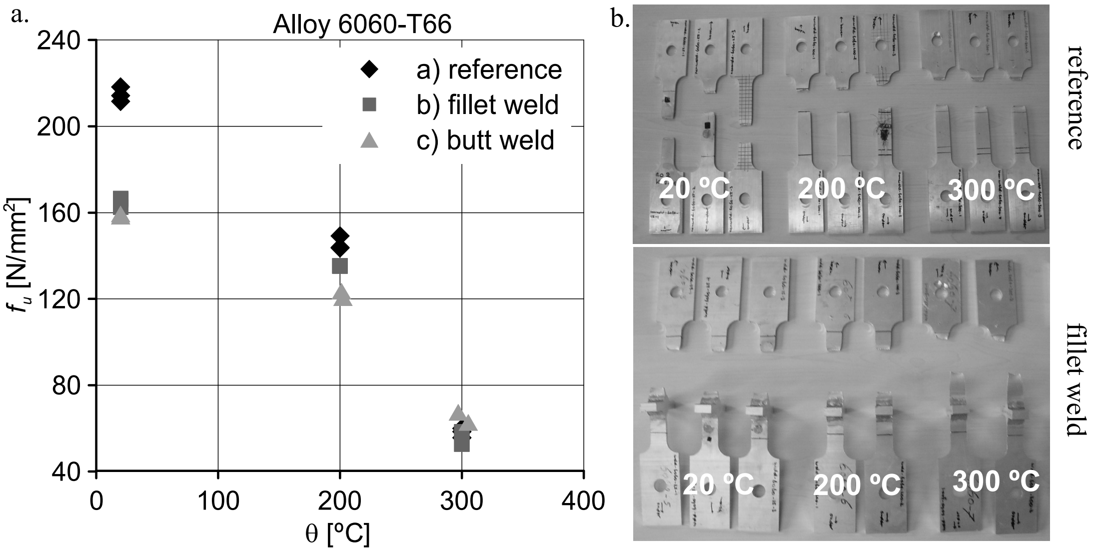

Figure 11. Test Results of Specimens of Alloy 6060-T66
(a. f_u as Function of θ; b. Specimens after Testing)

Figure 12a. gives f_u as a function of θ for the specimens of the artificially aged alloy 6082-T6. For reference, the Figure also gives the strength according to tests on parent material carried out by Langhelle [13]. There was a large difference in f_u between the welded and reference specimens at room temperature. This difference in strength decreased with increasing temperature, but a difference in strength remained present for all test temperatures. For the welded specimens, rupture took place in the heat affected zone at all test temperatures (Figure 12b).

All welded steady-state specimens failed outside the weld metal, both at room and at elevated temperatures.

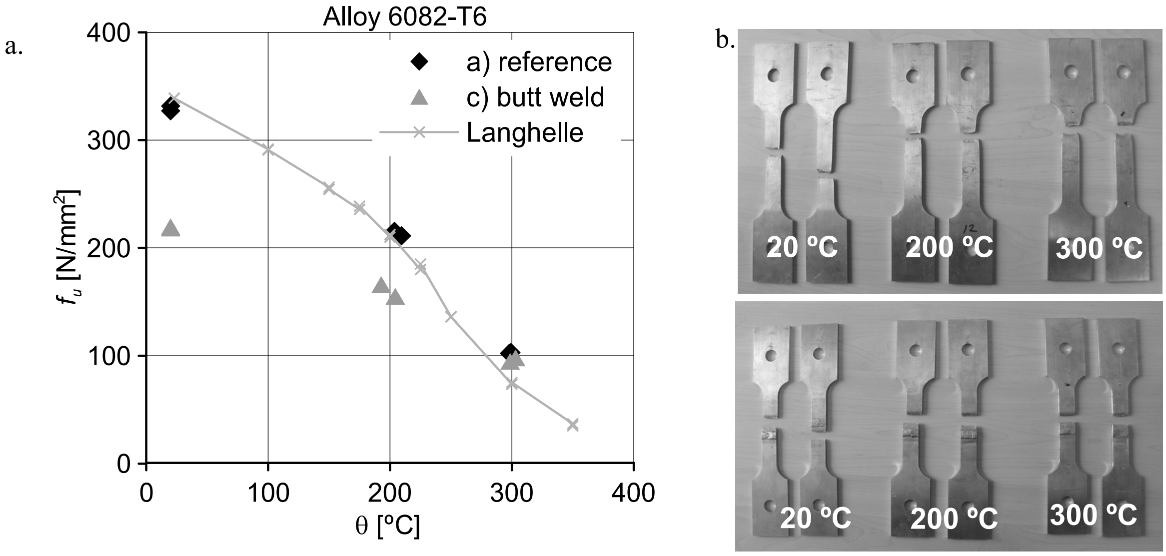

Figure 12. Test Results of Specimens of Alloy 6082-T6
(a. f_u as Function of θ; b. Specimens after Testing)

Transient State Tests

The transient state tests were carried out with a stress level equal to f_u of the steady state tests at 300 ºC. Figure 13 gives the mechanical strain in axial direction as a function of the temperature of the tests carried out. The strain development was almost equal for the welded and the reference specimens.

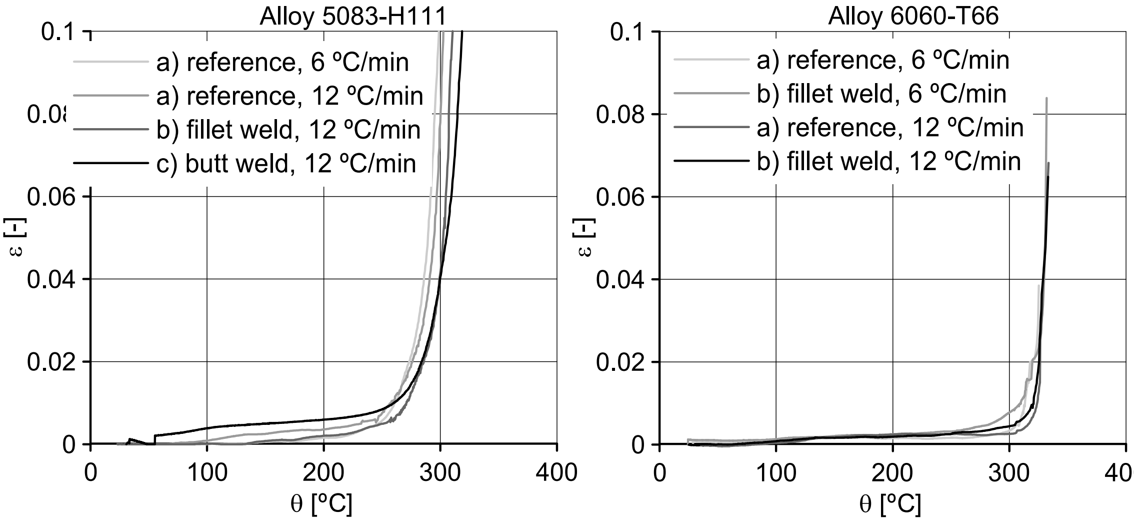

Figure 13. Axial Strain as a Function of the Temperature for the Transient State Tests
(a. Alloy 5083-H111, b. Alloy 6060-T66)

All welded transient-state specimens failed outside the weld metal.

4.5 Discussion of the Results

The weld throat of the fillet weld specimens was chosen such that the specimens would not fail at the weld. For the butt weld specimens, however, the weld throat was determined by the specimen thickness.

None of the tested specimens failed at the weld itself. This means that the weld itself is not decisive for the strength in the case of butt weld specimens with the applied combinations of alloy and filler metal and the applied overmatch of the weld throat: The weld throat was approximately 5.5 mm and the plate thickness was 5 mm.

The strength of the reference specimens represented the strength of the parent metal. The strength of the welded specimens is considered to represent the strength of the HAZ. The strength of the HAZ is considered to be independent of the weld type (fillet or butt).

The steady-state tests on the artificially aged alloys showed that the difference in strength between welded and reference specimens decreased as the temperature increased. This is attributed to the fact that the favourable structure of treated alloys is already destroyed by welding in the HAZ, so that heating by fire has a smaller impact than in case of treated parent metal. This is in agreement with the conclusion drawn in section 3, that work hardening and/or precipitation hardening has almost no influence on the strength at temperatures above 150-200 ºC. The transient state tests also showed an almost equal failure temperature for the parent metal and for the heat affected zone.

In conformity with EN 1999-1-1, the ratio between f_u of the HAZ and f_u of the parent metal is denoted with $\rho_{u,haz}$. Figure 14 a. gives $\rho_{u,haz}$ resulting from the tests as a function of the temperature. The values specified in EN 1999-1-1 for $\rho_{u,haz}$ at room temperature are 0.56 for alloy 6060-T66 and 0.64 for alloy 6082-T6. $\rho_{u,haz}$ in the standard agrees well with that of the tests for alloy 6082-T6. For alloy 6060-T66, however, $\rho_{u,haz}$ resulting from the tests is higher than the value in the standard.

The partial factor for $f_{0.2}$ of the parent metal at room temperature in EN 1999-1-1 is equal to γ_{M1} = 1.1. For f_u of the HAZ at room temperature, the partial factor is equal to γ_{M2} = 1.25. The HAZ is not decisive in the design if the following condition is fulfilled:

$$\frac{f_{u,haz}}{f_{0,2,parent}}\frac{\gamma_{M1}}{\gamma_{M2}} > 1 \quad \Rightarrow \quad \frac{f_{u,haz}}{f_{0,2,parent}} > 1.136 \tag{1}$$

The partial factor for material properties for fire is equal to $\gamma_{M,fi}$ = 1.0.

Figure 14b. gives the ratio $f_{u,\mathrm{HAZ}} / f_{0.2,\,parent\ metal}$ as a function of the temperature for the artificially aged alloys. This ratio increases for increasing temperature in case of alloy 6060-T66. For alloy 6082-T6, this ratio is slightly smaller at 200 ºC compared to the test at room temperature. However, the ratio according to the tests at 200 ºC (ratio = 0.76) is still larger than this ratio at room temperature according to EN 1999-1-1 (ratio = 0.74). At 300 ºC, the HAZ is (almost) not decisive for both alloys.

The number of tests carried out was limited. Moreover, transient state data are missing for aluminium alloys. Therefore, it is considered inappropriate to use the values found for $\rho_{u,haz}$ directly in design. However, it is shown in tests and theoretically explained that $\rho_{u,haz}$ increases with increasing temperature. It is a safe, but conservative approach, to use the same values for $\rho_{u,haz}$ at elevated temperatures as at room temperature.

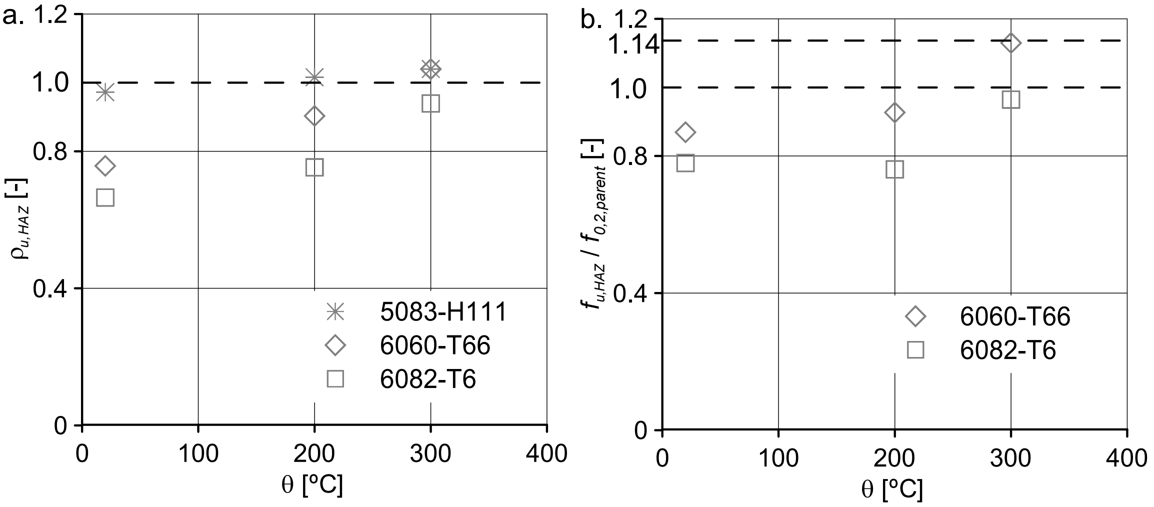

Figure 14. Steady State Strength of the Heat Affected Zone Compared to Steady State Strength of the Parent Metal (a. Ratio $f_{u,HAZ} / f_{u,parent}$; b. Ratio $f_{u,HAZ} / f_{0.2,parent}$)

5. CONCLUSIONS AND RECOMMENDATIONS

The following conclusions are drawn, based on this research:

- In case of treated (hardened) aluminium alloys, the strength of the heat affected zone (HAZ) is lower than that of the parent metal. This is due to the fact that the favourable metal structure obtained by the treatment is (partially) destroyed by the heat input due to welding. In addition, the strength of the weld metal is for a number of alloys lower than that of the parent metal. Consequently, the HAZ or the weld metal are often decisive for the strength of connections in room temperature design, and dimensions of components often depend on the strength of the HAZ or the weld metal.

- The tests carried out at elevated temperature show that the difference in strength between the HAZ and the parent metal decreases with increasing temperature. This is due to the fact that the favourable metal structure obtained by a treatment is already destroyed by the heat input at welding. Consequently, heating by a fire has a smaller impact on the strength of the HAZ than on the strength of the treated parent metal.

- It is a safe but conservative approach to assume that the values for the relative strength of the heat affected zone as given in EN 1999-1-1 for room temperature, $\rho_{u,haz}$, also apply in fire.

- A simple calculation rule in EN 1999-1-2 states that the connection need not be checked, provided that the thermal resistance of the fire protection at the connection is at least as high as that of the adjacent members. In general, the ratio between the ultimate tensile strength of the HAZ and the 0.2 % proof stress of the parent metal ($f_{u,HAZ} / f_{0.2,parent}$) increases slightly with increasing temperature. Therefore, the simple calculation rule in EN 1999-1-2 is justified, at least for the tested alloys (5083-H111, 6060-T66 and 6082-T6). Considering the fact that the strength degradation of alloys in the same series and the same temper is almost equal, it is expected that the simple calculation rule is justified for all 5xxx alloys in annealed temper and all 6xxx alloys in artificially aged temper;

- The tests carried out in this research on butt welded specimens of alloy 5083-H111 with fillet metal 5356, alloy 6060-T66 with fillet metal 4043 and alloy 6082-T6 with fillet metal 4043, show that the weld metal is not decisive for the strength, both at room and at elevated temperature.

The conclusions in this paper are based on a limited number of tests on three often applied aluminium alloys. It is therefore considered inappropriate to implement the data resulting from this test program in EN 1999-1-2 without further research. It is recommended to carry out a larger test programme, which should be focussed especially on transient state tests.

The simple calculation rule in EN 1999-1-2 - the connection need not be checked provided that the thermal resistance of the fire protection at the connection is at least as high as that of the adjacent members - should be accompanied by the prerequisite that the utilisation of the connection should not be larger than the utilisation of the connected members (as in EN 1993-1-2).

ACKNOWLEDGEMENTS

This research was carried out under project number MC1.02147 in the framework of the Strategic Research programme of the Netherlands Institute for Metals Research in the Netherlands (www.nimr.nl).

The members of the joint industry project group "fire design of aluminium structures", The Netherlands, are kindly acknowledged for their contribution.

REFERENCES

[1] Lundberg, S., “Mechanical Properties at Elevated Temperature for Aluminium Alloys CEN/TC 250/SC 9/PT Fire/N-27”, 2003.
[2] Kammer, C., “Aluminium Taschenbuch teil 1”, Grundlagen und Werkstoffe Aluminium Verlag, Düsseldorf, 2002.
[3] Maljaars, J., Soetens, F. and Twilt, L., “Heating of Aluminium Members Exposed to Natural Fire Conditions”, Proceedings of SIF’06, 2006, Vol. 1, pp. 75-88.
[4] EN 1999-1-2 Eurocode 9: Design of Aluminium Structures – Part 1-2: General Rules – Structural Fire Design, 2006.
[5] EN 1999-1-1 Eurocode 9: Design of Aluminium Structures – Part 1-1: General Structural Rules, 2007.
[6] Altenpohl, D., Aluminium Viewed from within, Aluminium-Verlag, Düsseldorf, 1982.
[7] Gitter, R., “Aluminium Materials for Structural Engineering – Essential Properties and Selection of Materials”, Structural Engineering International, 2006, Vol. 4/2006.
[8] Dwight, J., “Aluminium Design and Construction”, Spon, London, 1999.
[9] Soetens, F., “Welded Connections in Aluminium Alloy Structures”, Heron, Vol. 32, 1987.
[10] Voorhees, H.R. and Freeman, J.W., “Report on the Elevated-temperature Properties of Aluminium and Magnesioum Alloys”, Americal Society of Testing Materials, STP No. 291, 1960.
[11] Kaufman, J.G., “Properties of Aluminium Alloys – Tensile, Creep and Fatigue Data at High and Low Temperatures, ASM International, Materials Park, 1999.
[12] Hepples and Wale High Temperature Tensile Properties of 6082-T651, Technical Assistance Report No. BTAR-93/024, Alcan Banbury Laboratory, 1992.

[13] Langhelle, N.K., “Experimental Validation and Calibration of Nonlinear Finite Element Models for Use in Design of Aluminium Structures Exposed to Fire”, Norwegian University of Science and Technology : Trondheim, 1999, ISBN 82-471-0376-1.
[14] Kumar, D.R. and Swaminathan, K., “Tensile Deformation Behaviour of Two Aluminium Alloys at Elevated Temperatures”, Materials at High Temperatures, 1999, Vol. 16, pp. 161-172.
[15] Van den Boogaard Thermally Enhanced Forming of Aluminium Sheet, PhD dissertation, University of Twente, The Netherlands, 2002.
[16] Maljaars, J., Fellinger, J.E.J. and Soetens, F., “Fire Exposed Aluminium Structures”, Heron, 2005, Vol. 50-4, pp. 261-278.
[17] EN 1993-1-2 Eurocode 3: Design of Steel Structures – Part 1-2: General Rules – Structural Fire Design, 2005.
[18] Franssen, J.M. and Zaharia, “Steel Structures Subjected to Fire, 2nd Edition, University of Liege, Belgium, 2006.
[19] EN 10002-5 - Metals – Tensile Test - Part 5: Test Method at elevated temperature, 1992.

NUMERICAL ANALYSES OF COLD-FORMED THIN-WALLED SECTIONS WITH CONSIDERATION OF IMPERFECTIONS DUE TO THE PRODUCTION PROCESS

Albrecht Gehring [1] and Helmut Saal [2,*]

[1] *Research assistant, Versuchsanstalt für Stahl, Holz und Steine, Universität Karlsruhe (TH), Germany*
[2] *Professor, Versuchsanstalt für Stahl, Holz und Steine, Universität Karlsruhe (TH), Germany*
**(Corresponding author: E-mail: helmut.saal@va.uka.de)*

ABSTRACT: The load bearing capacity of cold-formed thin-walled sections strongly depends on deviations from the nominal dimensions and the material properties. The former reduce the load bearing capacity. The latter enhance the load bearing capacity, because of work hardening during the manufacturing process. It is difficult to realistically account for both effects in a finite-element analysis of the load bearing capacity of thin-walled sections. Today, cost intensive testing is necessary, if a maximum utilization of the load bearing capacity is desired. The properties of a product can be determined during the product development process with a new simulation strategy, which covers the production process as well as the state of serviceability of a product. The roll forming process is simulated first followed by a non-linear ultimate limit state analysis. The combination of both analysis steps gives the possibility to determine the load bearing capacity realistically as deviations from the nominal value of dimensions and material properties areincluded in the analysis. The new analysis strategy is demonstrated for a U-section with respect to different aspects concerning work hardening and the load bearing capacity of a C-section. It is shown, that the new strategy leads to a realistic estimation of the load bearing capacity of thin gauged sections.

Keywords: Numerical analyses, cold-formed sections, imperfections, work hardening, ultimate limit state

---

1. INTRODUCTION

Cold-formed thin-walled sections are produced by roll forming. Roll forming is a technology where a flat strip is formed into a cross-section continuously. The process involves a progressive bending of the metal strip as it passes through a series of forming tools, see Figure 1. The design of the rolling schedule is done by unfolding the profile. From this, the flower diagram is obtained, see Figure 1. Different calibration methods are used to obtain the flower diagram. Arc bending or the constant radius method are in common use, but other methods are also applied, Halmos [1], Bogojawlenski et al [2]. The sheet is deformed by an intended transversal bending load and unavoidable reversed bending and shear loads in longitudinal and transverse direction during roll forming. The latter arise from the curvature of a fiber during the forming process and they significantly influence the forming process and the final shape of the cross-section, Halmos [1], Bogojawlenski et al [2].

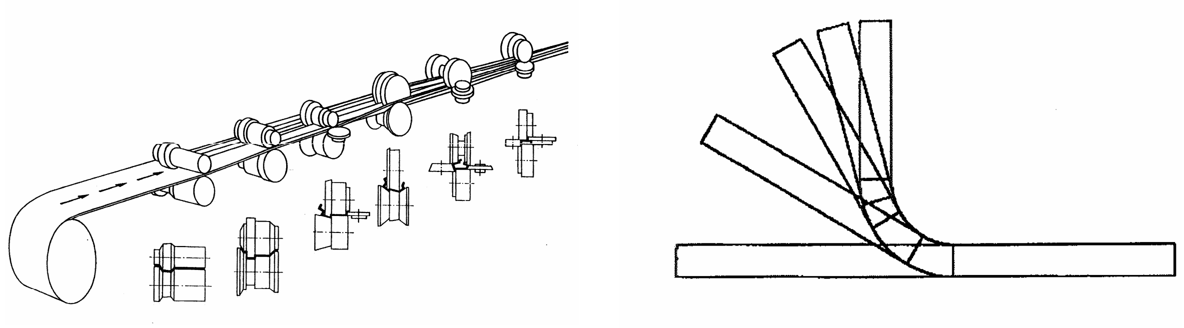

Figure 1. Roll Former (Left); Flower Diagram of a U-Profile (Right)

2. FINITE ELEMENT MODEL

2.1 General Considerations

The roll forming process can be regarded as a quasi-static dynamic process. Thus an explicit solver is applicable. The explicit solver is advantageous in an analysis, where contact is involved, Abaqus [3]. An implicit solver is used for subsequent springback analyses. The software package Abaqus [4] is used for all analyses jobs. The analyses are executed parallel with the domain-level method. The analyses jobs are run mainly on 4 cpus or 8 cpus on the HP XC 6000 cluster and on HP XC 4000 cluster of the Universität Karlsruhe [5].

2.2 Model Details

The forming tools are represented as rigid bodies in all analyses. The blank is meshed with the 4 node shell element S4R. In the flat areas an element size of 3 x 3 mm with 5 integration points through thickness are used and in the bending area an element size of 1 x 3 mm with 9 integration points through thickness are used. The ends of the sheet are constrained in rolling direction to simulate an endless sheet. Fixed boundary conditions are applied on the forming tools in all analysis jobs. The general contact algorithm is used in the analysis, as no restrictions are placed on the domain decomposition for domain-level parallelization. Friction is neglected with all analyses. The load is applied as velocity in rolling direction. The velocity is increased in the first 0.05 s from zero to a constant forming speed using the smooth step definition of ABAQUS [4] to minimize inertia effects in this quasi-static analysis. Through this, longitudinal oscillations of the sheet are minimized and thus the probability to induce numerically noisy or inaccurate results is reduced. The verification of the model is described in detail by Gehring and Saal [6].

2.3 Material Model

A Young's Modulus of E = 210 GPa and a Poisson's ratio of $\nu = 0.3$ define the elastic response in all analyses. The plastic part is described by the following material models, Khan and Huang [7]:

- Standard isotropic hardening with von Mises type yield function and associated plasticity
- Yield function according to the Hill stress potential and associated plasticity

In all models, the isotropic hardening behaviour of the material is modelled with the modified Ludwik-Hollomon equation, which is usually applied in forming analysis, Lange [8]. In this Equation

$$k_f(\varepsilon_p) = f_y \cdot \Phi \cdot \left(\frac{e}{n}\right)^n \cdot \varepsilon_p^n \tag{1}$$

f_y is the yield strength, Φ is the strength ratio of tensile strength to yield strength, ε_p are true plastic strains, e is the Euler number and n is a constant. Eq. 1 gives a good approximation of the flow curve for low alloy steel and aluminium alloys, if the exponent n is related to the uniform elongation ε_u in terms of $n = \ln(1 + \varepsilon_u)$, Lange [8]. The Hill stress potential is expressed as

$$f(\sigma) = \sqrt{F(\sigma_{22} - \sigma_{33})^2 + G(\sigma_{33} - \sigma_{11})^2 + H(\sigma_{11} - \sigma_{22})^2 + 2L\sigma_{23}^2 + 2M\sigma_{31}^2 + 2N\sigma_{12}^2} \tag{2}$$

where F, G, H, L, M and N are constants. These constants are defined as a function of the ratios R_{ij} of the reference stress σ_Y to measured yield stress value $\bar{\sigma}_{ij}$, when σ_{ij} is applied as the only nonzero stress component, Khan and Huang [7]. Here, the 1-axis constitutes the rolling direction and the 2-axis is transverse to the direction of rolling. The 3-axis is normal to the sheet plane. The reference yield stress σ_Y is determined in 1-direction and thus R_{11} becomes 1.00. Furthermore, the constants R_{33}, R_{13} and R_{23} are set to 1.00, because effects of a through-thickness anisotropy can be neglected in roll forming, Engl and Stich [9].

3. DESIGN CONSIDERATIONS

3.1 General

The application of cold-formed sections in buildings is well established. The resistance of thin-walled sections can be determined with calculations based on the effective width approach according to international design codes, e.g. EN 1993-1-3 [10]. The application of the design codes leads to conservative resistance values. The full benefit of the cross-sectional resistance can be achieved only by cost intensive experimental investigations, e.g. according to the guidelines given in EN 1993-1-3 [10].

3.2 Increased Yield Strength

The strain distribution after roll forming of an U-section can be seen in Figure 2. The strains in the corners are clearly higher than in the flat areas of the cross-section. This means, that work hardening takes place mainly in the corner areas. Many studies have been made to utilize the enhanced material properties for design. The mechanical properties were determined by tensile tests with specimen from different parts of a profile. Also full-section tensile or compressive tests were performed to obtain specific average yield strength for design application. A comprehensive list of references is contained in Halmos [1], Bogojawlenski et al [2] and Yu [11].

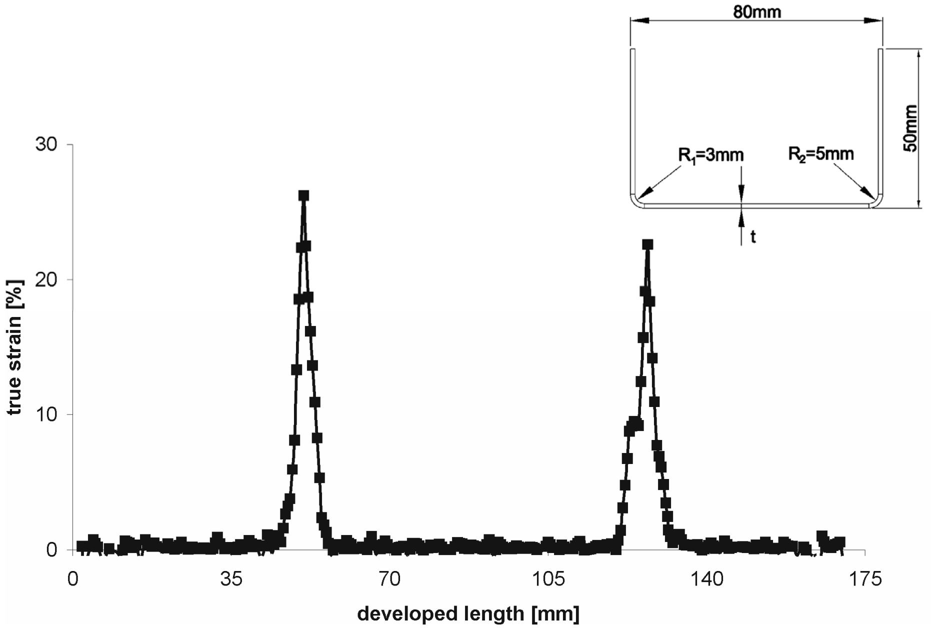

Figure 2. Strain Hardening Due to Roll Forming of a U-Section

Semi-empirical equations are introduced in international design standards for taking an enhanced yield strength into account. In EN 1993-1-3 [10], the increased yield strength f_{ya} is expressed as

$$f_{ya} = \min\left(0{,}5 \cdot \left(f_u + f_y\right);\, f_y + \left(f_u - f_y\right)\frac{k \cdot n \cdot t^2}{A_g}\right) \tag{3}$$

where f_y and f_u are the design values of the yield strength and the tensile strength respectively, k is a constant depending on the applied forming technology, e.g. k = 7 for roll forming, n is the number of 90° bends and A_g is the gross cross-sectional area. The increased yield strength f_{ya} is approximated in North America, Yu [11], with

$$f_{ya} = a_V \cdot f_{yc} + \left(1 - a_V\right) f_y \tag{4}$$

where f_{yc} is the corner yield strength and a_V is the ratio of corner areas to the gross cross-sectional area. The corner yield strength is calculated to

$$f_{yc} = f_y \cdot \frac{B_c}{\left(r/t\right)^m} \tag{5}$$

where

$$B_c = 3{,}69 \cdot \frac{f_u}{f_y} - 0{,}819 \cdot \left(\frac{f_u}{f_y}\right)^2 - 1{,}79$$

$$m = 0{,}192 \cdot \frac{f_u}{f_y} - 0{,}068$$

and r/t is the ratio of the bending radius to the thickness of the sheet. The application of Eq. 3 and Eq. 4 is restricted to a full effective cross-sections, certain values of the ratios r/t and f_u/f_y respectively and also to certain load cases.

3.3 Numerical Analysis

In EN 1993-1-5, Annex C [12] a guidance is given for the use of finite-element analysis for ultimate limit state verification, which includes appropriate assumptions for material models and imperfections. In the following, an analysis according to the guidance in EN 1993-1-5, Annex C [12] is called conventional analysis strategy. A non-linear finite-element analysis is necessary for the determination of the ultimate limit state of thin-walled sections. Where the non-linearity takes into account geometric deviations as well as material aspects. The imperfections can be introduced by applying equivalent geometric imperfections defined in design codes, which are scaled eigenmodes obtained from buckling analysis. Usually the material properties are assumed to be distributed uniformly, which leads to a safe estimation of the failure loads. General considerations on the characterisation of imperfections in numerical analyses are given by Schafer and Peköz [13]. Gardner and Nethercot [14] and Lecce and Rasmussen [15] introduce an enhanced yield strength due to cold-working by partitioning a cross-section. However, the problem is the lack of knowledge about the initial state of cold-formed sections, Schafer and Peköz [13].

3.4 New Analysis Approach

The properties of a roll formed section are determined with a new analysis strategy, which covers the production process as well as the state of serviceability of the section, Gehring et al [16]. The roll forming process is simulated first. This is followed by a non-linear ultimate limit state analysis. The combination of both analysis steps gives the possibility to determine the load bearing capacity realistically as deviations from the nominal value of dimensions and material properties are included in the analysis. The analysis is divided into the following steps:

- Analysis of the manufacturing process
- Introduction of imperfections and change of material properties obtained by the analysis of the manufacturing process as initial state to the new model
- Non-linear ultimate limit state analysis
- Verification of results

The new analysis strategy is demonstrated by two examples. Here, the yield strength is f_y=320MPa, the tensile strength is f_u=390 MPa and the uniform elongation is $\varepsilon_u = 0.12$. These values comply with steel grade S320 according to EN 10326 [17].

4. APPLICATION OF THE NEW APPROACH

4.1 Example 1: Degree of Work Hardening, Gehring and Saal [18]

Roll forming of an U 35 / 100 / 35 x 1 section is simulated. The applied inner bending radius is 4.00 mm. The profile is obtained on base of three different flower diagrams – 3 steps 30°/60°/90°, 4 steps 20°/45°/70°/90° and 5 steps 15°/35°/55°/75°/90°. The roll stands of the steps 15°, 20°, 30°, 35° and 45° are built with two tools. An additional side tool is applied in the roll stands of steps 55°, 60°, 70°, 75° and 90° respectively, see Figure 3. The inter-pass distance is set to 500 mm.

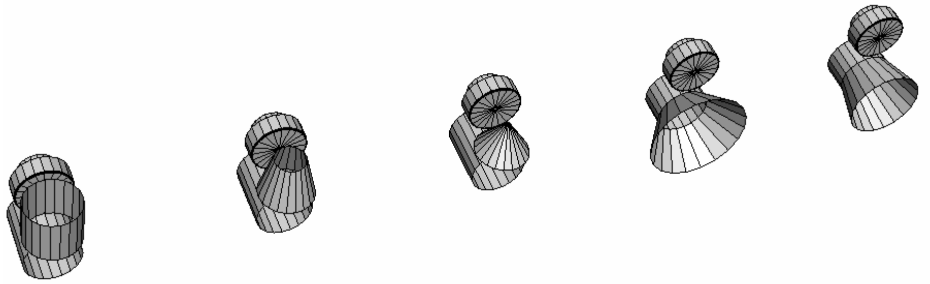

Figure 3. Roll Former with 5 Roll Stands – Steps From Right to Left: 15°/35°/55°/75°/90°

Experiments are performed to measure the effects of variables on a response. The effect of a variable means the change in the response as a variable is moved from a lower level to a higher level. Factorial designs are useful for this purpose, especially two-level factorial designs, Box et al [19]. Here, the objective is to identify the effect of mechanical material properties on the distribution of the yield stress of a roll formed section. Deviations from the assumed linear relation in two-level designs can be identified with an additional centre-point run. Then, the number m of experimental runs is

$$m = 2^k + 1 \tag{6}$$

where k is the number of variables. Here the commercial statistic software Statistica [20] is used for the design of the runs and the analysis of the results. The material properties strength ratio $\Phi = f_u/f_y$, uniform elongation ε_u and the constant R_{22} are taken as variables. The constant R_{12} is linked with R_{22} and thus not used as independent variable. On the upper level $R_{12} = 1.03$ and on the lower level $R_{12} = 1.00$. In addition the technological variable number of roll stands n_R is used. Thus, m = 17 experimental runs are necessary in this study. The experimental design can be seen in Table 1.

Plastic flow occurs in Hill's stress potential, if the equivalent yield stress according to Eq. 2 reaches the defined reference yield stress value. The size of the yield surface changes with the equivalent plastic strain ε_{eppq} isotropically. From this follows, that the yield stress $f_{y,fem}$ can be calculated with Eq. 7 and the average yield stress $f_{ya,fem}$ can be calculated with Eq. 8.

$$f_{y,fem}\left(\varepsilon_{eppq}\right) = \Phi \cdot f_y \cdot \left(\frac{e}{n}\right)^n \cdot \varepsilon_{eppq}^n \tag{7}$$

$$f_{ya,fem} = \frac{1}{l} \cdot \int_0^l f_{y,fem}\left(\varepsilon_{eppq}\right) dl \tag{8}$$

The effect of a variable on the increase of the yield strength is evaluated by statistical methods. The ratio $\psi = f_{ya,fem} / f_y$ is introduced for the evaluation. The effect C of a variable is calculated to

$$C = \frac{2}{m} \cdot \sum_{i=1}^{m} \left(\psi_i \cdot \{\pm\}\right) \tag{9}$$

where the subscript i refers to the run number and the sign in {} brackets to the low and high level respectively. The interaction effects are calculated similarly. Since there were no replicated runs, a standard error s_d^2 has to be estimated using higher-order interactions with negligible influence to

$$s_d^2 = \frac{1}{k} \cdot \sum_k C^2 \tag{10}$$

The significance of an effect can be identified by means of a confidence estimation based on the t distribution. Deviations from the assumed linear relations of the two-level design can be identified from the centre-point run with a curvature test. Detailed information on the statistical evaluation methods is given in Box et al [19].

The average yield stress $f_{ya,fem}$ and the maximum value of the yield stress $f_{y,fem}^{\#}$ evaluated with Eq. 7 and Eq. 8 are given in Table 1. In addition, the yield strength f_{ya} obtained from Eq. 3 and 4 are given in Table 1.

Eq. 3 leads to a safe estimation of the increased yield strength whereas Eq. 4 overestimates the increased yield strength for certain values of Φ slightly. The corner yield strength f_{yc} obtained from Eq. 5 overestimates the material response. This is evident by a comparison of f_{yc} and the individual true tensile strength $f_{u,true} = \Phi \cdot f_y \cdot (1 + \varepsilon_u)$, where f_{yc} is greater than $f_{u,true}$ for $\Phi = 1.2$ and 1.3. The distribution of the yield stress obtained from some runs with 3 roll stands are shown in Figure 4. The influence of a change of Φ and ε_u on the yield stress distribution is obvious from the web of the U-section. The steeper gradient of the flow curve with $\Phi = 1.3$ and $\varepsilon_u = 0.10$ causes more strain hardening than other combinations.

Table 1. Experimental Design and Results

Run	Variable [1]				Results						
no.	Φ	ε_u	R_{22}	n_R	$f_{y,fem}$ # [MPa]	$f_{ya,fem}$ [MPa]	ψ [-]	f_{ya} [2] [MPa]	f_{ya} [3] [MPa]	f_{yc} [4] [MPa]	$f_{u,true}$ [MPa]
1	$1.10^{\{-\}}$	$0.10^{\{-\}}$	$1.00^{\{-\}}$	$3^{\{-\}}$	389	330	1.031	323	327	403	387
2	$1.30^{\{+\}}$	$0.10^{\{-\}}$	$1.00^{\{-\}}$	$3^{\{-\}}$	459	364	1.138	328	336	510	458
3	$1.10^{\{-\}}$	$0.15^{\{+\}}$	$1.00^{\{-\}}$	$3^{\{-\}}$	386	327	1.023	323	327	403	405
4	$1.30^{\{+\}}$	$0.15^{\{+\}}$	$1.00^{\{-\}}$	$3^{\{-\}}$	455	347	1.085	328	336	510	478
5	$1.10^{\{-\}}$	$0.10^{\{-\}}$	$1.05^{\{+\}}$	$3^{\{-\}}$	390	330	1.032	323	327	403	387
6	$1.30^{\{+\}}$	$0.10^{\{-\}}$	$1.05^{\{+\}}$	$3^{\{-\}}$	460	365	1.140	328	336	510	458
7	$1.10^{\{-\}}$	$0.15^{\{+\}}$	$1.05^{\{+\}}$	$3^{\{-\}}$	388	328	1.024	323	327	403	405
8	$1.30^{\{+\}}$	$0.15^{\{+\}}$	$1.05^{\{+\}}$	$3^{\{-\}}$	462	351	1.098	328	336	510	478
9	$1.10^{\{-\}}$	$0.10^{\{-\}}$	$1.00^{\{-\}}$	$5^{\{+\}}$	386	326	1.020	323	327	403	387
10	$1.30^{\{+\}}$	$0.10^{\{-\}}$	$1.00^{\{-\}}$	$5^{\{+\}}$	459	349	1.092	328	336	510	458
11	$1.10^{\{-\}}$	$0.15^{\{+\}}$	$1.00^{\{-\}}$	$5^{\{+\}}$	381	325	1.016	323	327	403	405
12	$1.30^{\{+\}}$	$0.15^{\{+\}}$	$1.00^{\{-\}}$	$5^{\{+\}}$	451	335	1.047	328	336	510	478
13	$1.10^{\{-\}}$	$0.10^{\{-\}}$	$1.05^{\{+\}}$	$5^{\{+\}}$	390	326	1.020	323	327	403	387
14	$1.30^{\{+\}}$	$0.10^{\{-\}}$	$1.05^{\{+\}}$	$5^{\{+\}}$	457	349	1.090	328	336	510	458
15	$1.10^{\{-\}}$	$0.15^{\{+\}}$	$1.05^{\{+\}}$	$5^{\{+\}}$	382	325	1.017	323	327	403	405
16	$1.30^{\{+\}}$	$0.15^{\{+\}}$	$1.05^{\{+\}}$	$5^{\{+\}}$	453	335	1.048	328	336	510	478
17	1.20	0.125	1.00	4	420	333	1.040	325	332	460	432

[1] The + and – sign in {} brackets refer to the high and the low level respectively.

[2] According to Eq. 3

[3] According to Eq. 4

[4] According to Eq. 5

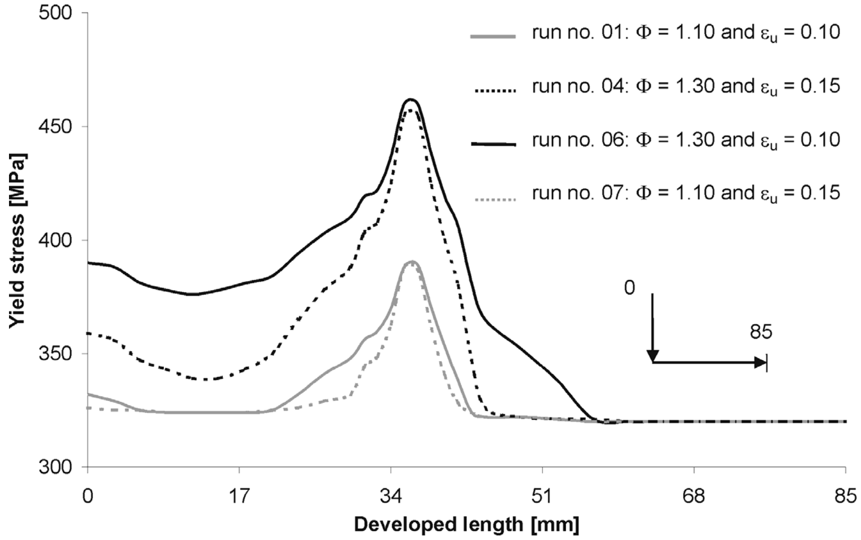

Figure 4. Distribution of Yield Strength – Runs 1, 4, 6 and 7

Table 2. Statistical Evaluation

Effect 1)	$C \cdot 10^2$ [-]
Φ (1)	**6.926**
ε_u (2)	**-2.582**
R_{22} (3)	0.217
n_R (4)	**-2.795**
12	**-1.986**
13	0.162
14	**-1.818**
23	0.180
24	0.211
34	-0.203
123	0.177
124	-0.018
134	-.0188
234	-0.109
1234	-0.139

1) Interactions are denoted with digits, e.g. the 2nd-order interaction of Φ and ε_u is denoted with 12.

The calculated effects and interactions C are given in Table 2. The comparison of the values suggests that the values in bold figures require further interpretation. All other values are supposed to be negligible and thus are used for the estimation of the standard error s_d^2, which becomes to $s_d^2 = 0.025$. From this follows the absolute value $c_{t,p}$ of a confidence interval. The values of $c_{t,p}$ on confidence levels of 95 %, 99 % and 99.9% are $c_{t,95\%} = 0.356$, $c_{t,99\%} = 0.507$ and $c_{t,99.9\%} = 0.732$ respectively.

Herewith the assumption is confirmed that the bold values are significant. The curvature test reveals, that the value of ψ does not depend linear on the variables. Thus, it is necessary to apply a higher-order statistical model for further investigations.

It is obvious that the value of the strength ratio Φ has a major effect on the increase of the yield strength.

Raising Φ from 1.1 to 1.3 leads to an increase of the average yield strength of 6.9 % in this example. The effect of ε_u is opposite to that of Φ, i.e. a smaller value of the uniform elongation ε_u results in a higher average yield strength. The increase of the yield strength decreases with increase of the number n_R of roll stands. This is due to smaller incremental bending in longitudinal direction. However, the significance of the interactions 12 and 14 shows, that the effect of the strength ratio Φ must also be considered jointly with the uniform elongation and the number of roll stands. The interaction of Φ and ε_u needs no further explanation as it was already discussed above. It is expected, that the interaction of Φ and n_R becomes less important with an increasing number of roll stands. But this has to be confirmed. It is worth to point out, that the influence of the anisotropy can be neglected.

4.2 Example 2: Load Bearing Capacity of a C-section, Gehring et al [16]

The roll forming process of a C-section 10 / 35 / 100 / 35 / 10 x 1 is simulated in the first analysis step. The applied inner bending radius is 4 mm. The C-section is obtained in 9 steps. First the edge stiffener of the C-section is formed with 4 roll stands in steps 20°/40°/60°/90°. Then the web is folded with 5 roll stands in steps 15°/35°/55°/75°/90°. All roll stands for the stiffener and the roll stands of the steps 15° and 35° are built with two tools. An additional side tool is applied in the roll stands of steps 55°, 75° and 90° respectively. The inter-pass distance is set to 500 mm.

The second step of the analysis is to transfer the results of the preceding analysis as initial state into the new model. In this step the out-of-balance forces of the explicit analysis are removed and static equilibrium is achieved. This accounts for springback effects. Thus dimensional deviations and cold-working effects due to roll forming are considered in the initial state. The failure load is calculated in the last step of the analysis. For this, the profile is divided into 6 specimen with a length of 250 mm each. This value is less than 20 times the radius of gyration and thus agrees with the length of stub column specimen recommended in EN 1993-1-3 [10]. The virtual stub column tests are performed with the 4 specimen from the middle part of the profile. New boundary conditions are applied to the model. At one end of the sections all translation degrees of freedom are fixed and at the other end the out-of plane degrees of freedom are fixed. The sections are subjected to constant translation in longitudinal direction.

For comparison, the ultimate limit state of the C-section is determined with the conventional analysis strategy. The eigenmode which corresponds to the lowest eigenvalue is used as imperfection. The amplitude of the eigenmode is scaled to a value of b/200 which complies with the value recommended in EN 1993-1-5 [12], Annex C. The material properties are assumed to be constant across the cross-section. The boundary conditions are defined as in the last step of the advanced analysis.

Also, the effective cross-sectional area A_{eff} of the C-section is calculated in accordance with provisions given in EN 1993-1-3 [10]. The characteristic resistance $N_{c,EC3}$ of the cross-section for uniform compression according to EN 1993-1-3 [10] is

$$N_{c,EC3} = A_{eff} \cdot f_y \tag{11}$$

The failure load N_u obtained from the finite-element analysis is calculated to

$$N_u = \sum_{i=1}^{k} n_{1,i} \tag{12}$$

where $n_{1,i}$ is the reaction force of the i-th node in loading direction and k is the number of nodes across the section.

The variation of material properties and geometric imperfections due to the forming process is taken into account in the determination of the load bearing capacity of the 4 individual specimen. The deformed shape obtained from the new analysis exhibits typical geometric defects of roll formed sections, like the flare at the ends of the profile, see Figure 5. The geometric imperfections obtained from this analysis are shown in Figure 5, where the values are taken from a path along the arrows in Figure 5 respectively.

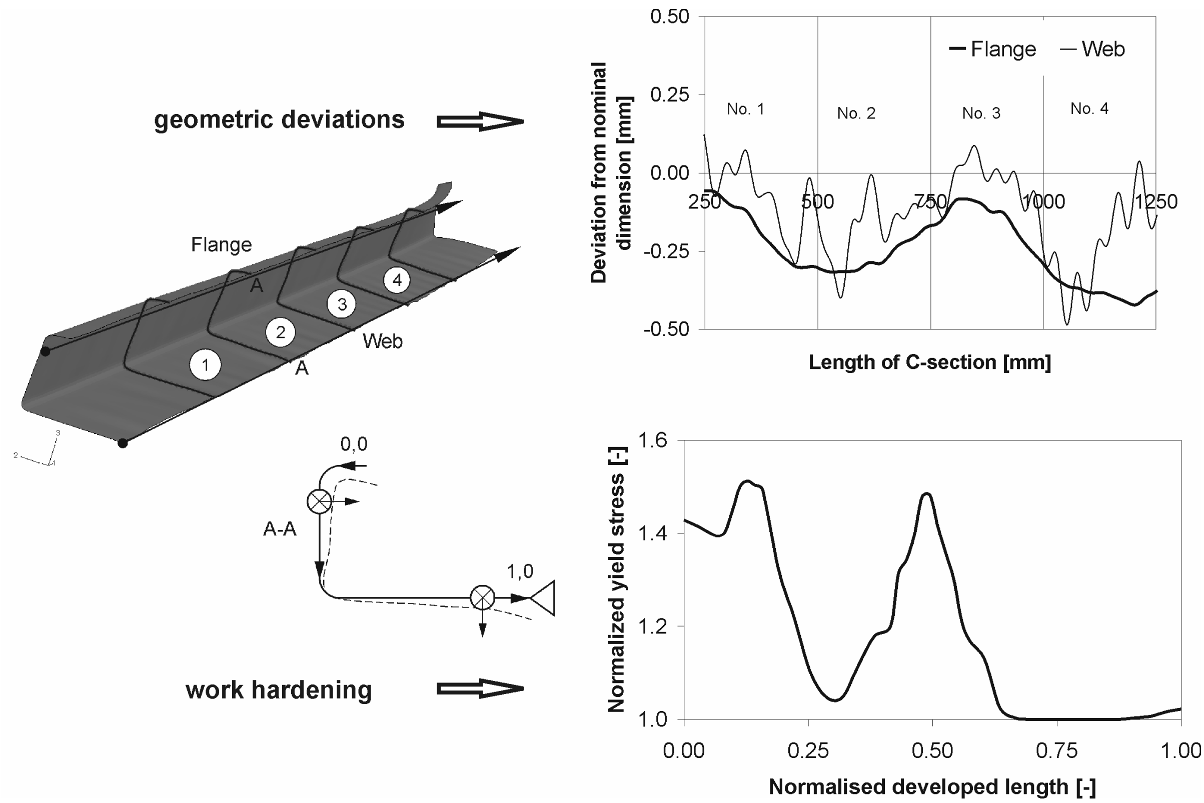

Figure 5. Predicted Imperfections from Simulation of Roll Forming Process

The numbers in Figure 5 are referring to the specimen number for the virtual stub column tests. The maximum value of the geometric imperfection of the flange is approximately 0.4 mm and of the web approximately 0.5 mm. These values agree quantitatively with measured values of similar sections, Lecce and Rasmussen [15] [16]. Also residual stresses and work hardening effects due to roll forming are considered in the initial state. The distribution of the yield stress after roll forming is shown in Figure 5. In addition, the average yield strength f_{ya} is determined according to Eq. 7 and Eq. 8.

The deformed C-sections after failure are shown in Figure 6. The failure modes deviate from each other, because the applied imperfections are different. In the conventional analysis, the wave length of the edge stiffener is longer than in the advanced analysis.

It is obvious from Figure 6, that the new analysis includes different imperfection modes and thus reveals different failure loads for each virtual test.

The failure loads determined with finite-element analyses are given in Table 3. The subscripts con and new refer to the conventional and new analysis respectively. The characteristic resistance according to EN 1993-1-3 [10] is $N_{c,EC3}$.

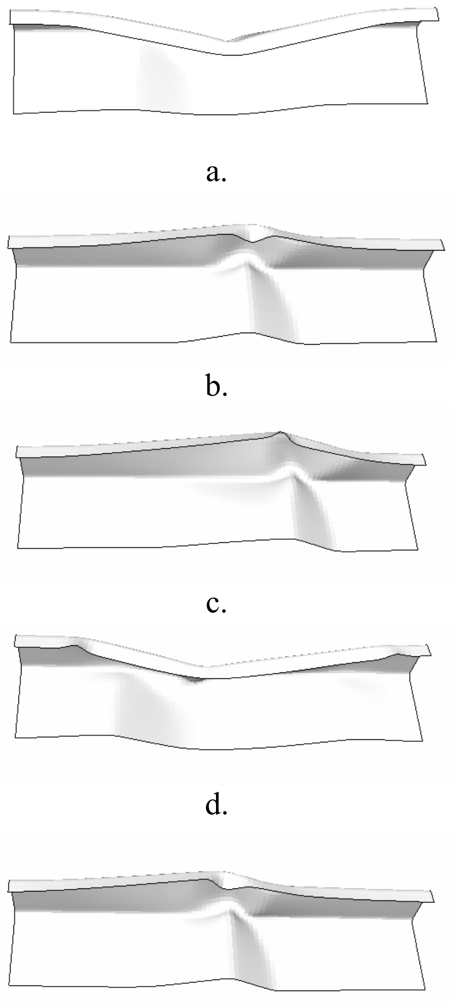

a.

b.

c.

d.

e.

Figure 6. Failed Specimen from Conventional Analysis (a.) and New Analysis (b. to e.)

Table 3. Ultimate Loads

$N_{c,EC3}$	[kN]	37,0
$N_{u,con}$	[kN]	39,8
$N_{u,new,1}$	[kN]	41,4
$N_{u,new,2}$	[kN]	42,4
$N_{u,new,3}$	[kN]	43,7
$N_{u,new,4}$	[kN]	42,4

The higher failure loads are due to the increased yield strength and the smaller geometric imperfections with the new analysis strategy. The average yield strength f_{ya} is 18 % higher than the yield strength f_y of the virgin material. The highest failure loads are obtained from the new analysis strategy. These are approximately 4 % to 10 % higher than the failure load obtained from the conventional analysis strategy and approximately 11 % to 18 % higher than characteristic resistance $N_{c,EC3}$ according to EN 1993-1-3 [10].

This example shows, that the new analysis strategy gives the opportunity to simulate the structural performance of cold-formed sections realistically. This is due to the fact, that deviations from the nominal dimensions and material properties are taken into account. The results are reasonable and within the expected range. With this model, the effect of slight modifications of, e.g. material specification, tool design, on the failure load, can be determined easily. However, in any case the results have to be verified with some tests before introducing them as characteristic resistance values in design.

5. SUMMARY AND CONCLUSIONS

A new simulation strategy for cold-formed thin-walled components, which covers the production process as well as the state of serviceability of a roll formed section was presented. The roll forming process is simulated first. This is followed by a non-linear ultimate limit state analysis. The combination of both analysis steps gives the possibility to determine the load bearing capacity realistically as deviations from the nominal value of dimensions and material properties are included in the analysis. The new analysis strategy is demonstrated for a U-section with respect to different aspects concerning work hardening and the load bearing capacity of a C-section. From the examples, the following conclusions can be drawn:

- The formulas for the average yield strength f_{ya} given in Eurocode 3 lead to a safe estimation of the increase of the yield stress due to roll forming.
- The strength ratio $\Phi = f_u / f_y$ is identified as the material property with the strongest influence. However, the effect of Φ interacts with the value of the uniform elongation ε_u.
- The anisotropy of the sheet material can be neglected.
- An increasing number of roll stands reduces the increase of the average yield stress.
- The enhanced average yield strength can be determined as a function of the material properties and the parameters of the roll former. This gives the opportunity to utilize the enhanced yield stress for specific sections in design.
- Deviation from the nominal dimensions and material properties are estimated realistically with the new analysis strategy and the obtained failure loads are reasonable compared to the values according to design standards.
- The characteristic resistance obtained from this process oriented analysis is higher than the characteristic values for general use in design standards.
- The new analysis strategy gives the chance to optimize the dimensions, the material specification and the manufacturing process of a section without a cost intensive experimental trial and error procedure.

It has to be kept in mind that the new analysis strategy will only lead to safe results if its application is based on a profound knowledge of the manufacturing process and the structural behaviour of the component. This demands substantial experience with experimental and numerical analysis of the object.

REFERENCES

[1] Halmos, G.T. (Edit.), “Roll Forming Handbook”, CRC Press Taylor & Francis Group, Boca Raton, 2006

[2] Bogojawlenskij, K.N., Neubauer, A. and Ris, V.W., “Technologie der Fertigung von Leichtbauprofilen“, VEB Deutscher Verlag für Grundstoffindustrie, Leipzig, 1979.

[3] ABAQUS Documentation – Version 6.6.1, Copyright 2006, ABAQUS, Inc.

[4] ABAQUS (Explicit & Standard); Version 6.6.1, Copyright 2006, ABAQUS, Inc.

[5] http://www.rz.uni-karlsruhe.de/ssc/hpxc

[6] Gehring, A. and Saal, H., “Sensitivity Analysis of Technological and Material Parameters in Roll Forming”, Proceedings of the 9th International Conference on Numerical Methods in Industrial Forming Processes, Porto, 2007, pp. 781.

[7] Khan, A.S. and Huang, S., “Continuum Theory of Plasticity”, John Wiley & Sons, Inc., New York, 1995.

[8] Lange, K. (Edit.), “Umformtechnik – Handbuch für Industrie und Wissenschaft, Band 1: Grundlagen“, Berlin: Springer Verlag, 1984.

[9] Engl, B. and Stich, G., “Neue Stahlsorten für die Kaltformung“, Tagungsband 722, Studiengesellschaft für Stahlanwendung e.V., 1998.

[10] EN 1993-1-3:2006, Eurocode 3 - Design of Steel Structures - Part 1-3: General Rules - Supplementary Rules for Cold-formed Members and Sheeting.

[11] Yu, W.-W., “Cold-formed Steel Design”, 3rd Edition, John Wiley & Sons, New York, 2001.

[12] EN 1993-1-5:2006, Eurocode 3 - Design of Steel Structures - Part 1-5: General Rules - Supplementary Rules for Cold-formed Members and Sheeting, Annex C.

[13] Schafer, B.W. and Peköz, T., “Computational Modeling of Cold-formed Steel: Characterizing Geometric Imperfections and Residual Stresses”, Journal of Constructional Steel Research, 1998, Vol. 47, pp. 193 – 210.

[14] Garnder, L. and Nethercot, D.A., “Numerical Modeling of Stainless Steel Structural Components – A Consistent Approach”, Journal of Structural Engineering, 2004, Vol. 130, pp. 1586 – 1601.

[15] Lecce, M. and Rasmussen, K., “Distortional Buckling of Cold-formed Stainless Steel Sections: Experimental Investigation”, Journal of Structural Engineering, 2006, Vol. 132, pp. 497 – 504.

[16] Gehring, A., Kathage, K. and Saal, H., “A New Strategy for Finite-element Analysis of the Load Bearing Capacity of Cold-formed Sections”, Proceedings of the 3rd International Conference on Structural Engineering, Mechanics and Computation, Capetown, 2007, pp. 377.

[17] EN 10326:2004, Continuously Hot-dip Coated Strip and Sheet of Structural Steels - Technical Delivery Conditions.

[18] Gehring, A. and Saal, H., “Yield Strength Distribution in Thin-walled Sections Due to Roll Forming – A Finite-Element Analysis”, Proceedings of the 6th International Conference on Steel and Aluminium Structures, Oxford, 2007, pp. 864.

[19] Box, G.E.P., Hunter, W.G. and Hunter, J.S., “Statistics for Experimenters”, 2nd Edition, New York: John Wiley & Sons, 2005.

[20] Statistica 7.1, Copyright 1986 - 2005, StatSoft, Inc.

Advanced Steel Construction Vol. 5, No. 2, pp. 164-174 (2009)

DESIGN OF WIDE-FLANGE STAINLESS STEEL SECTIONS

M. Lecce[1] and K.J.R. Rasmussen[2]

[1]Post Doctoral Fellow, Department of Civil Engineering, University of Toronto,
Toronto, Ontario, Canada, M5S 1A4
Tel: +1-416-978-3097, Fax: +1=416-978-6813, E-mail: mlecce@ecf.utoronto.ca
[2]Professor, School of Civil Engineering, University of Sydney,
Sydney, New South Wales, NSW 2006, Australia
Tel: +61 2 9351 2125, Fax: +61 2 9351 3343, E-mail: k.rasmussen@civil.usyd.edu.au

---

ABSTRACT: This paper describes a design procedure proposed to determine the moment capacities for the distortional and local buckling of wide-flange stainless steel sections influenced by flange curling. Experimental tests and theoretical analysis, conducted by the authors, of commercially available wide-flange stainless steel sections in pure bending have shown that flange-curling, where the wide-flange cross-section moves towards the neutral axis, reduces the cross-sectional section modulus, produces nonlinear stress distributions and increases the critical elastic buckling stresses. For the sections investigated, the section modulus is reduced by approximately 6% to 16.9%, while the critical elastic buckling stress is increased by a factor of 1.10 to 3.41. Overall, it was found that flange curling produced a net increase of up to 10.6% for the distortional buckling moment capacity but a net decrease of up to 12.2% for the local buckling moment capacity. Based on this data, it is recommended that the effects of flange curling should be ignored for distortional buckling but that it would be necessary to consider them for local buckling. This paper investigates whether the recently proposed Direct Strength Method (DSM) for the distortional buckling of stainless steel sections developed by Lecce and Rasmussen [1], the Winter curve for local buckling, and the North American Specification for the Design of Cold-Formed Steel Structural Members [2] DSM formulations for cold-formed carbon steel are applicable to wide-flange stainless steel sections in bending. It is concluded that the recently proposed DSM for stainless steel sections in compression can also be used, as presented herein, for wide-flange stainless steel sections in bending.

Keywords: Stainless steel, direct strength method, pure bending, local buckling, distortional buckling, flange curling, section modulus

---

1. INTRODUCTION

A recent experimental investigation [3] was conducted on the distortional and local buckling of two commercially available wide-flange ferritic stainless steel sections named Monoclad and Megaclad. The wide-flange width-to-thickness ratios of the two sections are 217 and 328, respectively. The wide-flange roof sections were subject to pure bending and were oriented in the test rig so that the wide flange was either in compression or tension. Figure 1 shows the top view of an experimental test of the Megaclad section where the wide flange is in compression.

Figure 1. Megaclad Experimental Test

A total of nine tests were conducted and all specimens showed evidence of flange curling. Flange curling is the tendency of the wide-flange of a thin walled section to shift towards the neutral axis when subject to bending and can occur when the wide-flange is in either tension or compression. As the wide flange moves towards the neutral axis, the cross-sectional geometry changes, the stress distribution becomes nonlinear, and the critical elastic buckling stress becomes altered. To gain a better understanding of this phenomenon and to quantitatively assess the deformations and associated flange stresses, Lecce and Rasmussen [4, 5] developed a nonlinear flange curling model to theoretically capture the changing geometric and loading conditions. The theoretical analysis of the wide-flange section stresses show that the stresses vary nonlinearly from the centre-pan to the web-flange junction, and that the nonlinearity becomes more severe for more slender sections. A full detailed report can be found in [4, 5].

The lack of available literature on the effects of flange curling and, in particular, their influence on the distortional and local buckling failure modes was the motivation behind this research. Furthermore, any limited literature that is available is based on tests of cold-formed *carbon* steel sections. The most relevant research was initiated by Winter [6] who proposed an equation to evaluate the flange curling deformations:

$$u_m = 2\frac{b_s^4}{t^2}\left(\frac{M}{EI}\right)^2 y \tag{1}$$

$$M = \frac{I\sigma_a}{y} \tag{2}$$

$$q = \left(\frac{M}{I}\right)^2 \frac{yt}{E} \tag{3}$$

where u_m is the deformation, M is the applied moment, y is the distance from the wide-flange to the neutral axis, I is the moment of inertia, q is a constant, uniform applied load causing flange curling, b_s is half of the wide-flange width (or full width of the wide-flange if the section is cantilevered), t is the section thickness, σ_a is the average stress in the flange determined by engineering beam theory, and E is the material modulus of elasticity. The constant "2" in Eq. 1 is an "average" of the theoretical values of 1.37 and 2.28 which correspond to idealized models where the flange curling deflections resemble that of a cantilevered, fixed-end beam (e.g., flange of an I-beam) and a simply supported beam (e.g., wide-flange simply supported by webs), respectively. The symbols M, σ_a and q in relation to a wide-flange section are depicted in Figure 2, (note the subscript "a" on σ_a has been dropped). In Figure 2 the symbol r_x is the radius of curvature of the bent plate (see Section A-A in Figure 2).

Bernard et al. [7, 8] examined the phenomenon of flange curling of thin walled roof sections and developed equations for maximum deflection taking into account different wide-flange end conditions provided by the section webs. Bernard et al. [7, 8] found that the best estimate of flange curling deformations (when compared to experimental results) was obtained when the true boundary conditions were represented, which are specific to the cross-section and connection details of the roof sections tested.

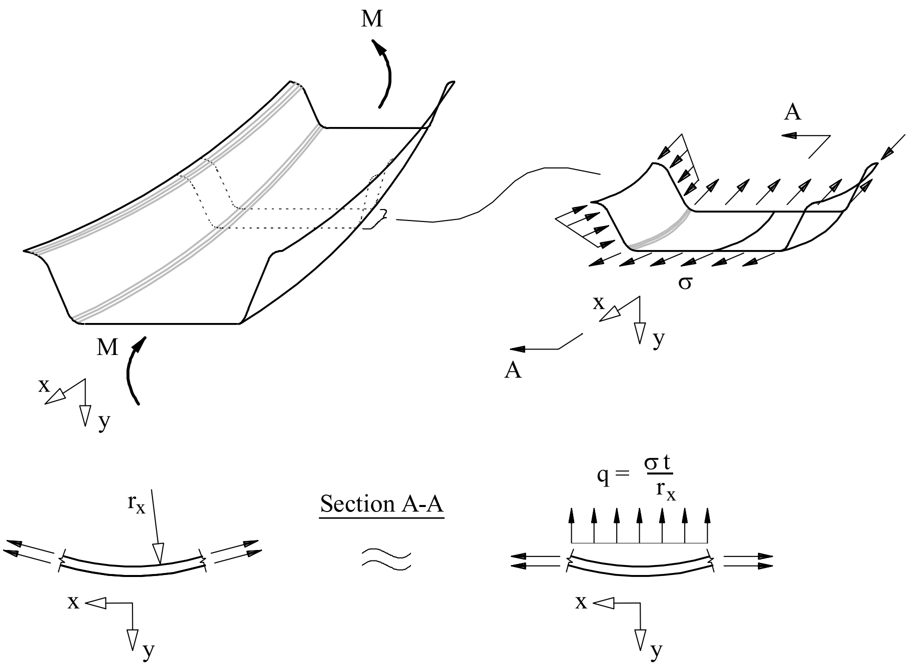

Figure 2. Flange Curling Stress Due to Applied Moment on a Wide-Flange Section

Nevertheless, the equations developed by Winter [6] and Bernard et al. [7] were developed based on the assumption that flange curling deformations were sufficiently small so that the stress (σ_a) causing flange curling remains uniform and that the cross-section properties including the first and second moment of area remains constant. With respect to the design of wide-flange sections, Bernard et al. [8] evaluated various design models for the distortional and/or local buckling modes and considered the interaction of local and distortional buckling but excluded the effects of flange curling.

The most recent research on wide-flange sections relevant to the research presented herein is that conducted by Davies and Chiu [9] who investigated both experimentally and numerically the behaviour of wide-flange, double-lip C-sections loaded in pure bending. The sections were used for double-skin "cassette" construction, and both foam-filled and non-filled sections were investigated. Davies and Chiu [9] suggest that if the wide flange is in tension, flange curling is not significant and if it is in compression, stresses which cause flange curling are "largely dissipated" once local buckling occurs. They also suggest that, for partially stiffened flange elements, the amount of flange curling can become significant but the magnitude can be estimated by considering the in-plane effective stress distribution.

Current guidelines in the Australian Standard/New Zealand Standard (AS/NZS) 4673 [10] for cold-formed stainless steel sections and the Direct Strength Method available in Appendix 1 of the North American Specification for the Design of Cold-Formed Steel Structural Members [2] (henceforth referred to as the NAS Appendix 1) for cold-formed carbon steel do not consider flange curling in the determination of ultimate moment capacity. The results of the experimental and theoretical investigations [3, 5, 11] are used in this paper for the assessment of design equations for moment capacity of wide-flange stainless steel sections. The current Direct Strength Method (DSM) formulations presented in the current NAS Appendix 1 [2], the DSM proposed for distortional buckling of stainless steel sections [1] and the Winter curve for local buckling are considered in the assessment.

2. FLANGE CURLING AND CRITICAL ELASTIC BUCKLING STRESS

The Direct Strength Method uses the critical elastic buckling stress (distortional buckling or local buckling), determined by rational analysis, and gross cross-sectional properties to evaluate the design strength. The ThinWall [12] finite strip elastic buckling analysis program was used to determine the gross cross-section properties and the critical elastic buckling stresses of the two wide-flanged sections, Monoclad and Megaclad, used in this study. Two sets of analyses were considered: one where the cross-section geometry was unaltered (or unaffected by flange curling); another where the theoretical flange curling displacements of the wide-flange were included in the cross-section geometry. The theoretical flange curling deformations, u_m, determined from a nonlinear flange curling model, are those which correspond to the mid-pan deformation at the experimental ultimate moment [5]. Therefore, the two sets of analyses provided critical elastic buckling stresses for the original cross-section and for a modified cross-section. The ThinWall program was used to calculate the section properties including the distance to the neutral axis, y, the second moment of area, I, gross section modulus, Z, section modulus to the extreme compression fibre, Z_f, and critical distortional or local elastic buckling stress, $f_{cr,d}$ and $f_{cr,l}$ respectively. These values are provided in Table 1, where those based on a modified cross-section are given the subscript "*m*".

Table 1. Original and Modified Geometric Properties and Critical Buckling Stresses

			Original Properties and Stresses (ThinWall)					Max. Disp. (Maple)	Modified Properties and Stresses (ThinWall)					Comparison	
Section	Orientation	$M_{u,avg}$ Nm	y mm	I mm^4	Z mm^3	Z_f mm^3	$f_{cr,d}$ or $f_{cr,l}$ MPa	u_m mm	y_m mm	I_m mm^4	Z_m mm^3	Z_{fm} mm^3	$f_{cr,dm}$ or $f_{cr,lm}$ MPa	Z_m/Z	$f_{cr,m}/f_{cr}$
Mono	WFC	860	8.07	56980	2859	7062	275	1.70	8.61	52920	2729	6144	422	0.955	1.534
Mono	WFT	1150	8.07	56980	2859	2859	1371	3.11	9.06	49840	2632	2632	1509	0.921	1.101
Mega	WFC	694	6.47	43800	2243	6768	104	6.91	8.98	31830	1871	3543	355	0.834	3.413
Mega	WFT	740	6.47	43800	2243	2243	671	7.40	9.21	31210	1858	1858	824	0.828	1.228

The stress distributions obtained from the critical elastic buckling analysis are depicted in Figures 3a and 3b for the Monoclad and Megaclad sections, respectively. Clearly those distributions for the modified cross-sections decrease toward the centre of the flange and this decrease is greater for the more slender Megaclad section. Figures 4 and 5 show the critical buckling stress versus half-wavelength for the original (solid line) and modified cross-sections (dotted line) for the distortional (wide flange in compression, WFC) and local (wide flange in tension, WFT) buckling modes of Monoclad sections and Megaclad sections, respectively. The minimum buckling stresses are highlighted by a diamond-shape data point.

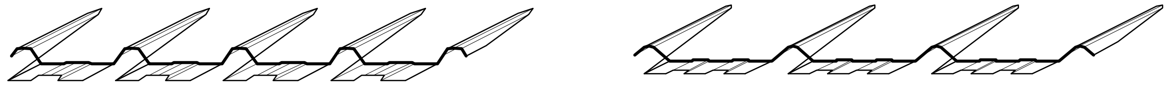

Original cross-section Original cross-section

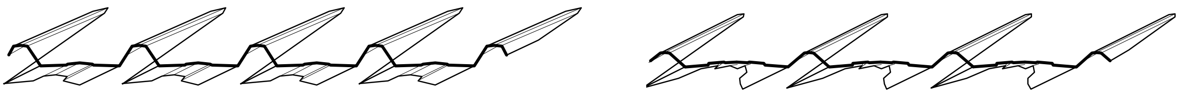

Modified cross-section Modified cross-section

(a) Monoclad sections (b) Megaclad sections

Figure 3. Stress Distributions

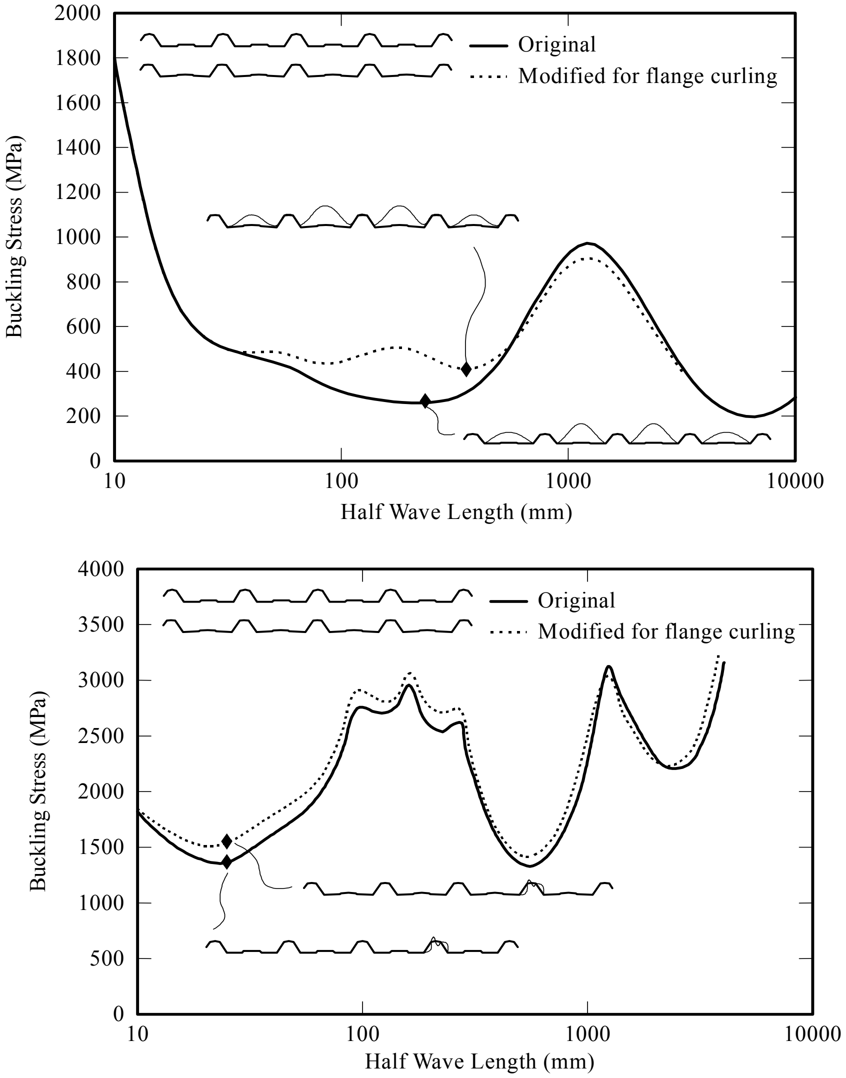

Figure 4. Elastic Buckling Analysis: Monoclad WFC (top); WFT (bottom)

When the wide flange is in compression, distortional buckling is the critical mode whereas when the wide flange is in tension, local buckling of the web/short flange is the critical buckling mode, and this is true irrespective of the influence of flange curling. As shown in Table 1, the modified cross-sections result in an increase in critical buckling stress. The ratio of the critical buckling stress of the modified section to that of the unaltered section ($f_{cr,m}/f_{cr}$) ranges from 1.10 to 3.41. In the case of distortional buckling, the half-wavelengths associated with the critical stress are also increased. These effects are the result of the cylindrical shape of the wide-flange produced by flange curling which stiffens the cross-section against local and distortional modes of buckling.

If one examines the results of Table 1, it is clear that the increase in critical buckling stress is greater for the distortional buckling critical sections (WFC) than it is for the local buckling critical sections (WFT) and, although flange curling causes a decrease in the section modulus, the decrease (see the ratio of Z_m/Z in Table 1) is greater for the local buckling critical sections.

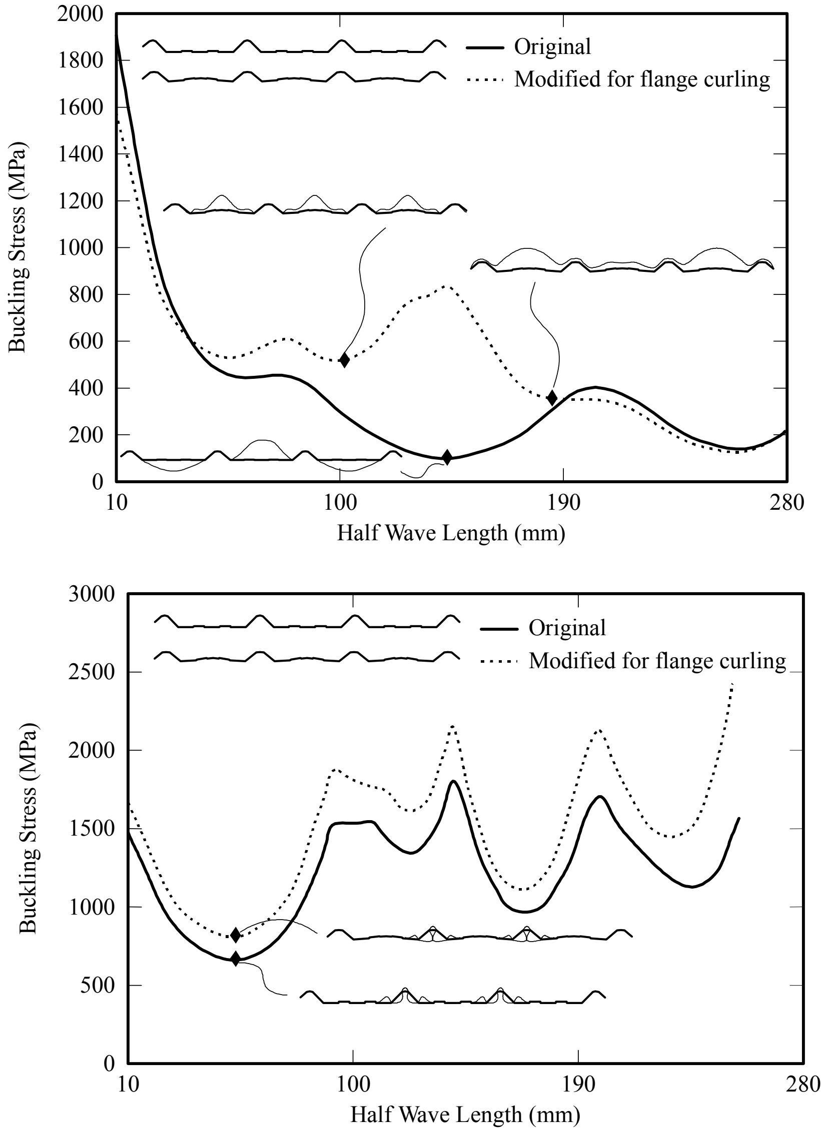

Figure 5. Elastic Buckling Analysis: Megaclad WFC(top) ; WFT (bottom)

Furthermore, flange curling deformations have a much greater influence on the more slender Megaclad section. The distortional and local critical buckling stresses for the Megaclad section is increased by a factor of 3.41 and 1.23 respectively whereas for the Monoclad section, the stresses are increased by a factor of 1.53 and 1.10 respectively. Although flange curling increases the critical buckling stress, the section modulus is reduced and this compromises the moment capacity. The section modulus is reduced by an average of 6% for the Monoclad section and 16.9% for the Megaclad section, again showing that flange curling has a greater influence on the more slender section. In any case, when considering the moment capacity, the net effect of increased critical buckling stress and decreased section modulus needs to be considered.

3. DIRECT STRENGTH METHOD TO DETERMINE MOMENT CAPACITY

The direct strength method provided in Appendix 1 of the North American Specification for the Design of Cold-Formed Steel Structural Members [2] for cold-formed carbon steel is considered for the design of stainless steel roof sections. Furthermore, the well-known Winter curve for local buckling and the proposed distortional buckling strength curve for stainless steel sections in compression [1] are also considered in the design evaluations. Note that research [13] has shown that the Winter curve provides accurate design strength predictions for the local buckling mode for stainless steel sections. The equations used in the DSM evaluations to determine moment capacity are as follows:

$$\lambda_d = \sqrt{\frac{M_y}{M_{cr,d}}} \tag{4}$$

$$M_{cr,d} = f_{cr,d} Z_f \tag{5}$$

$$\lambda_l = \sqrt{\frac{M_y}{M_{cr,l}}} \tag{6}$$

$$M_{cr,l} = f_{cr,l} Z_f \tag{7}$$

$$M_y = f_y Z \tag{8}$$

where, λ is slenderness, M_{cr} is the critical buckling moment, M_y is the yield moment, Z is the section modulus and Z_f is the section modulus calculated at the extreme compression fibre. The subscript "*d*" refers to distortional buckling and "*l*" to local buckling. (M_y and f_y are design yield moment and design yield stress, respectively, but are replaced by $M_{0.2}$ and $\sigma_{0.2}$, where $\sigma_{0.2}$ is the equivalent yield stress used in the design of stainless steels and other metals exhibiting gradual yielding). The design strength curves used in the evaluations are as follows:

Distortional Buckling, NAS Appendix 1 [2]:

$$M_{n,d} = M_y \left[\frac{1}{\lambda_d} - \frac{0.22}{\lambda_d^{\ 2}} \right] \le M_y \tag{9}$$

Distortional Buckling, based on Lecce and Rasmussen [1] for ferritic stainless steel:

$$M_{n,d} = M_y \left[\frac{0.90}{\lambda_d^{\ 1.1}} - \frac{0.20}{\lambda_d^{\ 2.2}} \right] \le M_y \tag{10}$$

Local Buckling, NAS Appendix 1 [2]:

$$M_{n,l} = M_y \left[\frac{1}{\lambda_l^{\ 0.8}} - \frac{0.15}{\lambda_l^{\ 1.6}} \right] \le M_y \tag{11}$$

Local Buckling, Winter curve:

$$M_{n,l} = M_y \left[\frac{1}{\lambda_l} - \frac{0.22}{\lambda_l^{\ 2}} \right] \le M_y \tag{12}$$

In Eqs. 9-12, M_n is the design moment capacity and the subscripts "*d*" and "*l*" represent distortional and local buckling, respectively.

The DSM evaluations using the distortional buckling strength curves given by the NAS Appendix 1 [2] for carbon steel (Eq. 9) and Lecce and Rasmussen [1] for stainless steel (Eq. 10) are presented in Tables 2 and 3. The evaluations given in Table 2 are based on original cross-sectional properties and associated critical buckling stresses whereas those given in Table 3 account for flange curling and are based on modified geometric properties and associated critical buckling stresses.

Table 2. Distortional Buckling Strength Evaluations Based on Original Properties

	Test	Values used in Distortional Buckling Strength Calculations							NAS Appendix 1, Eq. (9)		Lecce and Rasmussen, Eq. (10)	
Test ID	**M_u** **Nm**	Z mm^3	$\sigma_{0.2}$ MPa	$M_{0.2}$ Nm	Z_f mm^3	$f_{cr,d}$ MPa	$M_{cr,d}$ Nm	λ_d	$M_{n,d}$ Nm	**$M_u/M_{n,d}$**	$M_{n,d}$ Nm	**$M_u/M_{n,d}$**
MONO1	**878**	2859	346	989	7062	275	1941	0.71	959	**0.916**	**875**	**1.004**
MONO2	**853**									**0.890**		**0.975**
MONO3	**845**									**0.881**		**0.966**
MEGA1	**679**	2243	388	870	6768	104	704	1.11	628	**1.082**	**559**	**1.214**
MEGA2	**707**									**1.126**		**1.264**
									mean	*0.979*		*1.085*
									stdv	*0.1157*		*0.1428*
									cov	*0.1182*		*0.1317*

Table 3. Distortional Buckling Strength Evaluations Based on Modified Properties

	Test	Values used in Distortional Buckling Strength Calculations							NAS Appendix 1 Eq. (9)		Lecce and Rasmussen, Eq. (10)	
Test ID	**M_u** **Nm**	Z_m mm^3	$\sigma_{0.2}$ MPa	$M_{0.2,m}$ Nm	$Z_{f,m}$ mm^3	$f_{cr,dm}$ MPa	$M_{cr,dm}$ Nm	λ_{dm}	$M_{n,dm}$ Nm	**$M_u/M_{n,dm}$**	$M_{n,dm}$ Nm	**$M_u/M_{n,dm}$**
MONO1	**878**	2729	346	944	6144	422	2590	0.60	944	**0.930**	907	**0.968**
MONO2	**853**									**0.903**		**0.940**
MONO3	**845**									**0.895**		**0.931**
MEGA1	**679**	1871	388	726	3543	355	1258	0.76	679	**1.000**	618	**1.098**
MEGA2	**707**									**1.041**		**1.144**
									mean	*0.954*		*1.016*
									stdv	*0.0641*		*0.0979*
									cov	*0.0672*		*0.0963*

As shown in Table 2, the NAS Appendix 1 [2] Eq. 9 provides reasonable moment capacities ($M_{n,d}$) for the more slender (λ_d=1.11) Megaclad section but is unconservative for the stockier Monoclad section (λ_d=0.71). The NAS Appendix 1 [2] for cold-formed carbon steel does not account for the stainless steel material nonlinearity and this partly explains why the Monoclad strength ratios ($M_u/M_{n,d}$) are less than unity. The distortional buckling DSM curve developed for ferritic alloys given by Eq. 10 offers an improvement to Eq. 9 giving a mean test to predicted strength ratio $M_u/M_{n,d}$ of 1.085 compared with the mean $M_u/M_{n,d}$ = 0.979.

If flange curling effects are taken into account in the distortional buckling strength calculations, as shown in Table 3, then more consistent, but not necessarily more conservative, results are obtained. The coefficients of variation (COV) given in Table 3 (0.0672, 0.0963) are significantly less than those given in Table 2 (0.1182, 0.1317). Also, it is clear from the results of Tables 2 and 3 that flange curling effects have the greatest impact on the design moment capacities of the more slender

Megaclad section. This is unsurprising since this section has been shown to have the greatest enhancement in distortional buckling stress and the greatest decrease in section modulus (see Table 1). The average $M_u/M_{n,d}$ ratio has decreased from an average of 1.239 (Table 2) to an average of 1.121 (Table 3). Therefore, the combination of increased critical buckling stress (and decreased slenderness) and reduced section modulus results in an average net increase in predicted capacity of 10.6%. The discrepancy between the Monoclad and Megaclad evaluations can be explained by the sections' sensitivity to flange curling.

Tables 4 and 5 gives the local buckling strength evaluations using the NAS Appendix 1 [2] (Eq. 11) and the Winter curve (Eq. 12). The evaluations given in Table 4 are based on original cross-sectional properties and associated critical buckling stresses whereas those given in Table 5 account for flange curling and are based on modified geometric properties and associated critical buckling stresses.

Table 4. Local Buckling Strength Calculations Based on Original Properties

	Test	Values used in Local Buckling Strength Calculations							NAS Appendix 1 Eq. (11)		Winter, Eq. (12)	
Test ID	**M_u Nm**	Z mm^3	$\sigma_{0.2}$ MPa	$M_{0.2}$ Nm	Z_f mm^3	$f_{cr,l}$ MPa	$M_{cr,l}$ Nm	λ_l	$M_{n,l}$ Nm	**$M_u/M_{n,l}$**	$M_{n,l}$ Nm	**$M_u/M_{n,l}$**
MONO7	**1179**	2859	346	989	2859	1371	3920	0.50	989	**1.192**	989	**1.192**
MONO8	**1121**									**1.133**		**1.133**
MEGA3	**726**	2243	388	870	2243	671	1506	0.76	870	**0.834**	814	**0.892**
MEGA4	**748**									**0.859**		**0.919**
									mean	*1.005*		*1.034*
									stdv	*0.1841*		*0.1505*
									cov	*0.1833*		*0.1455*

Table 5. Local Buckling Strength Evaluations Based on Modified Properties

	Test	Values used in Local Buckling Strength Calculations							NAS Appendix 1 Eq. (11)		Winter Eq. (12)	
Test ID	**M_u Nm**	Z_m mm^3	$\sigma_{0.2}$ MPa	$M_{0.2,m}$ Nm	$Z_{f,m}$ mm^3	$f_{cr,lm}$ MPa	$M_{cr,lm}$ Nm	λ_{lm}	$M_{n,lm}$ Nm	**$M_u/M_{n,lm}$**	$M_{n,lm}$ Nm	**$M_u/M_{n,lm}$**
MONO7	**1179**	2632	346	911	2632	1509	3972	0.48	911	**1.295**	911	**1.295**
MONO8	**1121**									**1.231**		**1.231**
MEGA3	**726**	1858	388	721	1858	824	1532	0.69	721	**1.007**	714	**1.017**
MEGA4	**748**									**1.038**		**1.048**
									mean	*1.143*		*1.148*
									stdv	*0.1418*		*0.1360*
									cov	*0.1241*		*0.1185*

The predicted capacity given in Table 4 for both Monoclad and Megaclad sections is governed by the yield moment (i.e., $M_{n,l} = M_{0.2}$) except for the Winter evaluation for the more slender Megaclad section. The Winter curve given by Eq. 12 is marginally more conservative than Eq. 11 and this translates to a marginal improvement in the mean test to predicted strength ratio ($M_u/M_{n,l}$=1.005 given by Eq. 11 compared with $M_u/M_{n,l}$=1.034 given by Eq. 12).

If flange curling is considered in the local buckling strength evaluation, as shown in Table 5, then there is an improvement in the predicted moment capacities. Flange curling has the effect of decreasing the section modulus (Z) and since $M_{0.2}=\sigma_{0.2}Z$ (or $M_y=f_yZ$), the moment at which yielding occurs also decreases. The $M_u/M_{n,l}$ ratio for the Monoclad section changes from an average of

1.163 (Table 4) to an average of 1.263 (Table 5) and therefore the design evaluations become even more conservative if flange curling is taken into account. This is primarily because the section is fully effective (λ_l=0.50 and λ_{lm}=0.48), and hence parts of the cross-section are capable of reaching stresses higher than the 0.2% proof stress. Referring to Table 5, the mean test to predicted strength ratios $M_u/M_{n,lm}$ given by Eq. 11 and Eq. 12 are 1.143 and 1.148, respectively.

Comparing the results of the Megaclad to Monoclad sections in Tables 4 and 5, it is clear that the improvement in strength predictions is more significant for the Megaclad section. That is, the predicted local buckling capacity ($M_{n,l}$) is reduced by 12.2% if modified properties are considered, and the $M_u/M_{n,l}$ ratio increases from an average of 0.906 to 1.033 (using the Winter curve evaluation).

Overall, if distortional buckling is considered (wide flange in compression) then the flange curling effects produce a net increase in the predicted capacities. However, if local buckling is considered (wide flange in tension) then the flange curling effects produce a net decrease in the predicted capacity. Furthermore, the evaluations based on Eq. 10 for distortional buckling and Eq. 12 for local buckling provide more conservative results than the NAS Appendix 1 [2] predictions and would be more suitable for the design of stainless steel sections.

Given the present data, it would be prudent to ignore the effects of flange curling to determine the moment capacity for distortional buckling but include them to determine the moment capacity for the local buckling mode. As shown in Lecce and Rasmussen [5], flange curling deformations can be determined sufficiently accurate from an analysis based on the original cross-section geometry, (while the applied stress distribution cannot). A suitable design procedure for sections with the wide flange in tension can therefore be suggested as follows:

- Determine the design moment ($M_{n,l}$) on the basis of the original cross-section geometry using the Direct Strength Method
- Determine the flange curling deformations at this moment, e.g. as per [5]
- Modify the cross-section geometry to account for flange curling deformations
- Determine the design moment capacity for the modified cross-section using the Direct Strength Method

It is recognized that these recommendations are based on relatively few results and more data are required to establish the geometric limits for which flange curling becomes sufficiently significant to adversely affect the capacity and the design procedure would have to be reassessed given more data. For the assessment presented here, it is reasonable to ignore the effects of flange curling for the stockier Monoclad section whether designing against local or distortional buckling, but the same simplification would not be appropriate for the Megaclad section. Finally, there is now an understanding of the flange-curling phenomenon, how it affects the distortional and local buckling behaviour and its impact on the design of stainless steel roof sections.

4. CONCLUSIONS

The results of elastic buckling analysis of wide-flange roof sections both ignoring and including flange curling deformations have been presented. Overall, an increase in elastic buckling stress results when flange curling deformations are included. For the sections investigated, the influence of flange curling is greater for the more slender Megaclad section, with a wide-flange width-to-thickness ratio of 328, and there is an increase in the critical elastic distortional buckling stress by a factor of 3.41 compared to that based on an analysis without flange curling considered.

The critical elastic local buckling stress increased by a factor of 1.23 due to flange curling for the Megaclad section. Flange curling also has the effect of decreasing the section modulus, amounting to reductions of 6% and 16.9% for the Monoclad and Megaclad sections, respectively.

The assessment of design equations for the distortional and local buckling of roof sections subject to bending shows significant scatter in the results if flange curling effects are ignored. A marked decrease in the scatter of results can be achieved by including the effects of flange curling in the design. Given the present data, it is recommended that the effects of flange curling should be ignored in the prediction of distortional buckling moment capacity but that they should be included in the prediction of local buckling moment capacity. The proposed DSM for the distortional buckling of stainless steel sections, given by Eq. 10 (based on Lecce and Rasmussen [1]), and the Winter curve for local buckling, given by Eq. 12 (with modified properties and stresses to account for flange curling) are more suitable for predicting the moment capacities than the current NAS Appendix 1 [2] for cold-formed carbon steel.

REFERENCES

[1] Lecce, M., and Rasmussen, K.J.R., “Distortional Buckling of Cold-Formed Stainless Steel Sections: Finite Element Modeling and Design”, Journal of Structural Engineering, 2006, Vol. 134, No. 4, pp. 505-514.

[2] AISI, “North American Specification for the Design of Cold-Formed Steel Structural Members”, 2007, American Iron and Steel Institute, Washington, D.C.

[3] Lecce, M., and Rasmussen, K.J.R., “Experimental Investigation of Wide Flange Stainless Steel Sections in Bending”, Proceedings of the 6th International Conference on Steel and Aluminium Structures, Ed. R.G. Beale, Oxford, July 2007, pp. 1033-1040.

[4] Lecce, M., and Rasmussen, K.J.R., “Nonlinear Flange Curling of Wide-Flange Sections”, Research Report No. 850, 2005, Department of Civil Engineering, University of Sydney, Sydney.

[5] Lecce, M., and Rasmussen, K.J.R., “Nonlinear Flange Curling in Wide Flange Sections”, Journal of Constructional Steel Research, 2008, Vol. 64, No. 7-8, pp. 779-784.

[6] Winter, G., “Stress Distribution in and Equivalent Width of Flanges of Wide, Thin-Walled Steel Beams”, NACA Technical Note, 1940 (784).

[7] Bernard, E.S., Bridge, R.Q., and Hancock, G.J., “Flange Curling in Profiled Steel Decks”, Thin-Walled Structures, 1996, Vol. 25, No. 1, pp. 1-29.

[8] Bernard, E.S., Bridge, R.Q., and Hancock, G.J., “Design Methods for Profiled Steel Decks with Intermediate Stiffeners” Journal of Constructional Steel Research, 1996, Vol. 38, No. 1, pp. 61-88.

[9] Davies, J.M., and Chiu, R., “Flange Curling in Slender Sections” Proceedings of the 4th Specialty Conference on Cold-Formed Steel Structures, Ed. J. Loughlan, 2004. Loughborough, UK, IOP Publishing Ltd., pp. 39-55.

[10] AS/NZS 4673, “Cold-Formed Stainless Steel Structures”, Australian Standard/New Zealand Standard 4673:2001, 2001, Standards Australia, Sydney, Australia.

[11] Lecce, M., and Rasmussen, K.J.R., “Experimental Investigation of Stainless Steel Roof Sections in Pure Bending”, Research Report No.847, 2005, Department of Civil Engineering, University of Sydney, Sydney.

[12] Papangelis, J.P., and Hancock, G.J., “Computer Analysis of Thin-Walled Structural Members. Computers & Structures”, 1995, Vol. 56, No. 1, pp. 157-176.

[13] Rasmussen, K.J.R., Burns, T., and Bezkorovainy, P., “Design of Stiffened Elements in Cold-Formed Stainless Steel Sections”, Journal of Structural Engineering, 2004, Vol. 130, No. 11, pp. 1764-1771.

FULL – SCALE TESTS ON COLD-FORMED STEEL PITCHED-ROOF PORTAL FRAMES WITH BOLTED JOINTS

D. Dubina[1*], A. Stratan[1] and Zs. Nagy[2]

[1]Politehnica University of Timisoara, Faculty of Civil Engineering,
Department of Steel Structures and Structural Mechanics,
str. Ioan Curea nr.1, Timisoara 300224, Romania
tel/fax: ++40.256.403932
[2]Gordias SRL, Bucharest, Romania
**(Corresponding author: E-mail: dan.dubina@ct.upt.ro)*

ABSTRACT: The paper summarises the results of an experimental program carried out in order to evaluate the performance of pitched roof cold-formed steel portal frames of back-to-back channel sections and bolted joints. Three different configurations of ridge and eaves joints were tested. The behaviour and failure mechanisms of joints were observed in order to evaluate their stiffness, strength and ductility. Joints between cold-formed members with bolts in the web only result in a reduction of joint moment capacity and premature web buckling. The component method was applied in order to characterise the joint stiffness and moment capacity for the purpose of frame analysis and design. The influence of joints characteristics on the global frame response under lateral (seismic) loads was analysed by considering three connection models. Full-scale tests were performed on cold-formed pitched-roof portal frames. The paper presents experimental observations and comparison to numerical predictions of frame response.

Keywords: Cold formed construction, pitched roof portal frames, joint behaviour, full-scale tests

1. INTRODUCTION

Previous studies by Lim and Nethercot [1] and Chung and Lau [2] showed that bolted joints in cold formed steel portal frames have a semi-rigid behaviour. Also, these types of joints are partially resistant (Lim and Nethercot [3]). When bolts are installed only on the web of cold-formed section, the local buckling is made more critical by stress concentrations, shear lag and bearing deformations around bolt holes (Dundu and Kemp [4]), reducing the moment resistance well below the moment resistance of the effective cross-section. In case of usual cold-formed steel sections, both tests and numerical simulations show that elastic-plastic elongation of bolt-holes is by far the most important component controlling the stiffness and capacity of such type of connections (Lim and Nethercot [1], Yu et al. [5]). The contribution of other components, such as flanges in tension and compression due to bending action, and the web in shear due to transverse action is significantly lower.

The global behaviour of cold-formed steel portal frames of bolted joints was studied experimentally by Lim [6], Dundu and Kemp [4], and Kwon et al. [7]. All these studies provided evidence of the crucial importance of joint performance on the global response of frames.

In present paper, the influence of joint characteristics on the global behaviour of cold-formed pitched-roof portal frames is investigated. An experimental program on ridge and eaves joints was carried out. Detailed results on joint behaviour are reported elsewhere (Dubina et al. [8]). Based on experimental results, a calculation procedure based on the component method (EN1993-1-8 [9]) was adapted to cold-formed joints. Joint stiffness and moment capacity obtained using the component method is used to develop a joint model for global structural analysis. Two full-scale tests on cold-formed pitched-roof portal frames with bolted joints were performed, with the primary objective to assess their performance under horizontal (seismic) loading. The results of the experimental investigation are presented and experimental response is compared to analytical predictions of frame response.

2. SUMMARY OF TESTING PROGRAM ON JOINT SPECIMENS

2.1 Specimens

In order to be able to define realistic specimen configurations a simple pitched roof portal frame was first designed with the following configuration: span 12 m; bay 5 m; eaves height 4 m and roof angle 10°. This frame was subjected to loads common in the Romanian design practice: self weight 0.35 kN/m^2 (with a partial safety factor of γ_{ULS}=1.1 for the ultimate limit state), technological load 0.15 kN/m^2 (γ_{ULS}=1.1) and snow load 0.72 kN/m^2 (γ_{ULS}=2.0). These loads were totalling approximately 10 kN/m uniformly distributed load on the frame. The frame was analysed and designed according to EN 1993-1-3 (2001) 0 rules. The size of knee and ridge specimens and testing setup were chosen to obtain in the connected members a distribution of bending moment similar to the one observed in the designed structure.

The elements of the portal frame were made from back-to-back built up sections made of Lindab C350/3.0 profiles (yield strength f_y=350 N/mm^2). Using these cross section dimensions, three alternative joint configurations were designed (see Figure 1 and Figure 2), using welded bracket elements (S235: f_y=235 N/mm^2)

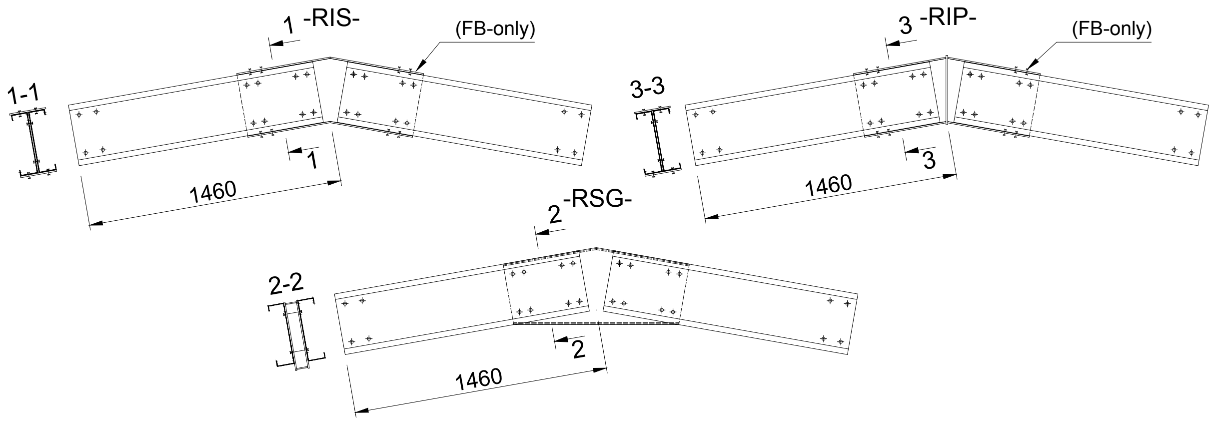

Figure 1. Configurations of Ridge Joints

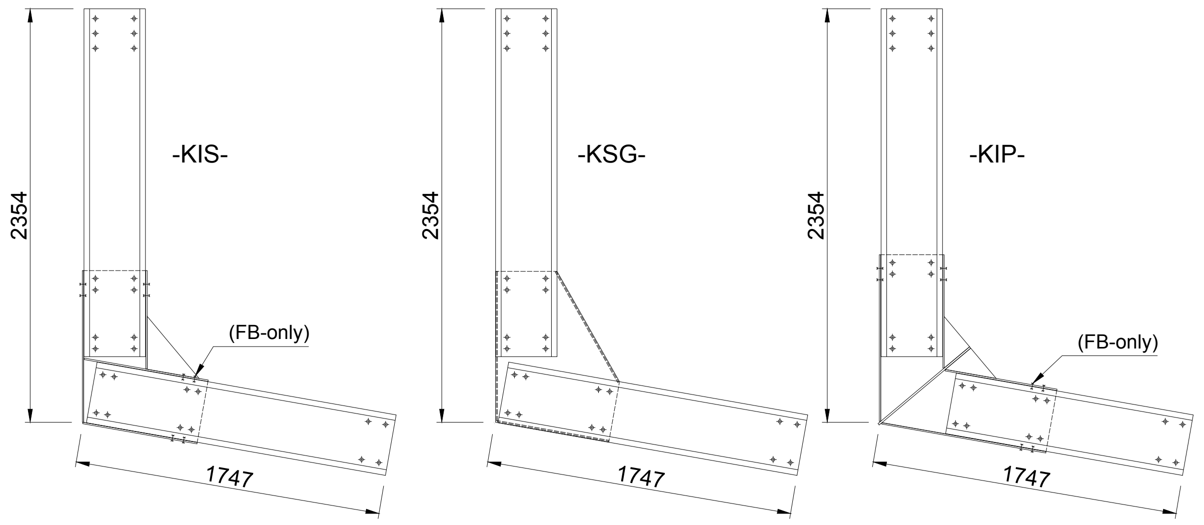

Figure 2. Configurations of Knee Joints

The connecting bolts are subjected to shear and their design was carried out assuming the rotation of the joint around the centroid of the bolt group and a linear distribution of forces in each bolt, proportional to their distance from the centre of rotation. The joints were designed to resist the bending moment in the beam, at the location of the centroid of the bolt group.

One group of specimens (KSG and RSG) used spaced built-up gussets. In this case, bolts were provided only on the web of the C350 profile. In the other cases, where two different details were used for the connecting bracket – i.e. welded I sections only (KIS and RIS), and welded I section with plate bisector (KIP and RIP), respectively - bolts were provided on the web only, or both on the web and the flanges. Joints where bolts were provided on the web and on flanges were denoted by FB letters (see Table 1).

Table 1. Tests on Joint specimens

Element type	Code	Loading type
RIS (Ridge connection with I Simple profile)	RIS-FB-M	Monotonic
	*RIS-FB-C1**	Cyclic: modified ECCS
	*RIS-FB-C2**	Cyclic: low cycle fatigue
RSG (Ridge connection with Spaced Gusset)	RSG-M	Monotonic
	RSG-C1	Cyclic: ECCS procedure
	RSG-C2	Cyclic: Modified ECCS
RIP (Ridge connection with I profile and end Plate)	RIP-M	Monotonic
	RIP-M	Monotonic
	RIP-C1	Cyclic - ECCS proc.
KSG (Knee connection with Spaced Gusset)	KSG-M	Monotonic
	KSG-C1	Cyclic - Modified ECCS
	KSG-C2	Cyclic - Low cycle fatigue
KIS (Knee connection with I Simple profile)	KIS-M	Monotonic
	*KIS-FB-M**	Monotonic
	*KIS-FB-C**	Cyclic - Modified ECCS
KIP (Knee connection with I profile and end Plate)	KIP-M	Monotonic
	*KIP-FB-M**	Monotonic
	*KIP-FB-C**	Cyclic - Modified ECCS

*FB Specimens (RIS, RIP, KIS, KIP) with supplementary bolts on the flange

2.2 Test Setup

Monotonic and cyclic experiments were performed for each specimen typology, all specimens being tested statically. Figure 3 shows the test setup and specimen instrumentation. In the knee connection tests, a short tie was used to prevent vertical displacements of the joint. For monotonically loaded specimens the loading velocity was approximately 3.33 mm/min, and the "yield" displacement (v_y) was determined according to the ECCS [11] procedure, as the displacement corresponding to the intersection of the initial stiffness line and another line with a slope of 10% of the initial stiffness (see Figure 4a). For the cyclic tests several alternative loading procedures were used: (1) the standard ECCS cyclic procedure (see Figure 4b), (2) a modified cyclic procedure, suggested by the authors, which is based on the ECCS proposal (see Figure 4c) and (3) a cyclic procedure for low cycle fatigue. The ECCS loading procedure consists of four initial cycles in the elastic range, followed by groups of three inelastic cycles at $\pm 2v_y$, $\pm 4v_y$, $\pm 6v_y$, etc. The inelastic demand imposed on cold-formed specimens following this procedure is too severe, the specimen failing during the first inelastic cycle at $\pm 2v_y$. To overcome this problem, a modified procedure was used, that consisted of four initial cycles in the elastic range, followed by groups of three inelastic cycles at $\pm 1.2v_y$, $\pm 1.4v_y$, $\pm 1.6v_y$, etc.

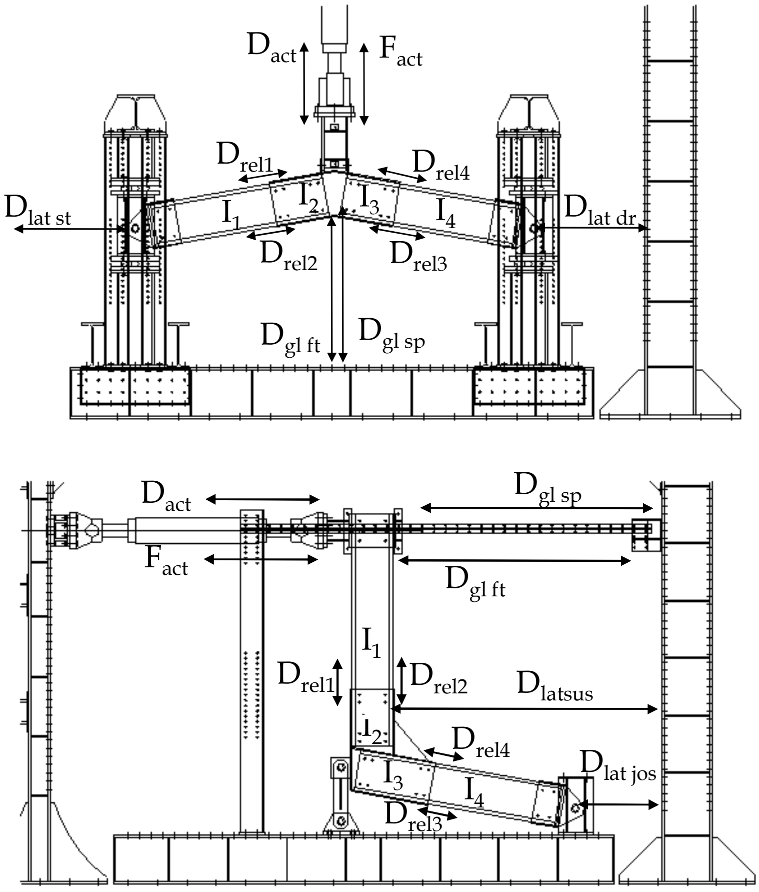

Figure 3. Loading Scheme and Instrumentation

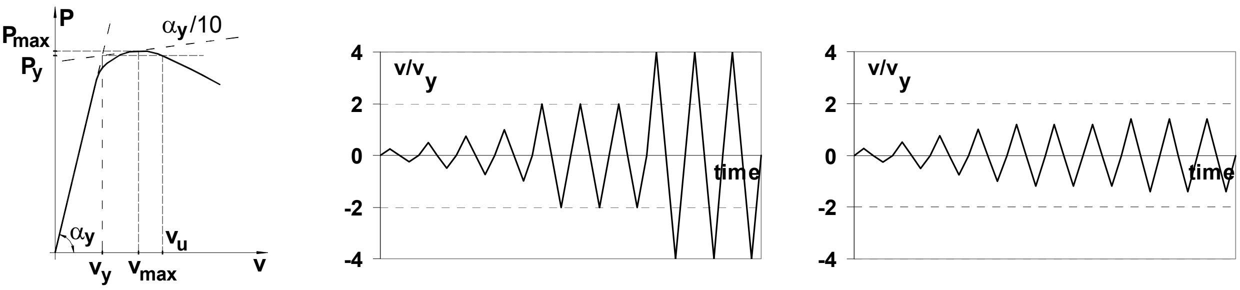

(a) (b) (c)

Figure 4. ECCS Procedure for Determining the Yield Displacement (a);
ECCS Loading Procedure (b) and Modified Loading Procedure (c)

2.3 Monotonic Tests

The monotonic tests identified failure modes of the different joint typologies. All specimens had a failure due to local buckling of the cold formed profiles; however two distinctive modes were identified for specimens with flange bolts and those without (Figure 5; Figure 6).


(a) (b)

Figure 5. Failure of Ridge Specimens RIP-M (a) and RIS-FB-M (b)

If no bolts are provided on the flange of profiles, initially minor bearing elongation of the bolt holes were observed, the failure being due to stress concentration in the vicinity of outer bolt row. The resulting concentration of compressive stress in the web of the C profile causes in the ultimate stage local buckling followed suddenly by web-induced flange buckling. This phenomenon occurred in a similar way in the case of RSG and KSG specimens. No important differences were observed between specimens where no bolts were provided on the flanges. In the case of the specimens with flange bolts, the stresses concentrated in the vicinity of the outer bolt row on the flange. In this case no initial elongation of the bolt holes were observed; the buckling was firstly initiated in the flange, and only later was extended into the web.

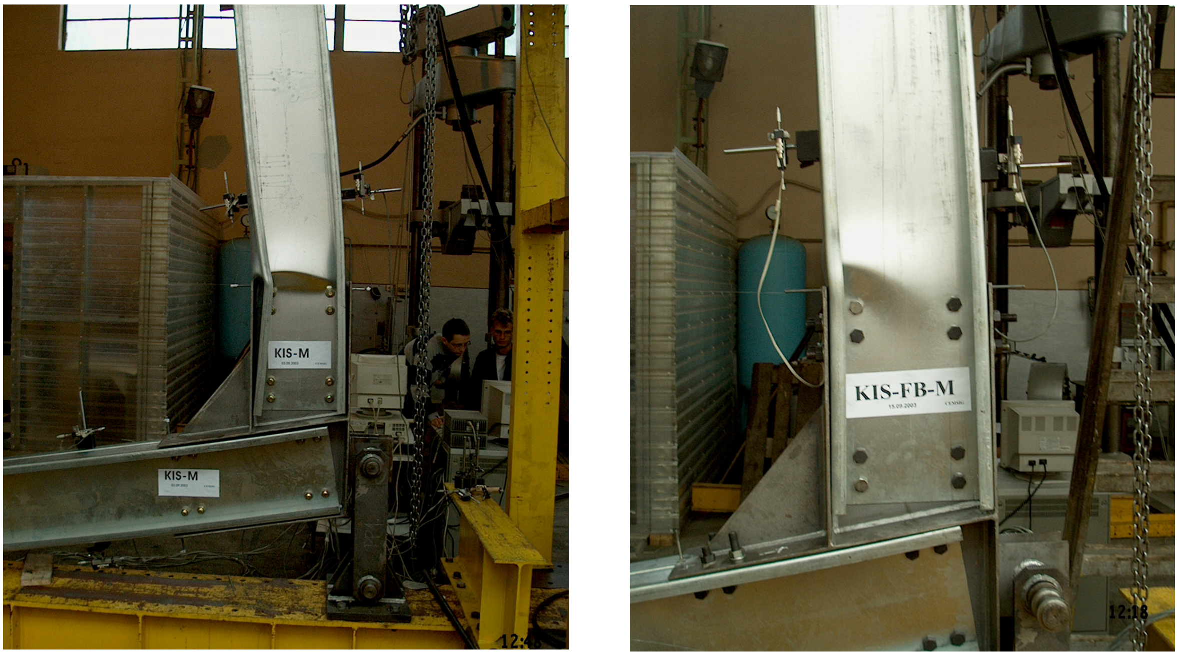
(a) (b)

Figure 6. Failure of Knee Specimens KIS-M (a) and KIS-FB-M (b)

Figure 7. Two Possible Models for Ridge Joints: Detailed (a) and Simplified (b)

To account for the flexibility of the bolted connection in structural analysis, two models are possible: one which considers both connections independently (see Figure 7a), and a simplified one, which considers the characteristics of the connection concentrated in one joint only (see Figure 7b). The former is believed to represent more exactly the real behaviour of the assembly, while the latter has the advantage of simplicity. Similar models can be used for knee joint configurations. Moment-rotation relationships characterising the connection response were derived for both the left and right ridge connections (beam and column connection in the case of knee joins). Moments were computed at the end of the bracket. The corresponding relative rotation between the bracket and the connected element $\theta_C{}^*$ was determined from acquired data, so as to represent both the flexibility of the connection (due to bolt bearing) and post-buckling deformations in the element (Dubina et al. [8]). For the simplified joint representation (as in Figure 7b), both moment (M_j) and rotations were considered at the intersection of the element centrelines.

Comparative experimental curves for ridge and knee connections are presented in Figure 8a and Figure 9. There are no significant differences among the specimens without flange bolts (RSG-M, RIP-M, and KSG-M, KIS-M). This could be explained by the higher stiffness and capacity of the connecting bolts compared to the other components of the joint. On the other hand, there is an important gain in load bearing capacity and the initial joint stiffness when bolts are installed also on the flanges, although this joint type is more difficult to fabricate (RIS-FB-M and KIS-FB-M).

In Table 2 the yield and ultimate rotation ($\theta_{C,y}{}^*$; $\theta_{C,u}{}^*$), the initial stiffness (K_{iniC}), and the maximum bending moment ($M_{C,max}$) are presented and compared for all monotonically tested specimens, for the failed connection. The initial stiffness was determined by a linear fit of moment-rotation values between 0.25 and 0.9 of the maximum moment. The lower-bound limit (0.25) was chosen different from zero in order to eliminate the effect of initial slip due to tolerance of bolt-holes. This initial slip is believed to be ineffective in the real structure, due to loading-unloading cycles under service loads. The upper-bound limit (0.9) was considered empirically as a limit of elastic response of the connection. Yield rotation was determined as the point on the initial stiffness line corresponding to maximum moment. Ultimate rotation was defined as the one corresponding to a 10% drop of moment capacity relative to the maximum moment. Figure 8b presents graphically determination the initial stiffness, yield rotation and ultimate rotation for the RIS-FB-M specimen.

Obviously, the specimens with unbolted flanges that failed prematurely by web buckling due to stress concentration around the outer bolt rows, would be the weakest part of portal frames. Consequently, this joint typology is not recommended to be used in practice.

Table 2. Monotonic Results: Parameters of Connection Moment-Rotation Curves

Specimen	K_{iniC} kNm/rad	$\theta_{C,y}^{*}$ Rad	$\theta_{C,u}^{*}$ rad		M_{Cmax} kNm
RSG-M	4891.3	0.021	0.034	1.6	77.1
RIS-FB-M	6011.1	0.017	0.025	1.4	108.0
RIP-M	5806.8	0.018	0.028	1.6	74.3
RIP-M2	6541.2	0.012	0.013	1.1	72.9
KSG-M	6031.6	0.009	0.023	2.5	53.3
KIS-M	4115.0	0.020	0.033	1.6	78.4
KIS-FB-M	6432.3	0.016	0.029	1.8	102.9
KIP-M	7863.9	0.010	0.019	2.0	90.0
KIP-FB-M	6956.5	0.015	0.025	1.6	116.7

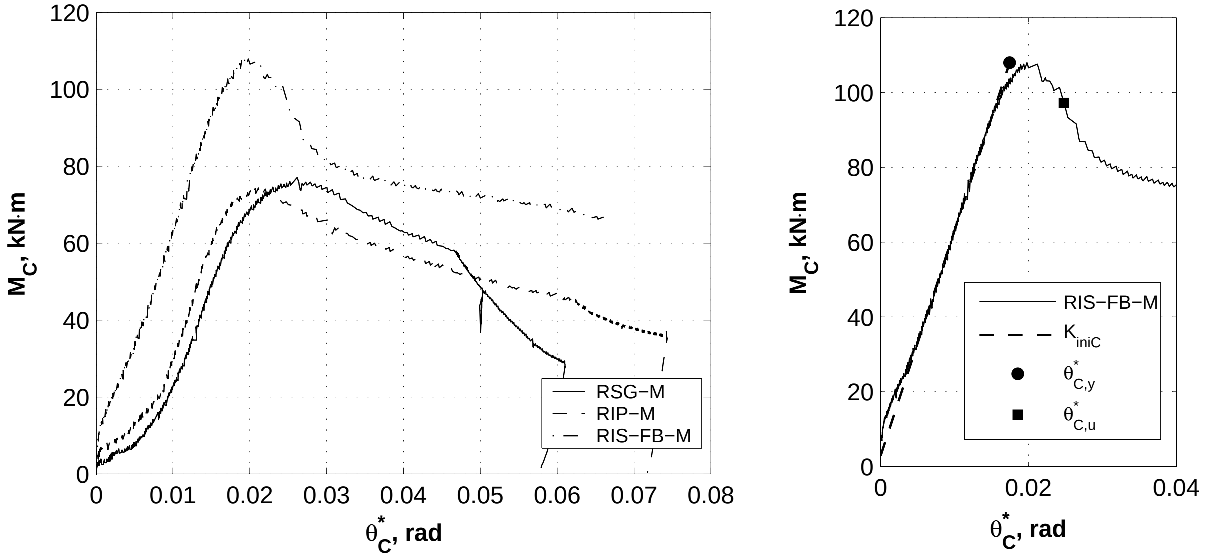

(a) (b)

Figure 8. Comparative Results from Monotonic Tests for Ridge Joints (a) and Graphical Representation of Initial Stiffness, Yield and Ultimate Rotations for the RIS-FB-M Specimen (b)

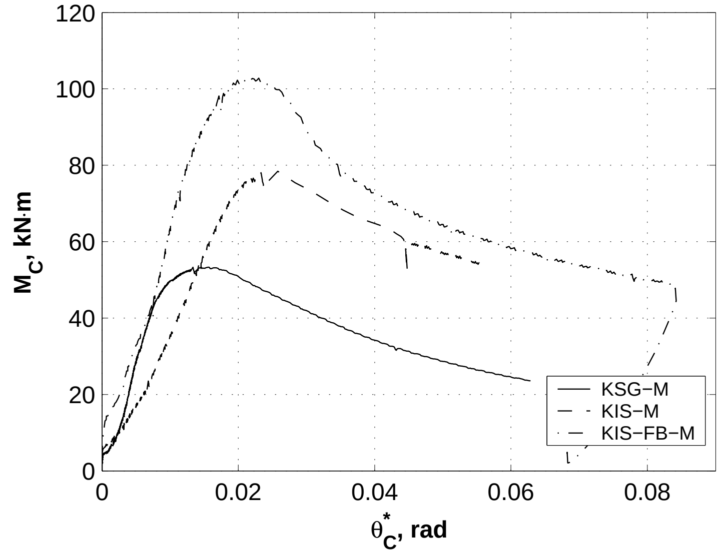

Figure 9. Comparative Results from Monotonic Tests for Knee Joints

2.4 Cyclic Tests

In the case of cyclic loading, failure of specimens started by elongation of bolt holes. Compared to monotonic loading, in the case of cyclic loading the phenomenon was amplified due to the repeated and reverse loading. However, the failure occurred also by local buckling, as in monotonic tests, but at the repeated reversals, the buckling occurred alternately on opposite sides of the profile. This repeated loading caused the initiation of a crack at the corner of the C profile, in 2-3 cycles following the buckling, closed to the point where the first buckling wave was observed in the flange.

The crack gradually propagated through the flange and web, causing an important decrease of the load bearing capacity in each consecutive cycle.

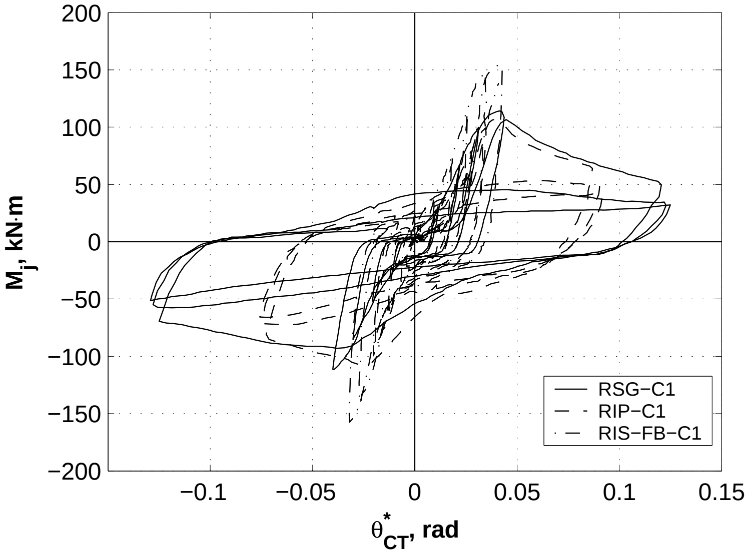

Figure 10. Comparative Results from Cyclic Tests on Ridge Specimens

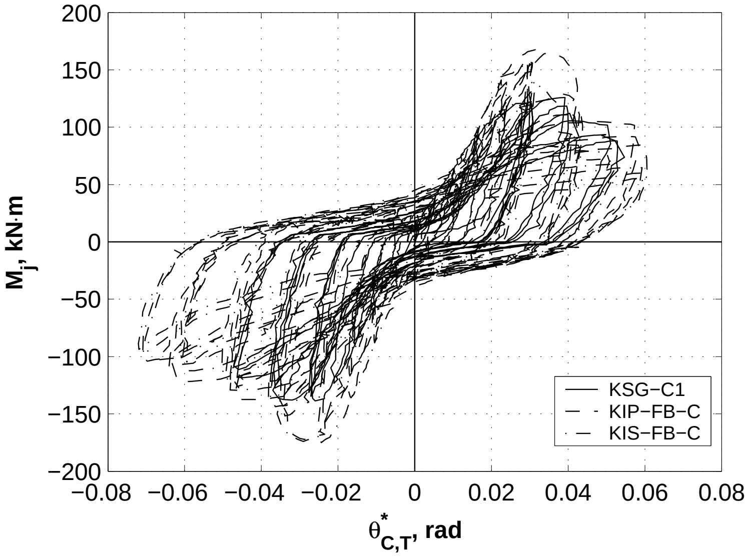

Figure 11. Comparative Results from Cyclic Tests on Knee Specimens

Table 3. Cyclic Results: Parameters of Connection Moment-Rotation Curves

Specimen	K_{iniC} kNm/rad	$\theta_{C,y}^{*}$ rad	$\theta_{C,u}^{*}$ rad	μ	M_{Cmax} kNm
RSG-C1	5060.0	0.017	0.028	1.7	78.8
	-5400.3	-0.019	*	*	-76.8
RSG-C2	4502.9	0.018	0.028	1.6	76.0
	-2792.5	-0.029	-0.036	1.2	-78.1
RIS-FB-C1	*	*	*	*	106.9
	*	*	*	*	-108.6
RIS-FB-C2	*	*	*	*	100.2
	*	*	*	*	-111.5
RIP-C1	6642.1	0.014	*	*	73.8
	-6585.1	-0.013	*	*	-74.7
KSG-C1	5395.5	0.013	0.022	1.7	82.5
	-6672.4	-0.015	-0.028	1.9	-90.9
KSG-C2	5067.6	0.014	0.022	1.5	84.5
	-4684.1	-0.014	-0.017	1.2	-76.8
KIS-FB-C	6914.7	0.014	0.021	1.5	102.3
	-9201.5	-0.012	-0.023	2.0	-114.4
KIP-FB-C	10051.8	0.012	0.026	2.1	102.2
	-8193.5	-0.011	-0.021	1.9	-105.1

* results not available due to faulty data acquisition

The hysteretic M-θ curves show a stable behaviour up to the yield limit ($\theta_{C,y}^{*}$) with a sudden decrease of the load bearing capacity afterwards (Figure 10 and Figure 11). Therefore the low ductility of the specimens must be underlined again. Further, the cycles show the effect of slippage in the joint (i.e. pinching) and strength degradation in repeated cycles. Strength degradation is most significant in the first cycle, while in the consequent ones the behaviour is more stable.

In order to obtain connection characteristics under cyclic loading, an unstabilised envelope was first determined, by considering the points corresponding to maximum moment in each cycle. Based on envelope curves, connection strength, rotation capacity and ductility have been determined following a procedure identical to the one used in the case of monotonic specimens, and are reported in Table 3. Again, joints without flange bolts were weaker.

3. THE COMPONENT METHOD

The component method is a general procedure for the design of the strength and stiffness of joints in building frames, and is implemented in EN1993-1-8 [9]. The procedure is primarily intended for heavy-gauged construction. Its application to joints connecting light-gauge members is investigated in the present paper.

Application of the component method requires the following steps (Jaspart et al. [12]):

- identification of the active components within the joint
- evaluation of the stiffness and strength of individual components
- assembly of the components in order to evaluate stiffness and strength of the whole joint

Based on the conclusions of the experimental programme, the present study investigates only joints with both web and flange bolts (RIS-FB-M, KIS-FB-M, and KIP-FB-M). Qualitative FEM simulation (see Figure 12) showed that in the case of specimens with bolts on the web only there is a stress concentration in the web, which causes premature local buckling failure. The FEM simulation also demonstrated that load distribution in the bolts is not linear. In fact, due to member flexibility and local buckling, the connected members do not behave as rigid bodies, and the centre of rotation of web bolts does not coincide with the centroid of web bolts. The centre of rotation of the connection is shifted towards the outer bolt rows (see Figure 13), whose corresponding force is an order of magnitude higher than the force in the inner bolts. Considering this observation, only the outer bolt group was considered for determination of connection characteristics using the component method. This assumption significantly differ in comparison with the behaviour models considered in the papers of the list of reference, which, all, consider the centroid of the bolt group as the rotation centre.

The centre of compression of the connection was considered at the exterior flange of the cold-formed member (see Figure 13), similarly with the model used for design of bolted connections with angle flange cleats in EN1993-1-8 [9]. There are a total of four bolt rows, of which three bolt rows are in the "tension" zone. The following components were identified and used to model the connection stiffness and strength:

- Cold-formed member flange and web in compression. Only the strength of this component was considered, while stiffness was considered infinite (similarly with Lim and Nethercot [1])
- Bolts in shear
- Bolts in bearing on the cold-formed member
- Bolts in bearing on the bracket

The stiffness and strength of all these components are readily available in EN1993-1-8 [9], only minor adjustments being required for the case of the particular case considered here. In order to facilitate comparison with the experimental results, the measured geometrical characteristics and strength (yield stress f_y = 452 N/mm^2, and tensile strength f_u = 520 N/mm^2) were considered in the case of the cold-formed member. Nominal characteristics were used for the bracket and bolt characteristics, as experimental data was not available. Partial safety factors equal to unity were considered in all cases.

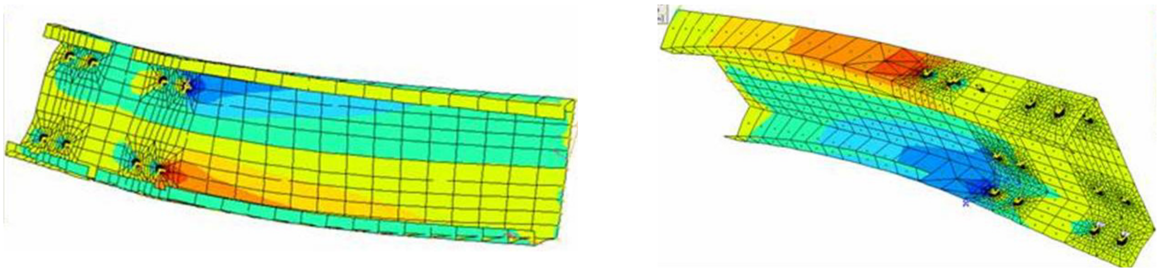
(a) (b)

Figure 12. Stress Concentration in the Case of Specimens with Web Bolts Only (a), and Both Web and Flange Bolts (b)

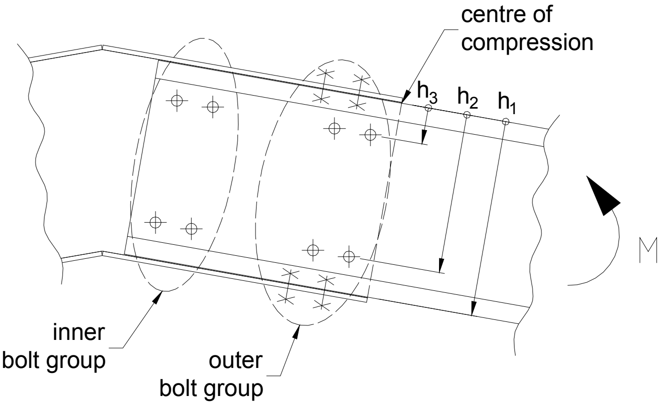

Figure 13. Bolt Groups Considered in Analysis

Only three components were considered to contribute to the stiffness of the connection: bolts in shear (denoted $k_{v,f}$ for flange bolts and $k_{v,w}$ for web bolts), bolts in bearing on cold-formed member (denoted $k_{b,cff}$ for flange bolts and $k_{b,cfw}$ for web bolts), and bolts in bearing on the bracket (denoted $k_{b,bf}$ for flange bolts and $k_{b,bw}$ for web bolts), see Figure 14a. Formulas for determination of stiffness coefficients are available in EN1993-1-8 [9]. For each of the bolt rows r, an effective stiffness coefficient $k_{eff,r}$ is determined, by combining the individual stiffness coefficients using the following relationship (EN1993-1-8 [9], see Figure 14b):

$$k_{eff,r}=\frac{1}{\sum_i \frac{1}{k_{i,r}}} \tag{1}$$

The effective stiffness coefficients of the bolt rows in "tension" zone are replaced by an equivalent spring k_{eq} (EN1993-1-8 [9], see
Figure 14Figure 14c):

$$k_{eq}=\frac{\sum_r k_{eff,r}h_r}{z_{eq}} \tag{2}$$

where h_r is the distance between bolt row r and the centre of compression; z_{eq} is determined using Eq. 3.

$$z_{eq}=\frac{\sum_r k_{eff,r}h_r^{\,2}}{\sum_r k_{eff,r}h_r} \tag{3}$$

Finally, the initial connection stiffness is determined as (see Figure 14d):

$$S_{j,ini}=\frac{E\,z_{eq}^2}{\sum_i 1/k_i} \tag{4}$$

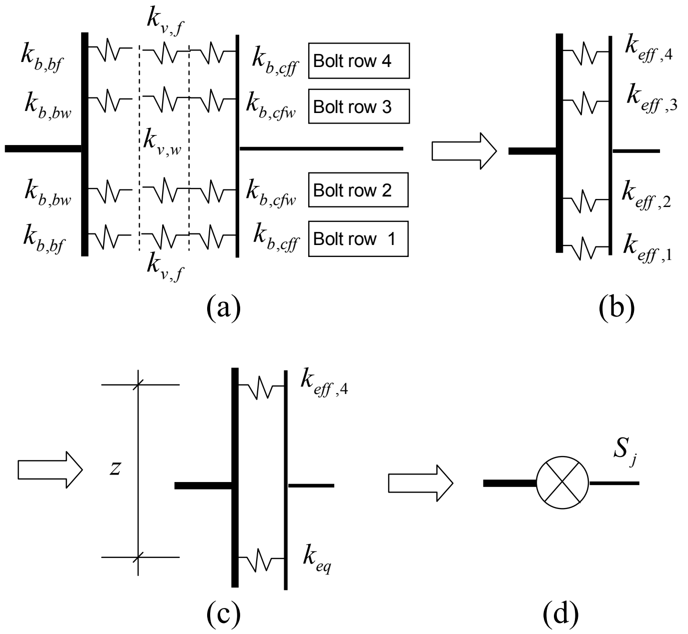

Figure 14. Main Steps in the Assembly of Components for Determination of Connection Stiffness

The moment resistance of the bolted connection was determined using a two-step procedure. In the first step, only components related to bolt resistance were included in order to determine the moment resistance of the bolted connection $M^b_{C,Rd}$. In a second step, the connection moment resistance was obtained as the minimum of the moment resistances of the bolted connection $M^b_{C,Rd}$ and the connected cold-formed member $M_{beam,Rd}$:

$$M_{C,Rd} = \min\left(M^b_{C,Rd}, M_{beam,Rd}\right) \tag{5}$$

The adopted approach for determination of connection moment resistance allows to easily determine if the connection is full-strength or partial strength.

The moment resistance of the bolted connection was determined as (EN1993-1-8 [9]):

$$M^b_{C,Rd} = \sum_r F_{tr,Rd}\, h_r \tag{6}$$

where $F_{tr,Rd}$ is the effective tension resistance of bolt row r (minimum value of components related to bolt row r); h_r is the distance between bolt row r and the centre of compression.

The moment resistance of the cold-formed member $M_{beam,Rd}$ was determined using measured geometrical and mechanical characteristics, using effective cross-section modulus.

It was considered appropriate to use a linear distribution of forces on bolts in the case of a connection to light-gauge members. Therefore, the effective tension resistance of bolt rows was limited according to the following relationship:

$$F_{tr,Rd} \le F_{t1,Rd}\,\frac{h_r}{h_1} \tag{7}$$

where $F_{t1,Rd}$ is the effective tension resistance of bolt row *1* (farthest from the centre of compression); h_1 is the distance between bolt row *1* and the centre of compression.

Table 4 and Table 5 present resistance and stiffness of bolt rows. The weakest component of flange bolts is bearing on cold formed member, while in the case of web bolts it is bearing on bracket (see Table 4). The difference is due to the fact that bolts are in simple shear on flanges and in double shear on web, as well as due to different number of bolts on flanges (4 bolts per row) and web (2 bolts per row). The main contribution to the flexibility of the connection is bearing on the cold-formed member, as well as bearing on bracket in the case of web bolts (see Table 5).

The configuration of the outer group of bolts being the same in the case of all three specimens with web and flange bolts (RIS-FB-M, KIS-FB-M, KIP-FB-M), a single set of analytical connection properties were determined. A comparison of experimental vs. analytical characteristics of connections (stiffness and moment resistance) is presented in Table 6. Generally a fair agreement between experimental and analytical stiffness of the connection can be observed. Larger experimental values of stiffness can be explained by the fact that the contribution of the inner bolt group was ignored in the analytical model. The stiffness of the connection is considerably lower than the EN1993-1-8 limits for classification of joints as rigid ($25EI_b/L_b$), which amounts to 25256 kN/m (considering the beam span L_b equal to frame span and using gross moment of inertia I_b). Therefore, these types of connections are semi-rigid, and their characteristics need to be taken into account in the global design of frame.

Table 4. Resistance of Connection Components

Bolt row	Component			Bolt-row resistance $F_{tr,Rd}$, kN
	Bolts in shear, kN	Bolts in bearing on the cold-formed member, kN	Bolts in bearing on the bracket, kN	
1	361.4	290.6	527.0	290.6
2	361.4	290.6	288.0	288.0
3	361.4	290.6	288.0	288.0
4	361.4	290.6	527.0	290.6

Table 5. Stiffness of Connection Components

Bolt row	Component			Bolt-row effective stiffness $k_{eff,r}$, mm
	Bolts in shear, mm	Bolts in bearing on the cold-formed member, mm	Bolts in bearing on the bracket, mm	
1	2.286	0.7785	1.3886	0.4095
2	2.286	0.7785	0.7714	0.3313
3	2.286	0.7785	0.7714	0.3313
4	2.286	0.7785	1.3886	0.4095

Table 6. Experimental vs. Analytical Connection Characteristics

Specimen	Initial stiffness, K_{iniC} [kNm/rad]		Moment resistance, M_C, [kNm]	
	experimental	analytical	experimental	analytical
RIS-FB-M	6011	5224	108.0	117.8
KIS-FB-M	6432	5224	102.9	117.8
KIP-FB-M	6957	5224	116.7	117.8

The moment resistance of the bolted connection $M^{b}_{C,Rd}$ determined by the component method amounted to 193.9 kNm, which was larger than the moment resistance of the cold-formed member $M_{beam,Rd}$, amounting 117.8 kNm. Therefore, this type of connection is a full-strength one. This was demonstrated also by the experimental results, failure mode being local buckling of the cold-formed member.

4. FULL SCALE TESTS ON PITCHED-ROOF PORTAL FRAMES

4.1 Test Setup

Following experimental tests on cold-formed joints, two full-scale tests on frames were performed. Frame dimensions were chosen identical to the ones in the initial design used to establish the dimensions of tested joints. Considering the poor performance of joints with web bolts only, RIS-FB and KIS-FB configurations (with both web and flange bolts) were used for frame construction. Pinned supports were used at the column bases. The objective of the full-scale tests was to assess the performance of pitched-roof cold-formed portal frames with moment-resisting joints under lateral loading, with particular emphasis on earthquake loading.

The test setup consisted of two frames in upward position, located 1.5 m apart. Tie bracing was provided between the two frames in order to provide out-of plane stability. The purlins were installed on the girders, but no side rails were provided on the columns. The schematic representation of test setup is shown in Figure 15. A reaction frame was used to apply lateral load.

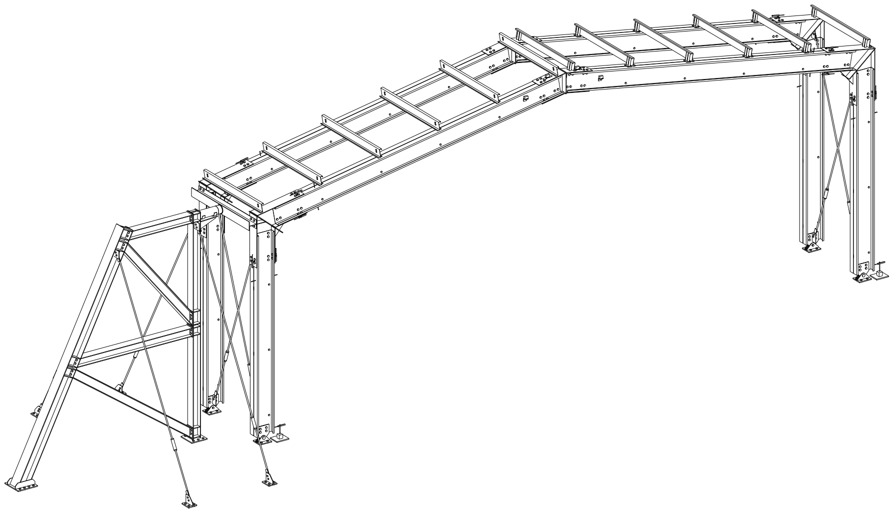

Figure 15. Experimental Test Setup for Full-scale Tests

In the case of the first test (C1), only lateral loading was applied. For the second test (C2), gravity loading corresponding to seismic design situation (permanent and a 0.3 fraction of the snow load) was applied, followed by increasing lateral load up to failure. Total gravity loading amounted to 31.2 kN per frame, and was applied using 30 corrugated steel sheets laid on the purlins. A load cell was used in order to measure lateral load applied through a hydraulic jack. Frames were instrumented with displacement transducer to measure lateral in-plane and out-of plane displacements at the eaves, deflections at the ridge, as well as connection rotations.

4.2 Test Results and Comparison to Numerical Model

Experimental tests on ridge and eaves joints showed that bolted connections of back-to-back channel cold-formed members are semi-rigid, even when bolts are provided not only on the web, but also on the flanges of the channel section. Therefore, deformations can be underestimated if connections are assumed rigid for global frame analysis. In order to assess the influence of connection stiffness and post-buckling resistance, three frame models were analysed (see Figure 16). A nonlinear static analysis under increasing lateral load was applied to the models, and the results were compared to experimental ones.

The first model was a conventional model, where connections were considered rigid. Nominal geometrical characteristics were used to model members. Finite dimensions of brackets were taken into account. Local buckling of members was modelled by rigid-plastic hinges located at the extremities of cold-formed members. an analytically determined moment capacity (M_c=117.8 kNm) was considered.

The second model (M2, see Figure 16b) was obtained from model M1 by adopting an elastic perfectly-plastic model of the connection moment-rotation response. The initial stiffness (K_{iniC}=5224 kNm/rad) and moment capacity (M_c=117.8 kNm) were the ones obtained using the analytical procedure described above (see Table 6).

In the case of the third model (M3, see Figure 16c), the elasto-plastic model was enhanced following two directions. The first one was related to connection behaviour under small loads, when experimental evidence showed a very stiff initial response. This response is attributed to wedging and friction between the cold-formed profiles and the bracket. Consequently, a rigid response was assumed before "slipping" up to moment M_s (see Figure 17a). The value of the "slipping" moment M_s was estimated based on experimental results, a value of 15% from the connection moment capacity being adopted. Following the initial rigid behaviour, the connection model consists of an elastic response at the initial stiffness K_{iniC} (determined using the component method), up to the connection moment capacity M_C.

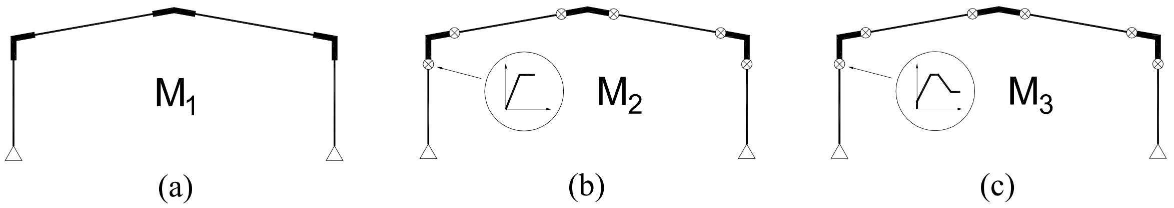

Figure 16. Considered Structural Models: Rigid Connections - M1 (a), Elastic-Perfectly Plastic Connections - M2 (b), and Degrading Connections – M3 (c)

The second enhancement of the model consisted in post-elastic response. The plastic rotation (plateau) was determined assuming an ultimate rotation θ_{Cu} equal to 1.4 times the yield rotation θ_{Cy}. The softening branch was determined by considering a drop of moment capacity to 50% from the maximum one, at a rotation θ_{Cr} of 4.0 times the yield rotation (see Figure 17a). The same moment-rotation characteristics were used for all connections (for both beams and columns). The influence of axial force on the stiffness and moment resistance of the connection were ignored. A comparison between the analytical model and the experimental moment-rotation curves is shown in Figure 17b.

Figure 18a shows a global view of the C1 frame (tested under horizontal loading only) after the test. The frame response during the test was characterised by an almost linear response up to the first local buckle of the beam at the connection 2 (see Figure 18b, Figure 19, and Figure 20a), followed by a rapid loss of global frame resistance. The final collapse mechanism consisted of hinging of the beam at connections 2 and 5 (see Figure 20b) near the eaves.

A comparison of the experimental and numerical lateral force – deformation curves for the C1 frame is shown in Figure 19. The force corresponds to one of the two frames from the experimental setup, assuming the force equally distributed between the two frames. It can be observed that the rigid model (M1) provides a good approximation of the initial response of the frame up to lateral forces of about 10 kN. At larger forces, model M2, with semi-rigid connections, provide a better approximation of the experimental response. The M3 model, incorporating both the initial rigid response and subsequent semi-rigid behaviour shows the best agreement to the experimental results. The same pattern of member hinging as in the one observed in the experiment is obtained for the numerical model (see Figure 20b for the case of the M3 model). The M3 model captures well the initial and post-buckling response. M2 model overestimates lateral deformations. All three models slightly underestimate the global frame resistance.

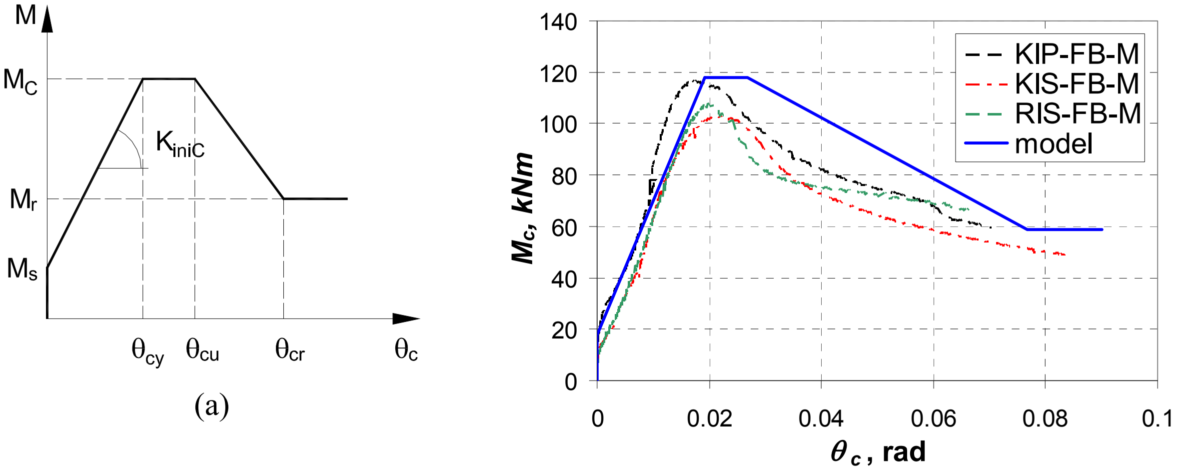

(a)

(b)

Figure 17. Parameters of the M3 Connections Model (a),
and Experimental and Analytical M3 Model of Connection Moment-rotation Relationship (b)

(a) (b)

Figure 18. C1 Frame: Global View (a) and Local Buckling of the Left Beam Connection (b)

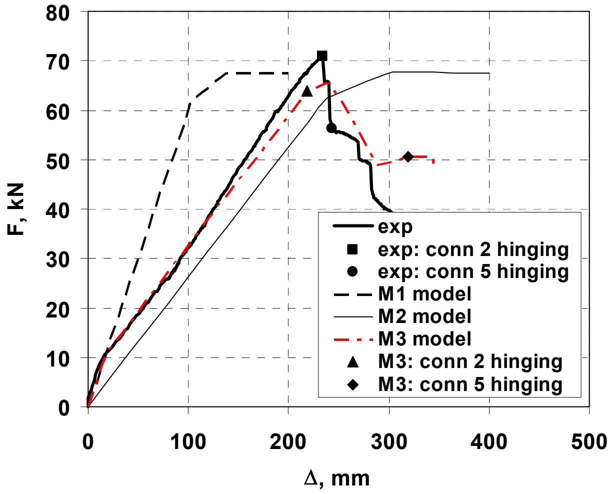

Figure 19. Frame C1: Experimental vs. Numerical Lateral Force - Deformation Curves

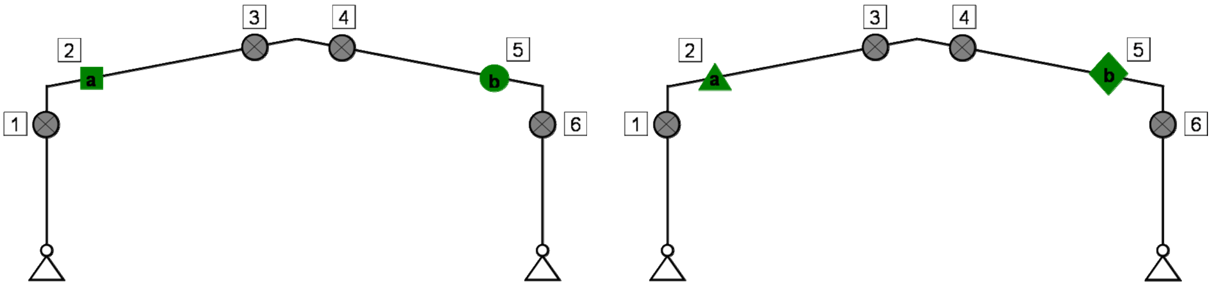

(a) (b)

Figure 20. Frame C1: Position of Local Buckling Observed Experimentally (b) and in the Numerical Model (c)

In the case of the C2 frame, gravity loading corresponding to seismic design situation was first applied, followed by increasing lateral loading up to complete failure of the frame. Figure 21a shows a view of the frame during loading. The global force-deformation response was very similar to the frame C1 up to 10-15 kN lateral loading. For larger lateral loading, the stiffness of the C2 frame was slightly larger than the one of the C1 frame. However, the global resistance under horizontal loading was smaller in the case of the C2 frame. The ultimate capacity was attained at the first local buckle in the beam near the right eaves (connection 5, see Figure 23a), when the lateral force resistance dropped suddenly. It was followed by a combined local buckling and lateral-torsional buckling of one of the columns at the mid-height (see Figure 21a and Figure 23a). Finally, local buckling of the beam at the left eaves was observed (at connection 2, see Figure 23a).

A comparison of the experimental and numerical lateral force – deformation response of the C2 frame is shown in Figure 22. As in the case of frame C1, The M1 model (with rigid connections) provides a good approximation of the initial response of the frame, up to lateral forces of about 10 kN. For larger forces, the M2 model, accounting for semi-rigid connection response, shows a better approximation of experimental response. The M3 model shows the best agreement between the numerical and experimental results. All numerical models overestimate the global frame resistance under lateral loading. There are two factors that are believed to have contributed to this situation: (1) the numerical model did not consider buckling of the column and (2) the influence of axial forces was neglected when determining connection moment resistance. Higher axial forces are present in the right column under combined effect of gravity loading and lateral loading due to the effect of overturning. While the location of the first local buckle was correctly predicted by the numerical model (at connection 5, see Figure 23a and Figure 22b), column hinging (due to combined local and flexural-torsional buckling) observed in the experimental test was not confirmed by numerical models. Column hinging can be explained by neglected influence of axial force, combined with the effect of no lateral restraining at column flanges by side rails. Both of these effects were present in the experimental setup, but not in the numerical model.

(a) (b)

Figure 21. C2 Frame: Global View (a) and Local Buckling of the Right Beam Connection (b)

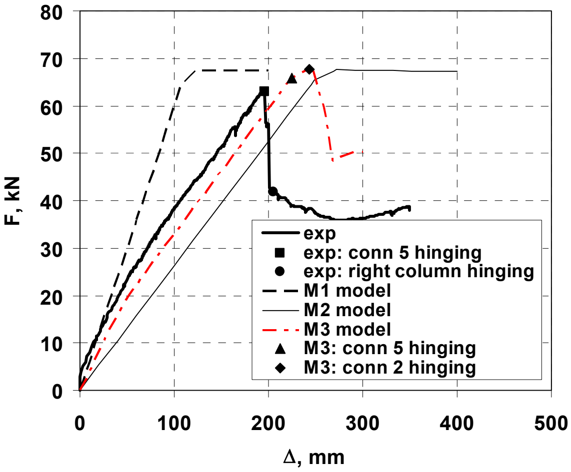

Figure 22. Frame C2: Comparison of Experimental and Numerical Lateral Force – Deformation Curves

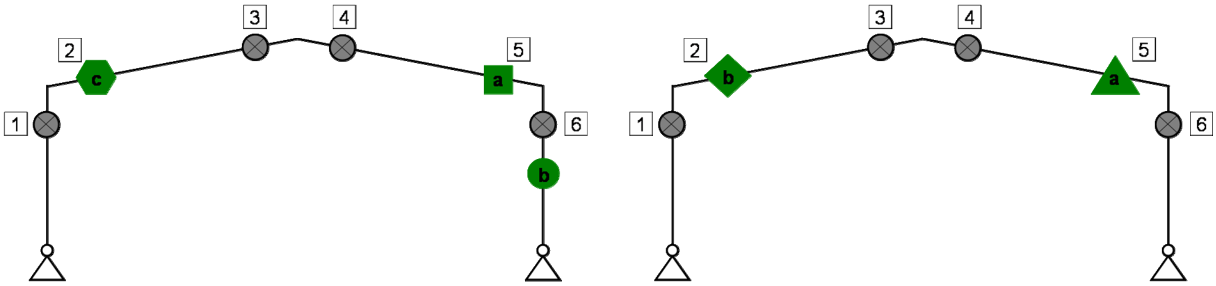

(a) (b)

Figure 23. Frame C2: Position of Local Buckling Observed Experimentally (b) and in the Numerical Model (c)

It can be concluded that the M3 model seems to provide the best agreement with the experimental results, if initial stiffness, lateral resistance, and post-buckling response are envisaged. The global frame resistance under lateral loads drops quickly after the first local buckling, when the maximum force is reached. This behaviour is attributed to the similar rapid drop in moment resistance of cold-formed cross-sections, as well as to the low redundancy of the frame. Therefore, for practical cases, the response to the first local buckle in members is important, which can be estimated using a simpler frame model, incorporating only the semi-rigid connection response, eventually an elastic perfectly plastic model. The Global frame stiffness determined using the bilinear moment-rotation characteristics obtained analytically by the component method is smaller than the experimental stiffness. The real initial stiffness of the connection may be higher at low moments, due to restraining provided by flanges of the bracket element and/or by the inner bolt group. The M3 connection model is capable of representing this higher stiffness and provides the closest match between experimental and numerical frame stiffness values.

5. CONCLUSIONS

This study suggests that the classical calculation model for connections, assuming the centre of rotation to be located at the centroid of the bolt group and a linear distribution of the forces on each bolt, is inappropriate for frames featuring cold-formed members. The force distribution is unequal due to the flexibility of the connected members. In fact, the force is an order of magnitude bigger in the outer bolt rows compared to most inner ones. A connection with bolts only on the web causes concentrated forces in the web of the connected member and leads to premature web buckling, reducing the joint moment capacity. These type of connections are always partial strength. If the load bearing capacity of the connected beam is to be matched by the connection strength, bolts on the flanges become necessary. The ductility of the connection is reduced both under monotonic and cyclic loads and the design, including the design for earthquake loads, should take into account only the conventional elastic capacity. Because there is no significant post-elastic strength, there are no significant differences in ductility and capacity of cyclically tested specimens compared with the monotonic ones.

The application of the component method implemented in EN1993-1-8 for determination of connection characteristics in the case of cold-formed members is possible with a minimum number of adjustments. For the particular case of connection studied in this paper (with both flange and web bolts), connection characteristics can be determined with a reasonable accuracy if only the outer bolt group of bolts is considered. The components contributing to the stiffness and strength of the connection are: cold-formed member flange and web in compression, bolts in shear, bolts in bearing on the cold-formed member, and bolts in bearing on the bracket. It is considered appropriate to use a linear distribution of forces on bolts in the case of a connection to light-gauge members.

The connection with both flange and web bolts is semi-rigid but full-strength. Therefore the design of light-gauge portal frames with the considered type of connection needs to account for connection flexibility. Connection characteristics obtained using the component method (EN1993-1-8) can be easily incorporated in the structural model, in order to obtain a realistic response under lateral forces. A connection model is developed that captures well both the behaviour in the elastic range and in the post-elastic range.

Though a detailed moment-rotation response representing the initial stiffness, moment resistance and post-buckling response provides the most realistic global response, a simple elastic structural analysis modelling connection stiffness alone can be sufficient for design purpose. Cold-formed steel pitched-roof portal frames of back-to-back channel sections and bolted joints are characterised by a rapid degradation of strength after the first local buckling in its members. This behaviour is attributed to the similar rapid drop in moment resistance of cold-formed cross-sections, as well as to the low redundancy of the frame analysed in this study. Therefore, for the considered frame configuration, global strength may be estimated at the attainment of the moment capacity in the most stressed cross-section using an elastic structural analysis. Axial forces can reduce moment resistance of cold-formed members and need to be taken into account.

REFERENCES

[1] Lim, J.B.P. and Nethercot, D.A., "Stiffness Prediction for Bolted Moment-connections between Cold-formed Steel Members", Journal of Constr. Steel Res., 2004, Vol. 60, Issue 1, pp. 85-107.

[2] Chung, K.F. and Lau, L., "Experimental Investigation on Bolted Moment Connections Among Cold Formed Steel Members", Engineering Structures, 1999, Vol. 21, No. 10, pp. 898-911.

[3] Lim, J.B.P. and Nethercot, D.A., "Ultimate Strength of Bolted Moment-connections between Cold-formed Members", Thin-Walled Structures, 2003, Vol. 41, No. 11, pp. 1019-1039.

[4] Dundu, M., Kemp, A.R., "Strength Requirements of Single Cold Formed Channels Connected Back-to-back", Journal of Constructional Steel Research, 2006, Vol. 62, Issue 3, pp. 250-261.

[5] Yu, W.K., Chung, K.F. and Wong, M.F., "Analysis of Bolted Moment Connections in Cold-formed Steel Beam–column Sub-frames", Journal of Constructional Steel Research, 2005, Vol. 61, Issue 9, pp. 1332-1352.

[6] Lim, J.B.P., "Joint Effects in Cold-formed Steel Portal Frames", University of Nottingham, Ph.D. Thesis, 2001.

[7] Kwon, Y.B., Chung, H.S., and Kim, G.D., "Experiments of Cold-formed Steel Connections and Portal Frames", Journal of Structural Engineering, 2006, Vol. 132, No. 4, pp. 600-607.

[8] Dubina, D., Stratan, A., Ciutina, A., Fulop, L., Nagy, Zs., "Performance of Ridge and Eaves Joints in Cold-formed Steel Portal Frames", Proc. of the 17th int. Specialty Conf., Orlando, Florida, USA, 04-05 Nov. 2004, Univ. of Missouri-Rolla, Ed. R.A. LaBoube, W-W. Yu, pp. 727-742.

[9] EN1993-1-8, "Eurocode 3: Design of Steel Structures - Part 1-8: Design of joints", European Committee for standardization, 2003.

[10] EN 1993-1-3, "Eurocode 3: Design of Steel Structures. Part 1-3: General Rules. Supplementary Rules for Cold-formed Thin Gauge Members and Sheeting", European Committee for Standardization, 2001.

[11] ECCS(1985), "Recommended Testing Procedure for Assessing the Behaviour of Structural Steel Elements under Cyclic Loads", European Convention for Constructional Steelwork, TWG 13 Seismic Design, Report No. 45, 1985

[12] Jaspart, J.P., Steenhuis, M., Anderson, D., "Characterisation of the Joint Properties by Means of the Component Method", Control of Semi-rigid Behaviour of Civil Engineering Structural Connections, COST C1, Proc. of the Int. Conf, Liege, 17-19 September 1998.

GBT AND cFSM: TWO MODAL APPROACHES TO THE BUCKLING ANALYSIS OF UNBRANCHED THIN-WALLED MEMBERS

S. Ádány[1*], N. Silvestre[2], B.W. Schafer[3] and D. Camotim[2]

[1]*Department of Structural Mechanics, Budapest University of Technology and Economics,*
1111 Budapest, Műegyetem rkp. 3, Hungary
[2]*Department of Civil Engineering and Architecture, Technical University of Lisbon, ICIST/IST,*
Av. Rovisco Pais, 1049 Lisboa, Portugal
[3]*Department of Civil Engineering, Johns Hopkins University, Latrobe Hall 210, Baltimore, MD 21218, USA*
**(Corresponding author: E-mail: sadany@epito.bme.hu)*

ABSTRACT: The objective of this paper is to provide (i) the fundamental derivation details and (ii) a comparison between Generalised Beam Theory (GBT) and the constrained Finite Strip Method (cFSM), two alternative modal approaches to analyse the elastic buckling behaviour of unbranched thin-walled members. Thin-walled members may generally buckle in three families (or types) of modes: global, distortional and local (or local-plate) modes. The distinguishing feature of the GBT and cFSM methodologies to obtain buckling solutions is that they can formally separate these three types of buckling modes. An overall comparison of the two methods is provided, including practical aspects, such as the different notations, and theoretical points related to how the displacement fields are either constructed or decomposed into deformation modes akin to the above families. Specific derivation details are provided for both GBT and cFSM, along with numerical examples concerning the buckling behaviour of cold-formed steel lipped channel members under compression and bending. The numerical examples (i) show the power of both GBT and cFSM to separate general stability solutions into pure solutions related to the buckling mode types, (ii) illustrate the use of the identified deformation fields to examine the modal contributions to a buckling solution, and (iii) demonstrate that, in spite of their quite distinct developments, GBT and cFSM modal approaches provide essentially the same extended capabilities for examining and understanding thin-walled member stability. Moreover, considerable attention is also paid to the different handling of the membrane deformations by the two methods, which is responsible for the minor (but fully explainable) discrepancies existing between the results yielded by the two methods.

Keywords: Thin-walled members, buckling analysis, generalised beam theory (GBT), constrained finite strip method (cFSM), deformation modes, local buckling, distortional buckling, global buckling

1. INTRODUCTION

Since the load-carrying capacity of thin-walled members is often governed by buckling phenomena, the ability to calculate the corresponding elastic critical loads/moments is of paramount importance. However, the member ultimate load is very seldom close to its elastic critical load, due to (i) the physical non-linearity (plasticity effects), (ii) the presence of material and geometrical imperfections and (iii) the possible existence of a more or less pronounced post-buckling strength reserve. While physical non-linearity is associated primarily with the material constitutive behaviour, the imperfection-sensitivity and post-buckling strength reserve are tied to the nature of the buckling phenomenon (mode). This explains why the correct identification and classification of the buckling modes, as well as the accurate calculation of the corresponding critical loads, have chief importance in determining the ultimate load-carrying capacity of a thin-walled member.

Usually, three main families of buckling phenomena (modes) are encountered in practice: (i) global buckling, in which the member axis deforms (*e.g.*, flexural or lateral-torsional buckling), (ii) local-plate buckling, involving only plate (wall) bending, and (iii) distortional buckling, combining wall bending with cross-section distortion – the last two phenomena are sometimes jointly described as “local buckling”. Although there exist several numerical and/or analytical methods to determine critical load/moment values and the corresponding buckling mode shapes, it is fair to say that only generalised beam theory

(GBT – *e.g.*, [1-3]) and the constrained finite strip method (cFSM – [4-6]) are able to perform this task for selected isolated ("pure") or arbitrarily combined ("coupled") modes.

For more than a decade, GBT has been the only approach possessing the modal features described above, which are specially useful to solve many problems of practical interest and, in particular, to provide in-depth understanding about several mechanical aspects of the member buckling behaviour. However, a novel modal approach has been recently developed and reported, namely the constrained finite strip method. Although the two approaches lead to very similar solutions, GBT and cFSM have quite different roots: while GBT is an extension of the classical thin-walled beam theory, the cFSM has its origins in the folded-plate theory underlying the semi-analytical finite strip method. Indeed, it may be said that (i) GBT is the generalisation of the classical beam theory, by considering additional degrees of freedom to allow for the cross-section in-plane deformations, whilst (ii) cFSM is a specialisation of the classical folded-plate theory that carefully selects constraints to force the member to deform (buckle) according to pre-defined patterns.

For about a year and a half the authors have been working on providing an in-depth comparison of the fundamentals of the two above modal approaches (GBT and cFSM), namely by addressing (i) their basic mechanical assumptions, (ii) the distinct procedures they employ, (iii) their domains of application and limitations, and also (iv) the numerical results provided by each of them [7-9] – therefore, the objective of this paper is to report in detail the outcome of the first phase of this ongoing research project. Initially, a general comparison is presented in section 2, which includes several practical aspects, such as the different notations, and theoretical points related to how the displacement fields are either constructed or decomposed into deformation modes akin to the three buckling mode families. Then, sections 3 and 4 are devoted to the presentation of the GBT and cFSM procedures to obtain the cross-section deformation modes. However, due to space limitations, the presentations are necessarily brief and cannot cover all the details – they rather focus on the main steps of the derivations and on the most important formulae involved (the interested reader can find more detailed information in the references). Next, illustrative numerical results concerning the buckling behaviour of lipped channel columns and beams are compared in section 5: the analyses are performed by means of the two approaches and the calculated critical loads and moments, together with the corresponding buckling mode participation factors, are presented and discussed. In particular, considerable attention is paid to the different handling of the membrane deformations, which is responsible for the minor (but fully explainable) discrepancies existing between the results yielded by the two methods – particularly the ones associated with column flexural buckling. Finally, the paper closes with some conclusions drawn from the comparison of the two modal approaches to analyse the buckling behaviour of unbranched open thin-walled members.

The authors hope that the comparison presented here will contribute to provide a better understanding of the two methodologies and also of the phenomena that they aim to uncover, thus paving the way to the development of more efficient tools for the analysis and design of thin-walled members, namely cold-formed steel columns, beams and beam-columns.

2. GENERAL COMPARISON BETWEEN GBT AND CFSM

2.1 Notation and Terminology

Consider the thin-walled member shown in Figure 1, which displays an arbitrary unbranched open cross-section formed by several walls (plate elements). The most important notation and terminology adopted by GBT and cFSM buckling analysis are summarised and compared in Table 1 – since the differences are not negligible, the interested reader is advised to pay attention to them, so that he can fully grasp the similarities and differences between the main concepts and procedures involved in the two approaches, as well understand the buckling results yielded by either of them.

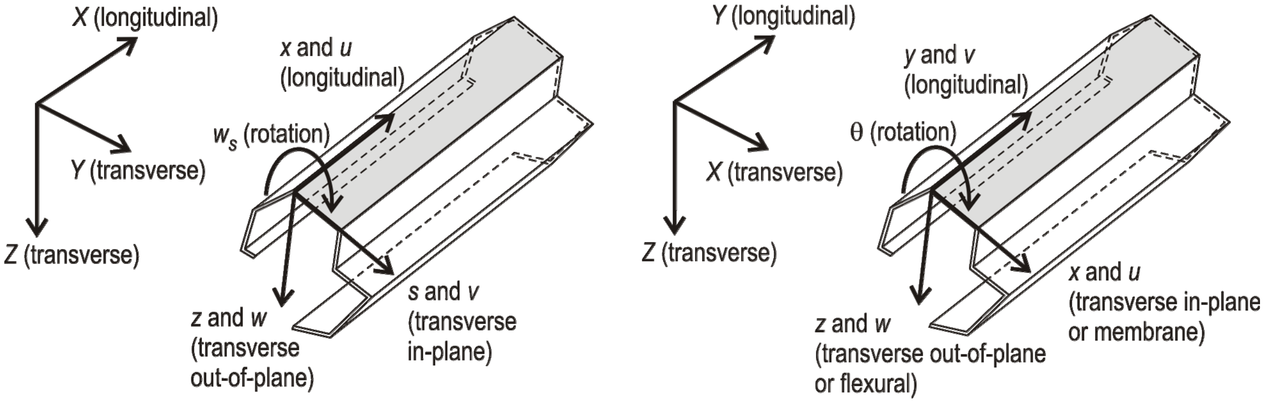

(a) GBT (b) cFSM

Figure 1. Thin-walled Member with Arbitrary Unbranched Open Cross-section: (a) GBT and (b) cFSM Coordinate Axis and Degree of Freedom Notations

Table 1. Comparisons between the Notation and Terminology Adopted by GBT and cFSM

	Description	**GBT**	**cFSM**
Displacements	longitudinal, transverse in-plane, transverse out-of-plane, rotation	u, v, w, $w_{,s}$	v ,u, w, θ
Local coordinates	longitudinal, in-plane, out-of-plane	x, s, z	y, x, z
Global coordinates	longitudinal, transverse	X and Y, Z	Y and X, Z
Member	Length	L	a
	wall (plate) width	b	b
Nodes, DOF	node at wall ends	natural node	main node
	node within walls	intermediate node	sub-node
	number of walls	n	n_{main}-1
	intermediate/sub-node number	m	n_{sub}
	total number of DOF	$n+m+1$	$m = 4\times(n_{main}+n_{sub})$
Deformation modes	Global	rigid-body, global, G	global, G
	Distortional	distortional, D	distortional, D
	local plate	local-plate, LP	local, L
	Shear	shear, S	other, O
	transverse extension	shear, TE	other, O

2.2 Comparison at a Glance

Table 2 provides a schematic general overview of the essential features characterising the GBT and cFSM approaches, making it possible to draw some conclusions compare them and draw some conclusions about their similarities and differences. First of all, it is worth pointing out that, although they originate from different theories and exhibit quite distinct evolutions, the two methods handle the buckling analysis of thin-walled members in manners that exhibit many common traits. The most important similarity is the fact that both (i) begin by performing a *nodal* discretisation of the cross-section (*nodal* degrees of freedom) and (ii) end up reaching (defining) a set of cross-section deformation modes (*modal* degrees of freedom). Conversely, the most important differences are related to (i) the longitudinal discretisation, (ii) the transformation to the modal basis and (iii) the concepts and procedures involved in the derivation and application of the two methods – some of these differences are discussed further ahead, in subsection 2.3.

Table 2. Comparison between the Essential Features of GBT and cFSM

Basis	GBT	cFSM
Origin	beam theory	folded-plate theory
Development of the method	enrichment of beam theory by adding additional deformation possibilities	decomposition of the general finite strip method deformation space
Two-step analysis	yes, first cross-section analysis, then member analysis	yes, first modal decomposition, then member analysis
Cross-section properties	calculation of modal cross-section properties, then the member treated as a bar	no cross-section properties are necessary, all the calculation is based on the strips
Orthogonal modes	important, not indispensable	possible, not crucial
Orthogonalisation	auxiliary eigenvalue problems in the cross-section (infinitesimal member element)	eigenvalue problem in member (longitudinal distribution is sin/cos)
Considered deformation modes	global, distortional, local-plate, shear, transverse extension	global, distortional, local, other
Base system for solution	always modal	can be modal or nodal
Cross-section discretisation	yes	yes
Distinction between main nodes and sub-nodes	yes	yes
DOF per node	u,v,w for natural nodes w for intermediate nodes	u,v,w,θ for all nodes – but any DOF can be switched off
Longitudinal discretisation	yes (if necessary)	never, due to FSM rational
Longitudinal displacement variation	no discretisation: sine-cosine discretisation: Hermite cubic polynomials	sine-cosine (in theory, it can be different – not yet worked out for cFSM)

As far as longitudinal discretisation is concerned, GBT allows for the application of the finite element method (beam elements adopting Hermite cubic polynomials for the longitudinal discretisation) or other numerical techniques, such as the finite difference, Rayleigh-Ritz or Galerkin methods – this possibility is particularly relevant if the member is not simply supported. However, for simply supported members (end sections locally/globally pinned and free to warp), trigonometric (sinusoidal) shape functions provide exact solutions for the problem and longitudinal discretisation can be avoided without sacrificing accuracy. In the case of cFSM, which retains the essence of finite strip analysis, longitudinal discretisation is never considered – recall that this is the key feature differentiating the FSM from the FEM (shell elements). Although the FSM has been implemented with various longitudinal shape functions, the cFSM uses only trigonometric (sinusoidal) longitudinal shape functions. Table 3 summarises how the different ways of handling the longitudinal shape functions affect the domains of application of the two methods.

Table 3. Comparison between the Domains of Application of GBT and cFSM

Applicability	GBT	cFSM
End restraint conditions	various: pinned, fixed, free, restrained/free warping	hinged and free to warp
Cross-section change along length	not allowed	not allowed
Tapered members	not	not
Intermediate supports along length	yes	yes, but only continuous

Another important difference between GBT and cFSM concerns the base systems adopted. cFSM begins by using mechanical assumptions to define sub-spaces for the various deformation mode families (G, D, L and O). Among the various cFSM base systems, it is possible to introduce a GBT-like one (see subsection 4.10), which can be determined by solving eigenvalue problems within the various sub-spaces – however, it should be emphasised that the calculation of pure buckling modes does not require any special base system in cFSM (the only important issue is the determination of the sub-spaces). Finally, note that, as far as the application of the cFSM is concerned, the adoption of the GBT-like base vectors does not entail any computational advantage.

In GBT, the determination of special (orthogonal) base vectors is fundamentally similar to the one employed by the cFSM and requires the solution of a sequence of auxiliary eigenvalue problems, defined for a cross-section (*i.e.*, a member element with an infinitesimal length *dx*) – in the cFSM, on the other hand, a "unit-length" member is analysed. Moreover, the existence of an orthogonal base system plays an important practical role in GBT, as the corresponding special base vectors are always associated with significant computational advantages (strong reduction of the number of degrees of freedom involved in the analyses).

2.3 Concepts and Procedures Adopted in the Derivations

Figure 2 provides flowcharts that briefly describe most of the concepts and (mostly) procedures involved in determining the deformation modes by means of GBT or the cFSM. Great emphasis is placed on the procedures adopted by these two methods to handle the various deformation mode families: (i) while GBT adds progressively more displacement degrees of freedom (d.o.f.) to the classical beam theory ones, (ii) the cFSM constrains the classical finite strip displacement degrees of freedom (d.o.f.). As it will be illustrated later, the numbers of displacement d.o.f. associated with the application of the two methods can be practically identical, even if they approach the thin-walled member analysis in fundamentally different ways. It is important to mention that figure 2 shows clearly that GBT gradually enhances of the deformation mode set, a sequential procedure that also reflects the historical evolution of the method – as for the cFSM, the sequential procedure displayed includes the steps that had to necessarily be followed to derive the method.

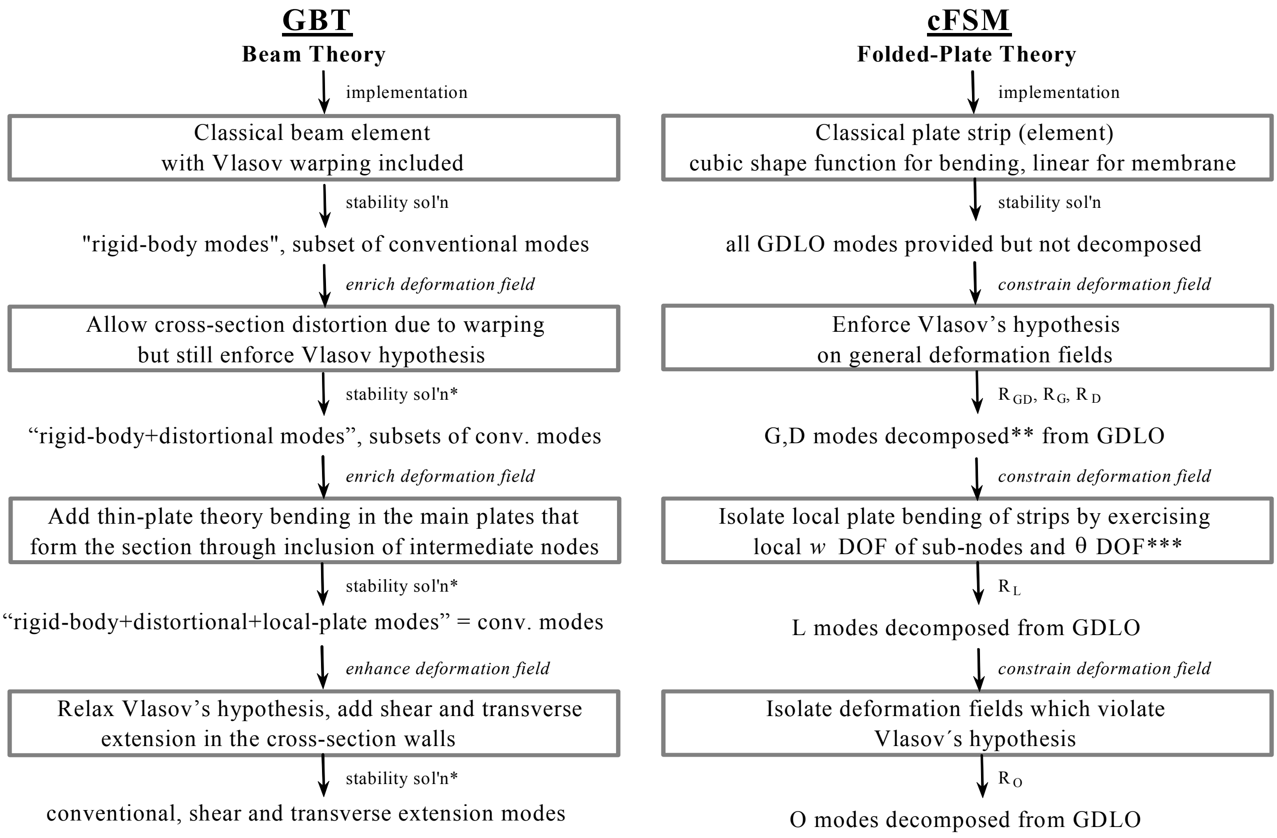

*before performing buckling analysis, auxiliary eigenvalue problems are solved to place the new deformations in a modal (cross-section) basis.

** separation of G and D from one another requires enforcing beam theory and considering the "rigid-body" constraint of D modes
*** Vlasov hypothesis is maintained

Figure 2. Flowcharts Concerning the Determination of the Deformation Mode by Means of GBT and cFSM

3. OVERVIEW OF GBT

First of all, it must be said that most of the unique features associated to the application of GBT stem from its cross-section analysis procedure, which has been described in detail in [1, 10] and leads to the identification of several (orthogonal) cross-section *deformation modes*: axial extension, major/minor axis bending, torsion, distortional and local-plate (transverse bending) modes. In order to provide a quick and concise overview of the most important concepts and procedures involved in the performance of a cross-section analysis, its application to the lipped channel section depicted in Figure 3 is briefly described and commented.

3.1 Cross-Section Analysis

A cross-section comprising n walls must be discretised into (i) $n+1$ natural nodes (wall ends) and (ii) m intermediate nodes, where it should be noted that the cross-section (free) end nodes are treated as *both* natural and intermediate, *i.e.*, are associated with a warping function *and* a local flexural function, thus making it possible to account for the flexural deformation of the end walls. (While the natural nodes are indispensable to perform a GBT analysis, the incorporation of intermediate nodes is necessary whenever the flexural deformation of the cross-section walls is relevant (mostly in local-plate buckling)). Figure 3 shows a possible discretisation of a lipped channel section that involves *6* natural nodes (mandatory) and *7* intermediate nodes (optional).

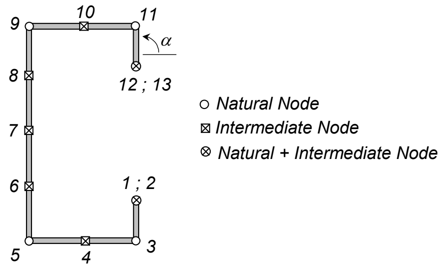

Figure 3. GBT Discretisation of a Lipped Channel Cross-Section.

In order to obtain the cross-section displacement field components (*i.e.*, functions $u(s)$, $v(s)$ and $w(s)$), one must begin by imposing (i) unit warping displacements at the natural nodes ($\overline{u}_k = 1,\ k=1,\ \ldots,\ n+1$) and (ii) unit flexural displacements at the intermediate nodes ($\overline{w}_k = 1,\ k=n+2,\ \ldots,\ n+m+1$), a procedure leading to the identification of $n+1$ "elementary warping functions" $\overline{u}_k\,(s)$ and m "elementary local flexural functions" $\overline{w}_k\,(s)$, all varying linearly between consecutive nodes – Figure 4 displays the functions $\overline{u}_k\,(s)$ and $\overline{w}_k\,(s)$ associated with the lipped channel discretisation shown in Figure 3.

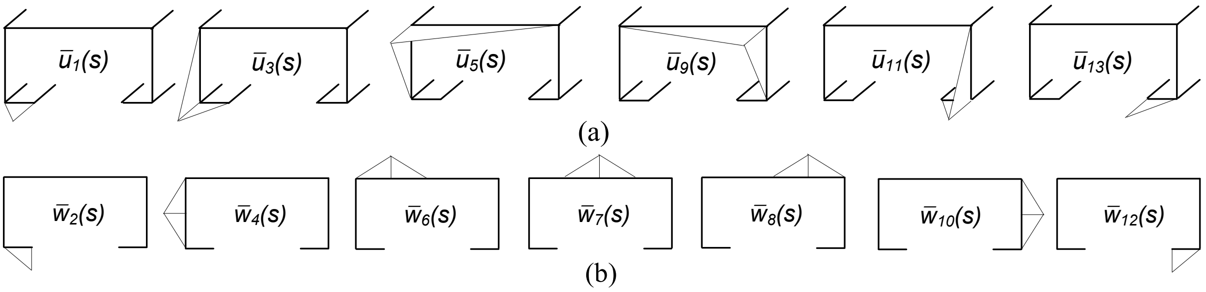

Figure 4. Lipped Channel Section Elementary (a) Warping ($\overline{u}_k\,(s)$) and (b) Local Flexural ($\overline{w}_k\,(s)$) Functions

In order to comply with Vlasov's assumption of null membrane shear strains along the cross-section mid-line, when a unit warping displacement is imposed at node k (function $u_k(s)$) each wall adjacent to that node is forced to move laterally, thus exhibiting membrane displacements v given by

$$\gamma_{xs} = u_{,s} + v_{,x} = 0 \qquad \Rightarrow \qquad \mathrm{dv} = -\frac{du}{ds}dx \tag{1}$$

Note that the elementary flexural functions $w_k(s)$ automatically satisfy Vlasov's assumption (since $u=v=0$). To ensure nodal compatibility between the transverse membrane (v) and flexural (w) displacements, the cross-section is "forced" to deform in its own plane due to the application of the "elementary warping functions" $\overline{u}_k\,(s)$. This is illustrated in Figure 5, where one sketches the membrane (v) and flexural (w) displacements associated with the $\overline{u}_k\,(s)$ and $\overline{w}_k\,(s)$ corresponding to a half (symmetric) lipped channel section.

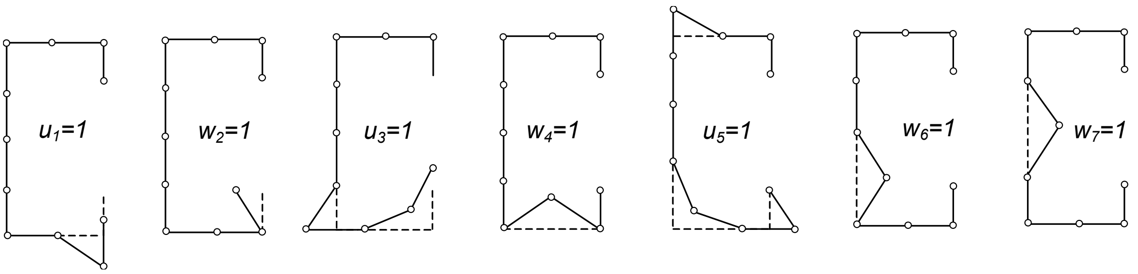

Figure 5. Deformed Configuration of the Cross-Section Walls after Imposing Unit Warping and Flexural Functions.

Imposing the wall membrane (v) and flexural (w) displacements leads to relative rotations between adjacent walls that violate the node compatibility, thus requiring the determination of nodal transverse bending moments that ensure rotation compatibility at the various nodes – this involves the solution of a statically indeterminate folded-plate problem, a task performed by means of the force method. (This could also be done by means of the displacement method. In the case of unbranched open cross-sections, both methods involve approximately the same amount of calculations.) When both equilibrium and compatibility are satisfied, one obtains the cross-section displacement field, characterised by (i) linear $u_k(s)$, constant $v_k(s)$ and cubic $w_k(s)$, in the case of $\overline{u}_k(s)$, and by (ii) null $u_k(s)$, null $v_k(s)$ and cubic $w_k(s)$, in the case of $\overline{w}_k(s)$. Then, the GBT equilibrium equation system is written in a vector space defined by a mixed coordinate system ($u_r(s)$ and $w_t(s)$): $y_k(s)$, with $k=1, ..., n+m+1$). For the discretisation shown in Figure 3, the mixed vector **y** of dimension $n+m+1$ reads

$$\mathbf{y} = \{u_1\ w_2\ u_3\ w_4\ u_5\ w_6\ w_7\ w_8\ u_9\ w_{10}\ u_{11}\ w_{12}\ u_{13}\}^{\mathrm{T}} \tag{2}$$

The displacement fields obtained through the imposition of the various elementary functions are grouped in matrices **U**, **V** and **W** (dimension $p\times(n+m+1)$, where p is the number of cross-section wall segments). The cross-section displacement field may then be expressed as

$$\mathbf{u} = \mathbf{U}\,\phi_{,x} \qquad \mathbf{v} = \mathbf{V}\,\phi \qquad \mathbf{w} = \mathbf{W}\,\phi \tag{3}$$

a representation compatible with the classical beam theory, where (i) **u**, **v** and **w** are column-vectors containing the member displacement fields ($u(x,s)$, $v(x,s)$ and $w(x,s)$), (ii) $(\cdot)_{,x}\equiv\partial(\cdot)/\partial x$, (iii) **U**, **V** and **W** are matrices containing the cross-section displacement profiles ($u_k(s)$, $v_k(s)$ and $w_k(s)$) in each row, and (iv) ϕ is a column-vector whose components are modal amplitude functions ($\phi_k(x)$), defined along the member length ($0 \leq x \leq L$).

The GBT equilibrium equations, written in the matrix form, are given by

$$\mathbf{C}\phi_{,xxxx} - \mathbf{D}\phi_{,xx} + \mathbf{B}\phi - \lambda W_m^o \mathbf{X}_m \phi_{,xx} = \mathbf{0} \tag{4}$$

where W_m^o are generalised pre-buckling stress resultants (known *a priori*), λ (load parameter) is the problem eigenvalue and the matrices appearing in system (4) read

$$\mathbf{C}=E\int_0^b[t\,\mathbf{U}^{\mathrm{T}}\mathbf{U}+\tfrac{t^3}{12}\mathbf{W}^{\mathrm{T}}\mathbf{W}]\,ds$$

$$\mathbf{D}=G\int_0^b[\tfrac{t^3}{3}(\mathbf{W}_{,\mathrm{s}}^{\mathrm{T}}\mathbf{W}_{,\mathrm{s}})-\tfrac{\nu}{2(1-\nu)}(\mathbf{W}_{,\mathrm{ss}}^{\mathrm{T}}\mathbf{W}+\mathbf{W}^{\mathrm{T}}\mathbf{W}_{,\mathrm{ss}})]\,ds$$

$$\mathbf{B}=\frac{E}{12(1-\nu^2)}\int_0^b t^3\,\mathbf{W}_{,\mathrm{ss}}^{\mathrm{T}}\mathbf{W}_{,\mathrm{ss}}\,ds \qquad \mathbf{X}_m=\int_0^b\tfrac{Et}{\mathbf{C}_m}(\mathbf{V}^{\mathrm{T}}\mathbf{U}_m^o\mathbf{V}+\mathbf{W}^{\mathrm{T}}\mathbf{U}_m^o\mathbf{W})ds \tag{5}$$

Once the displacement field components (**U**, **V** and **W**) are known, it is possible to calculate the matrices **C**, **D**, **B** and **X** appearing in system (4), which constitutes a straightforward (but time/effort consuming) task. Moreover, it should be mentioned that all the above four matrices are *fully populated*, which means that system (4) is *highly* coupled, a fact that considerably complicates its solution and, more important than that, the interpretation of the results obtained. Indeed, the physical meaning of the various matrix components is far from obvious, even in the case of rather trivial and well-known phenomena (*e.g.*, bending). In order to take full advantage of all the GBT potential, mostly concerning the clarity and physical interpretation of the results, the above matrices must be rendered “as simple as possible”, a goal achieved through the simultaneous diagonalisation of matrices **C** and **B**.

3.2 Determination of the Local-Plate and Distortional Modes

Consider the eigenvalue problem

$$(\mathbf{B}-\lambda_k\mathbf{C})\,\mathbf{y}_k=\mathbf{0} \tag{6}$$

which has $n+m+1$ eigenvalues λ_k – the first *four* are *null*. The following remarks are appropriate:

(i) $\lambda_k=0$ ($k=1,\dots,4$) correspond to the vector space defined by *4* eigenvectors $\dot{\mathbf{y}}_k$ associated with cross-section *rigid-body* motions – axial extension, major and minor axis bending and torsion.

(ii) $\lambda_k>0$ ($k=5,\dots,n+1$) correspond to $n-3$ eigenvectors $\dot{\mathbf{y}}_k$ associated with cross-section in-plane *deformation*, characterised by warping and fold-line motions – *distortional modes*.

(iii) $\lambda_k>0$ ($k=n+2,\dots,n+m+1$) correspond to m eigenvectors $\dot{\mathbf{y}}_k$ associated with cross-section in-plane *deformation* without warping and fold-line motions – *local-plate modes*.

For illustration purposes, consider the cross-section discretisation shown in Figure 3, which leads to the identification of *13* (conventional) deformation modes – Figures 6(a)-(b) show the in-plane deformed configurations and warping displacement profiles of *2* ($\equiv n$-3) *distortional* modes. Figure 7, on the other hand, displays the in-plane deformed configurations of the *7 local-plate* modes ($7\equiv m$) – note that they involve no fold-line motions (natural node displacements).

(a) (b)

Figure 6. Lipped Channel Distortional Modes: (a) In-Plane Configurations and (b) Warping Profiles

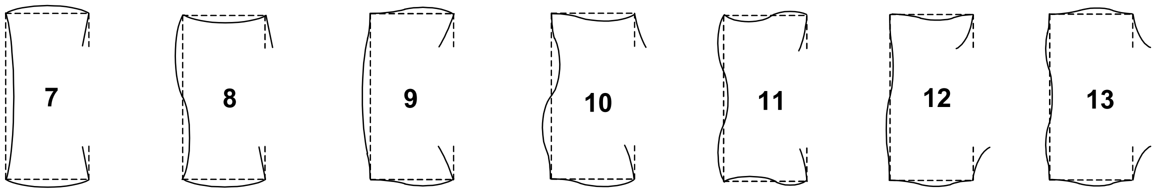

Figure 7. Lipped Channel Local-Plate Modes: In-Plane Deformed Configurations

Because one has $\lambda_k=0$ ($k=1,...,4$), any vector obtained through a linear combination of $\dot{\mathbf{y}}_1$, $\dot{\mathbf{y}}_2$, $\dot{\mathbf{y}}_3$ and $\dot{\mathbf{y}}_4$ is also an eigenvector of system (6). To obtain the *four rigid-body* deformation modes, one considers the sub-matrix $\dot{\mathbf{Y}}_\mathbf{I}$ (formed by the first four eigenvectors of (6)) and the transformed matrices $\dot{\mathbf{C}}$ and $\dot{\mathbf{D}}$, defined by

$$\dot{\mathbf{Y}}_\mathbf{I} = [\dot{\mathbf{y}}_1 \quad \dot{\mathbf{y}}_2 \quad \dot{\mathbf{y}}_3 \quad \dot{\mathbf{y}}_4] \qquad \dot{\mathbf{C}} = \dot{\mathbf{Y}}_\mathbf{I}^\mathrm{T}\,\mathbf{C}\,\dot{\mathbf{Y}}_\mathbf{I} \qquad \dot{\mathbf{D}} = \dot{\mathbf{Y}}_\mathbf{I}^\mathrm{T}\,\mathbf{D}\,\dot{\mathbf{Y}}_\mathbf{I} \qquad (7)$$

3.3 Determination of the Torsion Mode

Consider the eigenvalue problem ($\dot{\mathbf{C}}$ and $\dot{\mathbf{D}}$ are the transformed matrices in (7))

$$(\dot{\mathbf{D}} - \lambda_k \dot{\mathbf{C}})\,\mathbf{y}_k = \mathbf{0} \qquad (8)$$

which has *4* eigenvalues λ_k – the first *three* are *null*:

$\lambda_k=0$ ($k=1,...,3$) correspond to a vector space defined by *3* eigenvectors $\dot{\mathbf{y}}_k$ associated with cross-section *rigid-body* motions having *no twisting* rotation – extension, major/minor axis bending.

(ii) $\lambda_4>0$ corresponds to *one* eigenvector $\dot{\mathbf{y}}_4$ associated with a cross-section *rigid-body* motion *with twisting* rotation – *torsion mode*. Figure 8 shows the in-plane deformed configuration and warping displacement profile of this mode.

(a) (b)

Figure 8. Lipped Channel Torsion Mode: (a) In-Plane Configuration and (b) Warping Profile

Then, one determines matrix (of dimension $(n+m+1)\times 4$)

$$\ddot{\mathbf{Y}} = \dot{\mathbf{Y}}_{\mathbf{I}}\,\mathbf{Y} = \dot{\mathbf{Y}}_{\mathbf{I}}\,[\mathbf{y}_1 \quad \mathbf{y}_2 \quad \mathbf{y}_3 \quad \mathbf{y}_4] = [\ddot{\mathbf{y}}_1 \quad \ddot{\mathbf{y}}_2 \quad \ddot{\mathbf{y}}_3 \quad \ddot{\mathbf{y}}_4] \tag{9}$$

which stems from the product between $\dot{\mathbf{Y}}_{\mathbf{I}}$ (expression (7)) and $\mathbf{Y}$ (the 4×4 transformation matrix formed by the eigenvectors of system (8)). The fact mentioned in item (i) above implies that any vector given by a linear combination of $\ddot{\mathbf{y}}_1$, $\ddot{\mathbf{y}}_2$ and $\ddot{\mathbf{y}}_3$ is also an eigenvector of system (6) and, thus, the sub-system corresponding to the first three rows and columns remains fully populated. In order to characterise the last three rigid-body modes, one must consider the sub-matrix $\ddot{\mathbf{Y}}_{\mathbf{II}}$ (formed by the first three columns of $\ddot{\mathbf{Y}}$) and the transformed matrices $\ddot{\mathbf{C}}$ and $\ddot{X}$ (of dimension 3×3), given by

$$\ddot{\mathbf{Y}}_{\mathbf{II}} = [\ddot{\mathbf{y}}_1 \quad \ddot{\mathbf{y}}_2 \quad \ddot{\mathbf{y}}_3] \qquad \ddot{\mathbf{C}} = \ddot{\mathbf{Y}}_{\mathbf{II}}^{\mathrm{T}}\,\mathbf{C}\,\ddot{\mathbf{Y}}_{\mathbf{II}} \qquad \ddot{\mathbf{X}} = \ddot{\mathbf{Y}}_{\mathbf{II}}^{\mathrm{T}}\,\mathbf{X}\,\ddot{\mathbf{Y}}_{\mathbf{II}} \tag{10}$$

3.4 Determination of the Bending and Axial Extension Modes

Consider now the eigenvalue problem ($\ddot{\mathbf{C}}$ and $\ddot{\mathbf{X}}$ are the transformed matrices in (10))

$$(\ddot{\mathbf{X}} - \lambda_k \ddot{\mathbf{C}})\,\mathbf{y}_k = \mathbf{0} \tag{11}$$

which has *3* eigenvalues λ_k – the *first* is *null*:

$\lambda_k=0$ ($k=1$) corresponds to *one* eigenvector $\dot{\mathbf{y}}_1$ associated with a cross-section *rigid-body* motion with *no* in-plane cross-section *displacements – axial extension mode.*

(ii) $\lambda_2>\lambda_3>0$ correspond to *two* eigenvectors $\mathbf{y}_2$ and $\mathbf{y}_3$ associated with cross-section *rigid-body* motions *with* in-plane cross-section *displacements – major and minor axis bending modes.*

Figure 9 shows the lipped channel section in-plane deformed configurations and warping displacement profiles of the axial extension and major/minor axis bending modes. Finally, one must determine the matrix (of dimension $(n+m+1)\times 3$)

$$\dddot{\mathbf{Y}} = \ddot{\mathbf{Y}}_{\mathbf{II}}\,\mathbf{Y} = \ddot{\mathbf{Y}}_{\mathbf{II}}\,[\mathbf{y}_1 \quad \mathbf{y}_2 \quad \mathbf{y}_3] = [\dddot{\mathbf{y}}_1 \quad \dddot{\mathbf{y}}_2 \quad \dddot{\mathbf{y}}_3] \tag{12}$$

which stems from the product between $\ddot{\mathbf{Y}}_{\mathbf{II}}$ (expression (10)) and $\mathbf{Y}$ (3×3 transformation matrix formed by the eigenvectors of system (11)).

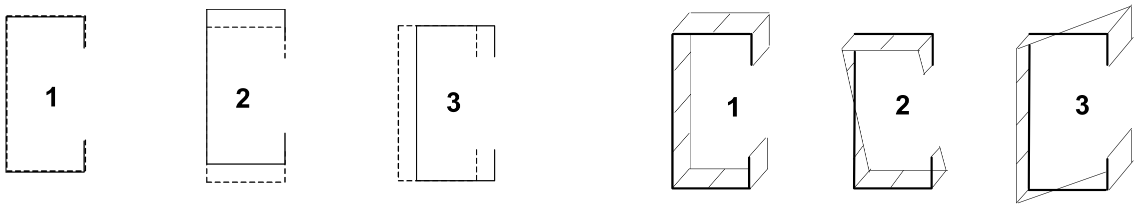

(a) (b)

Figure 9. Lipped Channel Extension and Bending Modes: (a) In-Plane Configurations and (b) Warping Profiles

3.5 Modal Form of GBT Equations

Finally, assembling matrices $\dddot{\mathbf{Y}}$, $\ddot{\mathbf{Y}}$ and $\dot{\mathbf{Y}}$ into a $(n+m+1)\times(n+m+1)$ global transformation matrix leads to

$$\tilde{\mathbf{Y}} = \left[\mathbf{Y}_{\mathrm{III}} \quad \mathbf{Y}_{\mathrm{II}} \quad \mathbf{Y}_{\mathrm{I}}\right] = \left[\dddot{\mathbf{y}}_1 \quad \dddot{\mathbf{y}}_2 \quad \dddot{\mathbf{y}}_3 \quad \ddot{\mathbf{y}}_4 \quad \dot{\mathbf{y}}_5 \quad \cdots \quad \dot{\mathbf{y}}_{n+m+1}\right] \tag{13}$$

where each column $\tilde{\mathbf{y}}_k$ corresponds to one of the $n+m+1$ orthogonal *deformation modes*. In the particular case of the lipped channel section shown in Figure 3, the mixed vector $\mathbf{y}$ (*i.e.*, involving warping $\tilde{u}_i$ and flexural $\tilde{w}_j$ displacements) defined by expression (2) has now the modal form

$$\tilde{\mathbf{y}}_k = \{\tilde{u}_1 \quad \tilde{w}_2 \quad \tilde{u}_3 \quad \tilde{w}_4 \quad \tilde{u}_5 \quad \tilde{w}_6 \quad \tilde{w}_7 \quad \tilde{w}_8 \quad \tilde{u}_9 \quad \tilde{w}_{10} \quad \tilde{u}_{11} \quad \tilde{w}_{12} \quad \tilde{u}_{13}\}^{\mathrm{T}} \tag{14}$$

The components of $\tilde{\mathbf{y}}_k$ are (i) the warping displacements at the natural nodes ($\tilde{u}_i$, $i=2, 3, 5, 9, 11$ and 12) and (ii) the flexural displacements at the intermediate nodes ($\tilde{w}_j$, $j=4, 6, 7, 8$ and 10) and lip end nodes ($\tilde{w}_j$, $j=1$ and 13), which define each deformation mode configuration. Note that local-plate modes ($k=7, \ldots, 13$ – see Figure 7) display null warping displacements and that the corresponding vectors $\tilde{\mathbf{y}}_k$ are of the form

$$\tilde{\mathbf{y}}_k = \{\tilde{w}_1 \; 0 \; 0 \; \tilde{w}_4 \; 0 \; \tilde{w}_6 \; \tilde{w}_7 \; \tilde{w}_8 \; 0 \; \tilde{w}_{10} \; 0 \; 0 \; \tilde{w}_{13}\}^T \tag{15}$$

Similarly, the axial extension mode ($k=1$ – see Figure 9(a)) exhibits null flexural displacements and the corresponding vector $\tilde{\mathbf{y}}_1$ is given by ($\tilde{u}_i=1$)

$$\tilde{\mathbf{y}}_1 = \{0 \; \tilde{u}_2 \; \tilde{u}_3 \; 0 \; \tilde{u}_5 \; 0 \; 0 \; 0 \; \tilde{u}_9 \; 0 \; \tilde{u}_{11} \; \tilde{u}_{12} \; 0\}^{\mathrm{T}} \tag{16}$$

All the remaining modes (*i.e.*, bending, torsion and distortional modes – see Figures 6, 8 and 9) are characterised by non-null warping and flexural displacements – the corresponding vectors display the general form given in (14). After completing this task, one obtains the set of $n+m+1$ ("mixed" u-w) eigenvectors, each associated with a specific cross-section *deformation mode*. Then, all four (fully populated) matrices $\mathbf{C}$, $\mathbf{D}$, $\mathbf{B}$ and $\mathbf{X}$ must be transformed by means of the operations

$$\tilde{\mathbf{C}} = \tilde{\mathbf{Y}}^{\mathrm{T}}\,\mathbf{C}\,\tilde{\mathbf{Y}} \qquad \tilde{\mathbf{D}} = \tilde{\mathbf{Y}}^{\mathrm{T}}\,\mathbf{D}\,\tilde{\mathbf{Y}} \qquad \tilde{\mathbf{B}} = \tilde{\mathbf{Y}}^{\mathrm{T}}\,\mathbf{B}\,\tilde{\mathbf{Y}} \qquad \tilde{\mathbf{X}} = \tilde{\mathbf{Y}}^{\mathrm{T}}\,\mathbf{X}\,\tilde{\mathbf{Y}} \tag{17}$$

The components of the transformed matrices $\tilde{\mathbf{C}}$, $\tilde{\mathbf{D}}$, $\tilde{\mathbf{B}}$ and $\tilde{\mathbf{X}}$ are the *cross-section modal mechanical properties*, namely (i) the axial, bending, torsional and warping stiffness values (global modes) and (ii) several less familiar properties with no obvious mechanical meaning (distortional and local-plate modes). The GBT system (4) then acquires the modal form

$$\tilde{\mathbf{C}}\tilde{\boldsymbol{\phi}}_{,xxxx} - \tilde{\mathbf{D}}\tilde{\boldsymbol{\phi}}_{,xx} + \tilde{\mathbf{B}}\tilde{\boldsymbol{\phi}} - \lambda \tilde{W}_m^o \tilde{\mathbf{X}}_m \tilde{\boldsymbol{\phi}}_{,xx} = \mathbf{0} \tag{18}$$

As for the nature of the matrices appearing in Eq. 18, it is worth noting that:

(i) $\tilde{\mathbf{C}}$, $\tilde{\mathbf{D}}$, $\tilde{\mathbf{B}}$ are stiffness matrices concerning generalised warping, torsion and transverse bending (cross-section in-plane deformation), respectively – see the expressions in (5).

(ii) $\tilde{\mathbf{X}}_m$ ($m=1, 2, 3, 4$) are geometric stiffness matrices that account for the influence of the interaction between the longitudinal normal stresses associated with the pre-buckling deformation mode m (stress resultant $\tilde{W}_m^o$) and the in-plane cross-section strains. Moreover, it is also worth noting that the generalised stress resultants $\tilde{W}_m^o$ (deemed uniform along the member length) can be either (ii$_1$) axial compressive forces ($\tilde{W}_1^o=N$), (ii$_2$) major/minor axis bending moments ($\tilde{W}_2^o=M_I$ or $\tilde{W}_3^o=M_{II}$), (ii$_3$) bi-moments ($\tilde{W}_4^o=B$) or (ii$_4$) any combination of the above. The diagonalisation procedure described earlier is only capable of *reducing* the strong coupling of the GBT differential equilibrium equation system (18). However, the non-diagonal symmetric geometric stiffness matrix $\tilde{\mathbf{X}}_m$ always causes mode coupling effects in buckling analyses.

The solution of the eigenvalue problem defined by system (18) is either (i) a closed-form analytical expression satisfying the homogeneous differential equations and associated boundary conditions (*exact* solution, only possible in a few cases) or (ii) yielded by applying a numerical discretisation method, which replaces the member buckling mode by a linear combination of pre-defined shape functions (*approximate* solution, always possible). In the first case, *exact* solutions may only be obtained for simply supported members (end sections locally/globally pinned and free to warp). In such case (the one dealt with in this work), the buckling modes vary longitudinally accordingly to sinusoidal functions of the type

$$\tilde{\phi}_k = d_k sin\left(\frac{n_s \pi x}{L}\right) \tag{19}$$

where n_s is the half-wave number ($n_s=1$ in this work) and L is the member length. The participation of deformation mode k in a cross-section deformed configuration associated with a given buckling mode depends on the ratio between the corresponding $\tilde{\phi}_k$ value and the sum of all such values – obviously, this ratio varies along the member length. Therefore, it seems plausible to quantify the contribution of mode k to the member buckling mode by means of a *participation factor* given by

$$p_k = \frac{\int_0^L \left|\tilde{\phi}_k\right|}{\sum_{i=1}^{n}\left(\int_0^L \left|\tilde{\phi}_i\right|\right)} \tag{20}$$

which correspond to the ratio between the *averages* of $\tilde{\phi}_k$ and of the sum of all modal amplitudes. The GBT-based modal participation diagrams presented in this work are based on this definition. Note that in simply supported members, an alternative participation factor definition involving only the mid-span modal amplitudes can also be used – it yields p_k values that are very similar to the ones obtained with the ratio defined in (20).

4. OVERVIEW OF cFSM

4.1 FSM Essentials

The semi-analytical Finite Strip Method (FSM) was developed to analyse prismatic plated structures (*e.g.*, [11]). The most important features of FSM are (i) discretisation into *strips* (long and narrow rectangular plates), (ii) selection of longitudinal shape functions that constitute (exact or approximate) solutions of the problem, obviously satisfying its boundary conditions, and (iii) the use of polynomial transverse shape functions, as is typically done in FEM (Finite Element Method) applications. These features are responsible for the fact that the FSM (i) involves a significantly smaller number of d.o.f. than the FEM (*i.e.*, requires less input data and computational effort) and (ii) can only be effectively applied to certain types of regular structures (due to the need to pre-define adequate longitudinal shape functions).

Since the advantages of the FSM can be fully exploited when performing buckling analyses of thin-walled members, while its restrictions pose no significant problems (in most cases), this method became popular in the last decades. In buckling applications, the stiffness of each strip stems from a combination of (i) small deflection plate bending (d.o.f. w) and (ii) membrane plane stress (d.o.f. u and v). As for the shape functions adopted, they are (i) standard cubic polynomials for the transverse flexural d.o.f., (ii) linear polynomials for the transverse membrane d.o.f. and (iii) sinusoidal functions in the longitudinal direction. In an individual strip, the plate bending and membrane behaviours are completely uncoupled, even though the assembly of the strips into the member global stiffness matrix causes coupling between the membrane (in-plane) and flexural (out-of-plane) behaviours. Moreover, the choice of longitudinal functions implies that the member end sections are locally/globally pinned and may warp freely − thus, one only obtains solutions for thin- walled member buckling problems exhibiting these classical end support conditions. Note, however, that the FSM is capable of handling more complex end support conditions (not addressed in this work). Finally, note that there at least two FSM codes widely available to the technical/scientific community, namely THIN-WALL [12] and CUFSM [13] − moreover, it is worth mentioning that the cFSM presented and discussed in this work is implemented and available in the latest version of CUFSM [14].

To obtain the buckling modes of a thin-walled member by means of the FSM, one must solve a generalised eigenvalue problem that can be written as

$$\mathbf{K_e \Phi} = \mathbf{\Lambda K_g \Phi} \tag{21}$$

where (i) $\mathbf{K_e}$ and $\mathbf{K_g}$ are the global elastic and geometric stiffness matrices, (ii) $\mathbf{\Phi} = [\boldsymbol{\varphi}_1 \quad \boldsymbol{\varphi}_2 \quad \dots \quad \boldsymbol{\varphi}_m]$ is the eigenvector matrix, (iii) $\mathbf{\Lambda} = diag[\lambda_1, \lambda_2, ..., \lambda_m]$ is the eigenvalue matrix and (iv) $m=4\times n$ is the number of d.o.f. − note that the exact evaluation of $\mathbf{K_e}$ and $\mathbf{K_g}$ is reported in [15].

4.2 Mode Definition

The separation between *global* (G), *distortional* (D), *local* (L) and *other* (O) deformation modes can be carried out through the application of the following three mechanical criteria (Table 4 shows which criteria must be satisfied by the different deformation modes. In the context of the cFSM, “deformation mode” may sometimes mean “deformation mode family” or “deformation mode space” − this was not the case in GBT, where “deformation mode” means a specific cross-section deformed configuration:

(i) Criterion 1. (a) $\gamma_{xy}=0$, *i.e.*, null membrane shear strains, (b) $\varepsilon_x=0$, *i.e.*, null transverse extensions, and (c) the axial displacements v are linear along each wall mid-line (i.e., between two main nodes).

(ii) Criterion 2. (a) $v\neq 0$, i.e., the warping displacement are not null along the whole cross-section, mid-line, and (b) the cross-section is in transverse flexural equilibrium.

(iii) Criterion 3. $\kappa_{xx}=0$, i.e., there is no transverse flexure.

Table 4. Mode definition in cFSM: criteria that must be satisfied by the different deformation modes.

	G modes	**D** modes	**L** modes	**O** modes
Criterion 1 – Vlasov's hypothesis	Yes	Yes	Yes	No
Criterion 2 – Longitudinal warping	Yes	Yes	No	–
Criterion 3– Undistorted section	Yes	No	–	–

4.3 Concept of Constraint Matrices for Modal Decomposition

Implementation of the criteria given in Table 4 is completed through the application constraint matrices for each of the modes that "force" the FSM general displacement field (expressed in terms of *m* d.o.f.) to satisfy the relevant criteria, thus leading to "reduced d.o.f." displacement fields. In order to achieve this goal, one establishes relationships between the nodal displacements of the form

$$\mathbf{d}=\mathbf{R_M d_M} \tag{22}$$

where (i) **d** is a general *m*-element displacement vector, (ii) $\mathbf{d_M}$ is a displacement vector in the reduced space, and (iii) $\mathbf{R_M}$ is the constraint matrix associated with a certain deformation mode and responsible for enforcing deformations in accordance with a set of pre-defined mechanical assumptions (criteria) – note that subscript "M" identifies the deformation mode or modes and may stand for G, D, L, O or GD, GDL, etc. It should be noted that, since the $\mathbf{d_M}$ vector belongs to a "reduced d.o.f." space, it is not necessarily directly associated with the original nodal displacements – instead, $\mathbf{d_M}$ should be viewed simply as a vector in generalised coordinates.

In general, there is an infinite number of vectors satisfying Eq. 22 for a given $\mathbf{R_M}$ constraint matrix, which means that all of them lay in the same vector (or function, to be more precise) *space* – a *sub-space* of the original FSM d.o.f. space. Any such sub-space can be conveniently defined by means of a set of linearly independent *base vectors* – note that the column vectors of $\mathbf{R_M}$ can also be viewed as base vectors. Hence, the vector space defined by the base vectors associated with a given mode (included in the relevant $\mathbf{R_M}$) will also be designated as G, D, L or O space – one may also speak about a GD space (the reunion of the G and D spaces), a GDL space (the reunion of the G, D and L spaces), etc. Naturally, the GDLO space coincides with the original FSM d.o.f. space.

Since a buckling mode shape is itself a displacement field (*i.e.*, eigenvectors are displacement vectors), the constraint given by Eq. 22 may also be applied to $\mathbf{\Phi}$. By introducing (22) into (21) and pre-multiplying by $\mathbf{R_M}^\mathbf{T}$,

$$\mathbf{R_M}^\mathbf{T}\mathbf{K_e R_M \Phi_M}=\mathbf{\Lambda_M R_M}^\mathbf{T}\mathbf{K_g R_M \Phi_M} \tag{23}$$

which can be re-written as

$$\mathbf{K_{e,M}\Phi_M}=\mathbf{\Lambda_M K_{g,M}\Phi_M} \tag{24}$$

an equation that is recognisable as a new eigenvalue problem, now posed in the "reduced (constrained) d.o.f." space spanned by the deformation mode or modes under consideration. In the above expression, $\mathbf{K}_{\mathbf{e,M}}$ and $\mathbf{K}_{\mathbf{g,M}}$ are the linear stiffness and geometric stiffness matrices of the constrained FSM problem.

Since $\mathbf{R}_{\mathbf{M}}$ is an $m \times m_M$ matrix, where m_M is the dimension of the reduced d.o.f. space, $\mathbf{K}_{\mathbf{e,M}}$ and $\mathbf{K}_{\mathbf{g,M}}$ are $m_M \times m_M$ matrices, much smaller than the $m \times m$ $\mathbf{K}_{\mathbf{e}}$ and $\mathbf{K}_{\mathbf{g}}$. Thus, the application of the constraint can be viewed as a form of model reduction. Finally, $\mathbf{\Lambda}_{\mathbf{M}}$ is an $m_M \times m_M$ diagonal matrix containing the eigenvalues associated only with the mode or modes under consideration, and $\mathbf{\Phi}_{\mathbf{M}}$ is the matrix whose columns are the eigenmodes (or buckling modes).

One defines *pure buckling modes* as the solutions of the constrained eigenvalue problem (24), which (i) are also solutions of the *generalised eigenvalue problem* (21), and (ii) satisfy the constraint Eq. 22. The definition of the various $\mathbf{R}_{\mathbf{M}}$ matrices requires different derivations – while $\mathbf{R}_{\mathbf{L}}$ and $\mathbf{R}_{\mathbf{O}}$ can be defined directly, $\mathbf{R}_{\mathbf{G}}$ and $\mathbf{R}_{\mathbf{D}}$ involve two steps: one first defines $\mathbf{R}_{\mathbf{GD}}$, which is then separated into $\mathbf{R}_{\mathbf{G}}$ and $\mathbf{R}_{\mathbf{D}}$.

4.4 Constraint Matrix for GD Modes

As a direct consequence of Criteria 1 and 2, any displacement vector belonging to the GD space can be expressed by its axial displacements – note that the above criteria are *a priori* assumptions of the GBT analyses. In other words, the warping displacements unambiguously define the whole member displacement field. Moreover, since the warping displacements are linear between two main nodes (*i.e.*, within a wall), it suffices to know the axial translations of all main nodes to determine the entire displacement field. Then, (i) it is possible to develop a mathematical relationship between the longitudinal displacement d.o.f. and all the remaining ones, (ii) the number of GD base vectors is equal to the number of main nodes and (iii) any set of n_{main} independent warping displacement profiles may be adopted as a base vector system.

4.5 Separation of G and D Modes

To separate the G and D spaces, it is necessary to perform an additional transformation inside the GD space. Mathematically, one seeks a $\mathbf{H}_{\mathbf{GD}} = \begin{bmatrix}\mathbf{H}_{\mathbf{G}} & \mathbf{H}_{\mathbf{D}}\end{bmatrix}$ transformation matrix that can be used to describe any $\mathbf{d}_{\mathbf{GD}}$ in terms of a modal basis formed by a system of base vectors that has the G and D vectors separated, *i.e.*, such that

$$\mathbf{d}_{\mathbf{GD}} = \begin{bmatrix}\mathbf{H}_{\mathbf{G}} & \mathbf{H}_{\mathbf{D}}\end{bmatrix}\begin{bmatrix}\mathbf{d}_{\mathbf{G}} \\ \mathbf{d}_{\mathbf{D}}\end{bmatrix} \tag{25}$$

The column vectors of $\mathbf{H}_{\mathbf{G}}$ and $\mathbf{H}_{\mathbf{D}}$ are, in fact, warping displacement profiles associated with the global and distortional modes. Once $\mathbf{H}_{\mathbf{G}}$ and $\mathbf{H}_{\mathbf{D}}$ are defined, they can be used to calculate the global and distortional buckling modes separately. By considering Eqs 22 and 25, any displacement vector in the *global* or *distortional* space can be expressed as $\mathbf{d}=\mathbf{R}_{\mathbf{G}}\mathbf{d}_{\mathbf{G}}$ or $\mathbf{d}=\mathbf{R}_{\mathbf{D}}\mathbf{d}_{\mathbf{D}}$, where $\mathbf{R}_{\mathbf{G}}$ and $\mathbf{R}_{\mathbf{D}}$ are the constraint matrices for the G and D spaces, defined as

$$\mathbf{R}_{\mathbf{G}}=\mathbf{R}_{\mathbf{GD}}\mathbf{H}_{\mathbf{G}} \qquad \mathbf{R}_{\mathbf{D}}=\mathbf{R}_{\mathbf{GD}}\mathbf{H}_{\mathbf{D}} \tag{26}$$

4.6 Constraint Matrix for the G Modes

Since the constraint matrix for the global modes is expressed as $\mathbf{R}_{\mathbf{G}}=\mathbf{R}_{\mathbf{GD}}\mathbf{H}_{\mathbf{G}}$ and $\mathbf{R}_{\mathbf{GD}}$ is already defined through the satisfaction of Criteria 1 and 2, the only task remaining is to find $\mathbf{H}_{\mathbf{G}}$. Recalling that the columns of **H** are nodal warping displacements, one must define warping displacement profiles specifically for the G modes. Since, by definition, these modes exhibit no cross-section distortion (see Criterion 3 and keep in mind that the longitudinal displacement profile stems from the pre-defined shape functions), one has *4* global modes, associated with the four cross-section rigid-body motions: (i) longitudinal translation, (ii) two transverse translations and (iii) rotation about the member longitudinal axis passing through the cross-section shear centres – obviously, these deformation modes coincide with the GBT rigid-body ones – their transverse and warping displacement profiles were already shown in Figures 9(a)-(b) and 8(a)-(b).

4.7 Constraint Matrix for the D Modes

Since there is no direct definition currently available for distortional modes, their warping displacement profiles are obtained by imposing that they must be linear independent with respect to the global modes. Independence with the global modes is achieved by satisfying the orthogonality condition

$$\int v_i(x)v_j(x)t(x)\,dx = 0 \tag{27}$$

where the integration is carried over the whole cross-section, $t(x)$ is the wall thickness and $v_i(x)$ and $v_j(x)$ are arbitrary warping functions belonging to the G and D spaces, respectively. Note that the above expression is also employed in the GBT approach, see the first term in matrix **C**, given in (5) (recall that u are warping displacements in the GBT notation). The imposition of the above orthogonality conditions requires some mathematical operations that are not discussed here (see [4, 5]) but lead to the determination of the $\mathbf{H_D}$ matrix, *i.e.*, the warping displacement profiles characterising the distortional modes. Then, the corresponding constraint matrix is given by $\mathbf{R_D}=\mathbf{R_{GD}}\mathbf{H_D}$.

4.8 Constraint Matrix for the L Modes

The constraint matrix $\mathbf{R_L}$ can be defined through the direct application of the criteria defining the L modes, given in Table 4. First, one uses the fact that L modes need not satisfy Criterion 2, which means that (i) all the warping displacements are null and (ii) transverse flexural equilibrium may be violated. At the same time, the enforcement of Criterion 1 leads to a strict relationship between the longitudinal displacements of the main nodes and the transverse displacements of the internal main nodes, which implies that the L modes have no internal main node displacements (only rotations may occur). Then, the consideration of Criterion 1(a) makes it clear that the local u displacements must be null for all strips, *i.e.*, no membrane shear strains can occur in the member. Moreover, only displacements in the local w direction (*i.e.*, normal to the plate strip) are allowed at the nodes that can move (*i.e.*, all but the main nodes 2 to n_{main}-1). Since no other restrictions apply to the L modes, the allowable generalised displacements include (i) local w-direction translations of the external main nodes, (ii) local w-direction translations of the sub-nodes and (iii) rotations of all nodes – all remaining nodal generalised displacements are fully restrained.

A possible and rather convenient way to define the $\mathbf{R_L}$ matrix is to apply FEM-like (or FSM-like) base functions with unit value at appropriate w or θ local d.o.f. and null value at all remaining d.o.f. This procedure is illustrated in Figure 10, for the lipped channel considered throughout this paper (see Figure 3 – *6* main nodes and *5* sub-nodes) – all FEM-like local base functions are shown and one should note that this cFSM discretisation (with *5* sub-nodes) replicates the previous GBT discretisation (with *7* intermediate nodes).

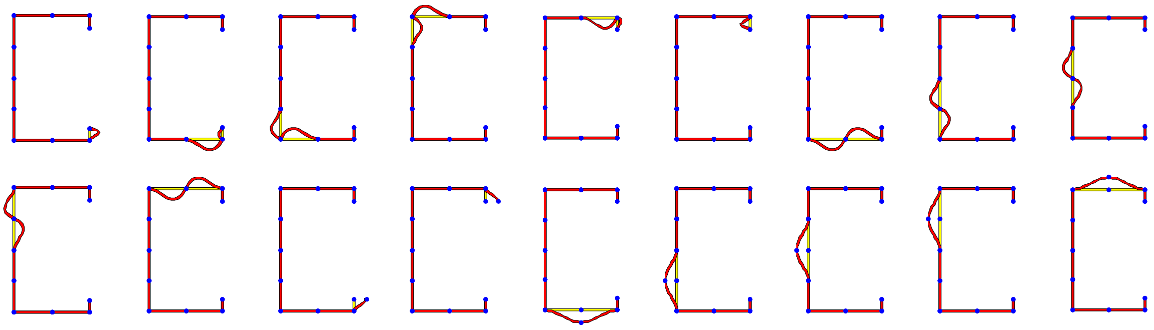

Figure 10. FEM-Like (Natural) Base Functions Considered for the L Modes

4.9 Constraint Matrix for the O Modes

The O-modes are characterised by the fact that they do not satisfy Criterion 1, *i.e.*, (i) the in-plane (membrane) transverse extensions and/or shear strains are not null and (ii) non-linear warping displacement profiles may exist within a wall width (*i.e.*, between adjacent main nodes) – the latter condition is strongly related to the existence of membrane shear strains. The direct application of the above considerations makes it a straightforward task to define a system of independent vectors associated with unit transverse extensions and unit shear strains, as has been done similarly in the GBT approach [16] – since both modes may occur in any strip, the number of the corresponding base vectors must equal $2\times(n-1)$ (twice the number of strips). It is worth mentioning, however, that these types of deformation modes were only considered in the context of GBT-based *post-buckling analysis* (*i.e.*, they were never included in buckling analyses).

It should still be mentioned that this approach, although easy to explain and understand, has a non-negligible drawback: the resulting O space has overlaps with the previously defined sub-spaces (G, D and L spaces). Thus, in order to avoid such overlaps, the O base vectors can be defined in such a way that they must necessarily be orthogonal to the G, D and L ones – the use of modern numerical tools (*e.g.*, definition of null spaces in MATLAB [17]) render the performance of this task quite straightforward.

4.10 Orthogonal Modes

Any pure mode space (G, D, L, etc.) can be defined by means of a multitude of base vector systems. However, it is certainly convenient to define special base vector systems, among which orthogonal systems have considerable practical importance. A convenient way to perform the orthogonalisation is to solve the constrained eigenvalue problem defined by Eq. 24, assuming that the applied stresses are uniformly distributed along the cross-section mid-line. The columns of the resulting $\mathbf{\Phi_M}$ matrix contain the unit member pure buckling modes, which are obviously orthogonal to each other and span the sub-space under consideration – thus, any $\mathbf{d_M}$ vector belonging to the reduced d.o.f. space can be expressed as a linear combination of them,

$$\mathbf{d_M} = \mathbf{\Phi_M c_M} \tag{28}$$

where (i) $\mathbf{\Phi_M}$ is the $m_M \times m_M$ matrix of the orthogonal modes and (ii) the $\mathbf{c_M}$ vector components define the contributions of the various modes (*i.e.*, $\mathbf{c_M}$ is the *modal coordinate vector*). It is worth noting that the $\mathbf{\Phi_M}$ matrix can also be interpreted as a transformation matrix that, when applied to $\mathbf{R_M}$, effectively transforms the solution of the constrained eigenvalue problem into the unit-member axial mode base system, but expressed in the original nodal d.o.f. space – indeed, the incorporation of (28) into (22) leads to

$$\mathbf{d} = \mathbf{R_M d_M} = \mathbf{R_M \Phi_M c_M} = \mathbf{C_M c_M} \tag{29}$$

which demonstrates that any nodal displacement vector **d** lying in a given M sub-space can be expressed as a linear combination of the $\mathbf{C_M}$ matrix column vectors – this matrix, which should not be confused with the GBT **C** matrix, is just a transformed form of the corresponding restraint matrix **R** whose columns are orthogonal and expressed in the original FSM nodal displacement space.

Once the orthogonal modes are defined both in the reduced and original d.o.f. spaces, any pure mode space can still be further reduced by eliminating one or more of those modes (*i.e.*, columns of the $\mathbf{\Phi_M}$ or $\mathbf{C_M}$ matrices) – if only one mode is kept, this procedure ultimately leads to *individual buckling modes*.

It should be noted that, in general, the $\mathbf{R_M}$ matrices (and, therefore, also their orthogonal versions $\mathbf{\Phi_M}$ or $\mathbf{C_M}$) depend on the member length. However, it is possible to introduce length-independent orthogonal modes, by carrying out the above orthogonalisation procedure for a unit-length member, where "unit-length" is defined so that one has $k_r=r\pi/a=1$, which leads to a real length equal to $a=r\pi$, where r is the number of sinusoidal half-waves considered. The advantage of a length-independent orthogonal base system is that it is unique for a specific cross-section and, thus, directly comparable with the GBT modes. Figures 11 and 12 show the G, D and first nine L orthogonal modes, for a unit-length member with the illustrative lipped channel section.

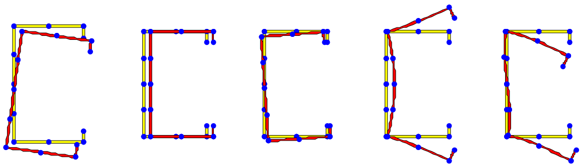

Figure 11. Global and Distortional Length-Independent Orthogonal Modes (In-Plane Deformed Shapes)

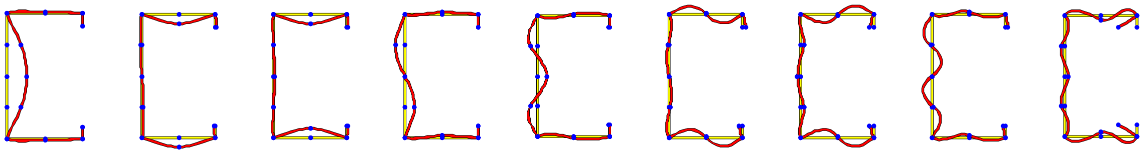

Figure 12. First Nine Local Length-Independent Orthogonal Modes (In-Plane Deformed Shapes)

4.11 Mode Contribution Calculation

The most important use of the orthogonal (deformation) modes is the calculation of modal contributions to a general unconstrained member buckling mode (or even to any other member deformed configuration). The formulae required to perform this task, in the context of the entire GDLO space, can be obtained directly from Eq. 29 (one just needs to replace subscript M with GDLO). However, since the $\mathbf{C_{GDLO}}$ matrix columns are eigenvectors that can be arbitrarily scaled, the calculation of the modal contributions (participations) requires the definition of a suitable *normalisation*.

Various normalisation procedures are possible (*e.g.*, see [18]), the one adopted here is called *work normalisation*, since it is based on the work done by a unit force on the deformed (orthogonal) shape. To achieve this, one incorporates an orthogonal mode $\boldsymbol{\varphi}$ into the eigenvalue problem defined by Eq. 21 and pre-multiplies both sides by $\boldsymbol{\varphi}^\mathbf{T}$, thus leading to

$$\frac{1}{\lambda}\boldsymbol{\varphi}^{\mathbf{T}}\mathbf{K_e}\boldsymbol{\varphi} = \boldsymbol{\varphi}^{\mathbf{T}}\mathbf{K_g}\boldsymbol{\varphi} \tag{30}$$

where the right hand side is the work done by the unit compressive force (if $\mathbf{K_g}$ is calculated for a unit stress evenly distributed along the cross-section mid-line), which becomes unitary through the appropriate scaling of the $\boldsymbol{\varphi}$ vector. Then, if one uses the normalised orthogonal mode vectors to construct the linear combination defined in Eq. 29, the elements of vector $\mathbf{c_{GDLO}}$ provide the contributions of the deformation modes to the member buckling mode – the corresponding *relative contribution* of a particular mode can be obtained by means of the expression

$$|c_i| \Big/ \sum_{all} |c_i| \tag{31}$$

where c_i denotes the component of the $\mathbf{c_{GDLO}}$ vector under consideration. Similarly, the joint contribution of a family of deformation modes (*i.e.*, global, distortional or local modes) is defined as

$$\sum_{mode} |c_i| \Big/ \sum_{all} |c_i| \tag{32}$$

Concerning the orthogonality, it is worth noting that it is always satisfied within a given mode family, as a direct consequence of their derivation. However, modes belonging to different families are not necessarily orthogonal to each other – this fact accounts for a small degree of arbitrariness in the calculation of the modal contributions (participations). However, since experience shows that the modes calculated according to the above-described procedure are nearly orthogonal, the calculation of the modal participating factors is certainly applicable in practice – note that the GBT deformation modes also are not fully orthogonal displacement fields.

5. ILLUSTRATIVE NUMERICAL RESULTS

5.1 General Comparison

In order to enable a better grasp of the concepts and procedures presented before, GBT and cFSM are next employed to investigate the *single-wave* buckling behaviour of thin-walled lipped channel columns and beams having (i) cross-section dimensions $b_{web}=100\ mm$, $b_{flange}=60\ mm$, $b_{lip}=10\ mm$, $t=2\ mm$, (ii) pinned (locally and globally) and free to warp end sections, and (iii) the (steel) elastic constants $E=210\ GPa$ and $\nu=0.3$. The results obtained are presented in (i) Figures 13 and 14 (*columns*) and (ii) Figures 15 and 16 (*beams* under major axis bending) and will be discussed next.

The curves depicted in Figures 13 and 15 provide the variation of the buckling load ($\lambda_b P \equiv P_b$) or buckling moment ($\lambda_b M_Z \equiv M_b$) with the member length L (represented in logarithmic scale), obtained by means of analyses that include (i) only individual deformation modes or combinations of a few of them (top curves and corresponding dots) or (ii) all the deformation modes simultaneously (bottom thick solid curves and black dots) – the curves and dots provide GBT and cFSM results, respectively. Concerning the top curves and dots, one has (i) dotted curves and thick white dots for the local-plate buckling results, (ii) dashed-dotted curves and grey dots for the distortional buckling results and (iii) thin solid curves and thin white dots for the global buckling results. As for Figures 14 (columns) and 16 (beams), they make it possible to visualise the "degree of participation" of each individual mode (GBT) or each mode family (cFSM) in the member buckling mode.

After observing Figures 13 and 14, dealing with the *column* buckling behaviour, one concludes that:

(i) As usual, local-plate buckling dominates for short columns (*L<18 cm*), distortional buckling prevails for intermediate-length columns (*18<L<75 cm*) and flexural-torsional or flexural buckling modes occur for the longer columns (*L>250 cm*). In the length range *75<L<250 cm*, the columns buckle in distortional-flexural-torsional mixed modes.

(ii) There is a virtually perfect agreement between the results yielded by the GBT (thick solid curve) and cFSM (black dots) that take into account all deformation modes simultaneously. As far as the local-plate and distortional minima are concerned, the differences between the buckling load values provided by the two approaches are *0.25%* and *0.80%* respectively. Concerning global buckling, the differences are of the same order of magnitude (*e.g.*, *0.78%* for *L=226 cm*).

(iii) Despite the fact that the GBT modal participation diagram provides more detailed information concerning the contribution of each deformation mode to the column buckling mode (actually, the cFSM diagram shows the relative contributions of the deformation mode families L, D, G and O), the two diagrams are quite similar. The minor discrepancies detected in Figure 14 can be attributed to the different definitions of the GBT and cFSM participation factors.

Finally, the results presented in Figures 15 and 16, concerning the *beam* buckling behaviour, show that:

(i) Now, local-plate buckling only dominates for very short beams (*L<10 cm*), while lateral-torsional buckling prevails for the long ones (*L>250 cm*). As for the beams with small-to-intermediate lengths (*10<L<90cm*), they buckle in distortional modes. Lastly, the buckling modes of the not-too-long beams (*90<L<250 cm*) are mixed distortional-flexural-torsional – however, the distortional contribution tends to be smaller than in the columns.

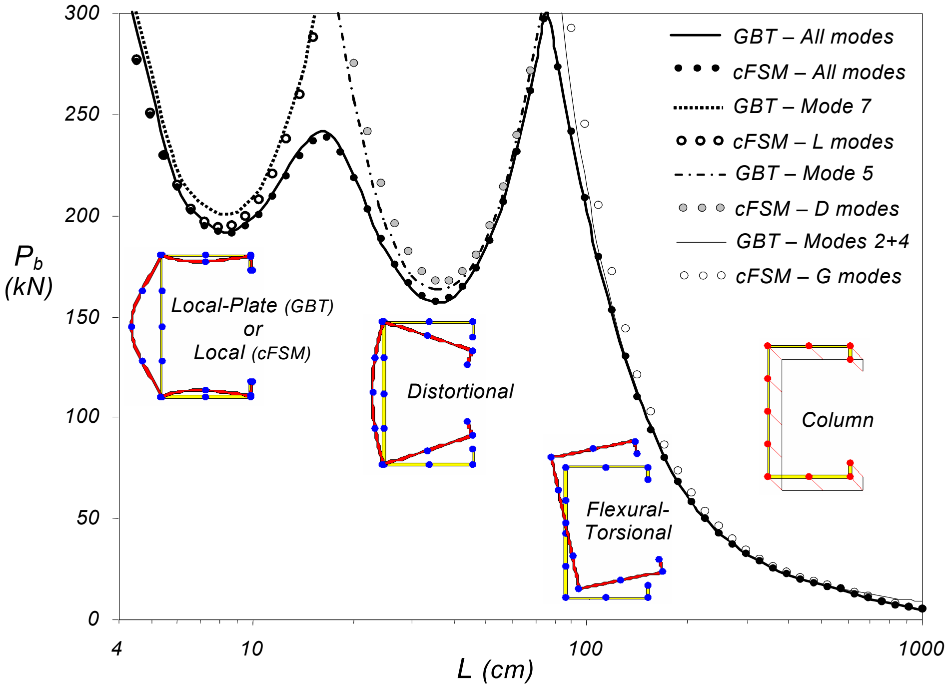

Figure 13. Variation of the Buckling Load P_b with the Column Length L

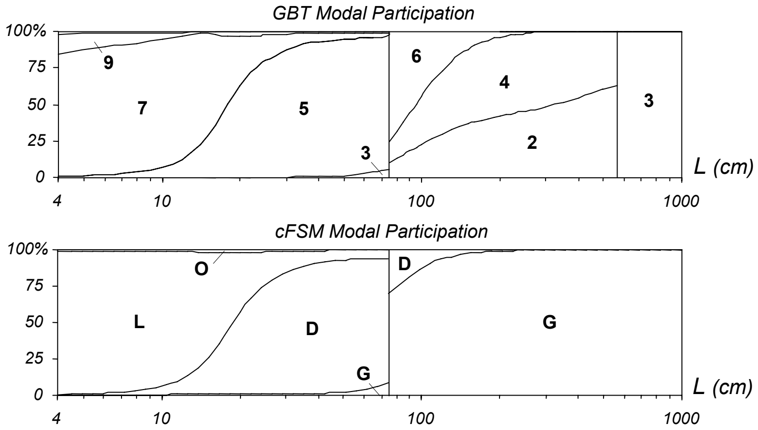

Figure 14. Column GBT and cFSM Modal Participation Diagrams

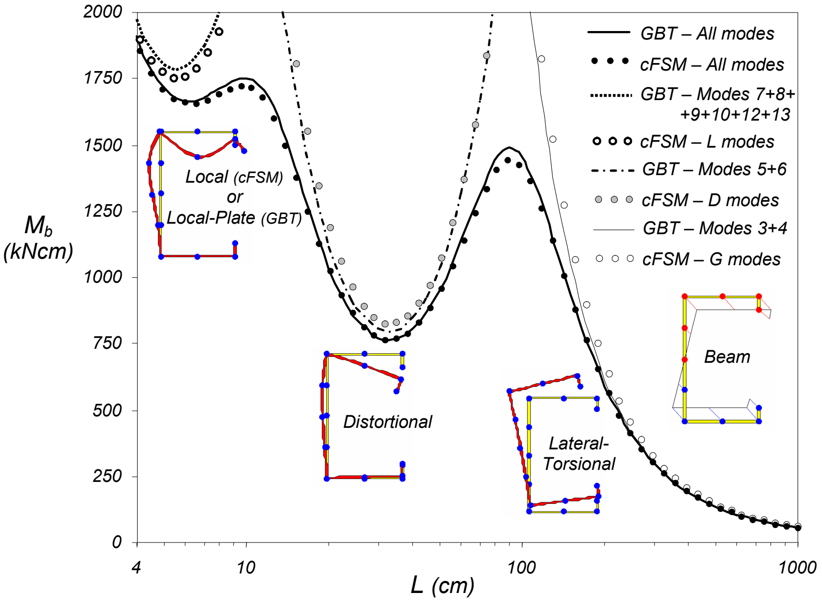

Figure 15. Variation of the Buckling Moment M_b with the Beam Length L

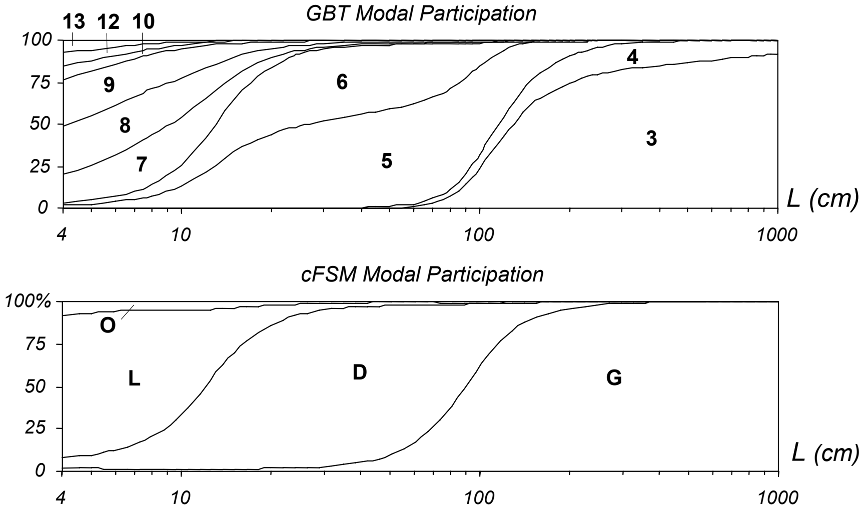

Figure 16. Beam GBT and cFSM Modal Participation Diagrams

(ii) The results provided by the GBT and cFSM all-mode analyses (thick solid curve and black dots) are again very close. In particular, it is worth mentioning that the buckling moment differences are equal to *1.35%* and *0.25%* for the local-plate and distortional minima, respectively, and similarly small for the beams buckling in lateral-torsional modes (*e.g.*, *0.56%* for $L=298.4\ cm$).

(iii) Once more, the GBT and cFSM modal participation diagrams are rather similar. Note that the cFSM L-mode, D-mode and G-mode domains practically coincide with the reunions of the GBT sub-domains associated with deformation modes **7**+**8**+**9**+**10**+**12**+**13**, **5**+**6** and **3**+**4**, respectively. Only the cFSM O-mode domain has no GBT counterpart, due to the fact that no shear or transverse extension modes were included in the GBT analyses – this may explain the small differences between the two sets of M_b values (the cFSM ones are slightly lower).

5.2 The Role of Kinematic and Constitutive Modelling

During the course of this comparative study between the GBT and cFSM analyses of the buckling behaviour of unbranched open thin-walled members, it was found that some of the small discrepancies detected in the numerical results yielded by the two approaches can be traced back to basic mechanical assumptions embedded in them. Indeed, while cFSM logically views the member as an assembly of interconnected plates (the FSM is based on folded-plate theory), GBT tries to accommodate, as much as possible, the classical beam model format – these different perspectives have two main consequences:

(i) Concerning the kinematic (strain-displacement) relation dealing with the longitudinal extensions, cFSM takes into account the non-linear terms associated with all the displacements. On the other hand, GBT does not incorporate the non-linear term stemming from the longitudinal displacements (the same as the classical beam models) – however, note that this term is only non-negligible for members with very small lengths, of very little (if any) practical interest.

(ii) Concerning the plane stress constitutive (stress-strain) relationship, cFSM adopts the exact one, which implies that the longitudinal normal stresses and extensions are related by $E/(1-\nu^2)$. On the other hand, GBT employs an approximate 2D constitutive relation that replaces the above elastic constant by the Young's modulus E, in order to replicate the 1D stress state characterising the classical beam theories – in the case of steel ($\nu=0.3$), this corresponds to a 9% increase that is directly reflected in the member stiffness values associated with applied longitudinal normal stresses. This stiffness increase can also be conveniently interpreted as an "artificial" increase of the corresponding cross-section geometric properties, namely the area A, the major/minor moments of inertia I and the warping constant C_w.

In the case of the global flexural buckling of thin-walled columns, the first author [19] showed that the above mechanical assumption differences are responsible for buckling load drops that (i) increase as the column length decreases and (ii) are only non-negligible for very short columns – nevertheless, the cFSM critical stresses tend to $E/(1-\nu^2)$ as the column length approaches zero, a value that is in sharp contrast with the infinite one yielded by GBT (and also by the Euler formula).

In view of what was mentioned in the previous paragraphs, it becomes clear that the effect of the membrane axial stiffness change (*i.e.*, E vs. $E/(1-\nu^2)$) on the member buckling stress depends on how relevant is the role played by the applied longitudinal normal stresses – thus, it seems logical to anticipate the following, concerning the relation between the GBT and cFSM pure-mode (G, D and L) buckling stresses:

(i) The larger differences correspond to column global flexural (F) buckling, since only longitudinal normal stresses are involved.

(ii) In column torsional (T) or flexural-torsional (FT) buckling and in beam lateral-torsional (LT) buckling, the relevant stresses are longitudinal normal (flexure and warping torsion) and shear (Saint-Venant torsion) – the relative importance of the shear stresses obviously grows with the participation of torsion in the column/beam buckling mode. This means that the differences must be smaller than in the F buckling case (*9%*), particularly so in T buckling.

(iii) Since distortional (D) buckling involves cross-section distortion and wall bending, relevant shear and transverse normal stresses are present, together with the longitudinal normal ones. Therefore, the differences will again be smaller than *9%*.

(iv) Since local (L) buckling is associated exclusively with wall (transverse) bending, only transverse normal stresses are involved. Thus, the differences between cFSM and GBT buckling stresses are bound to be rather small.

In order to assess the correctness of the above predictions, one presents next numerical results concerning simply supported lipped channel steel ($E=210\ MPa$ and $\nu=0.3$) columns and beams with (i) cross-section dimensions $b_{web}=150\ mm$, $b_{flange}=60\ mm$, $b_{lip}=15\ mm$, $t=2\ mm$ and (ii) lengths comprised between *10* and *10000 mm*. The curves and dots depicted in Figures 17 to 19 provide the GBT and cFSM buckling stresses corresponding to the G, D and L buckling of columns (first two modes) and beams (first mode only) – note that this is only possible due to the unique modal nature of the two approaches. The observation of these numerical results prompts the following remarks (note that the length is represented in logarithmic scale):

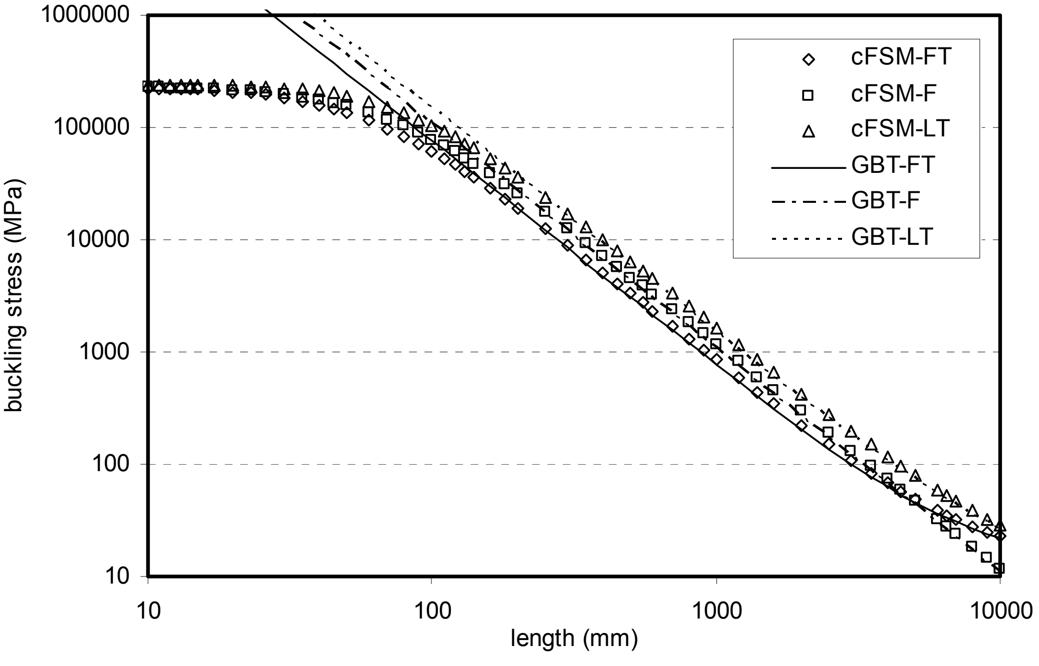

Figure 17. Buckling Stresses Associated with Column and Beam Global Buckling

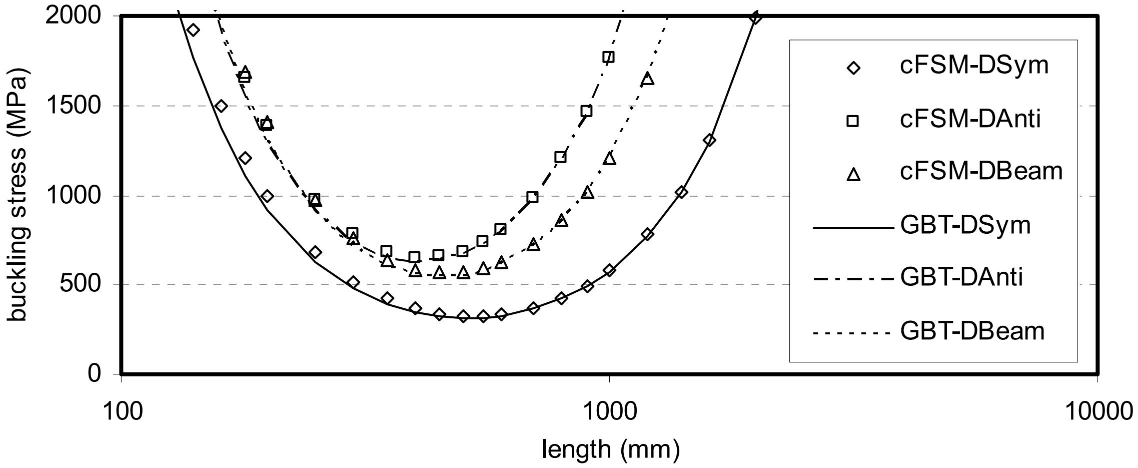

Figure 18. Buckling Stresses Associated with Column and Beam Distortional Buckling

(i) As expected, the cFSM global buckling stresses converge to $E/(1-\nu^2)$ as the column/beam length approaches zero. Naturally, the differences are only non-negligible for small lengths – *e.g.*, for F buckling one has *1%* and *3%* differences for column lengths of *700 mm* and *400 mm*. (Since global buckling very rarely, if ever, governs in this small length range, this fact has little practical relevance.)

(ii) There is another expected discrepancy between the GBT and cFSM global buckling stresses, which is hardly visible in Figure 17 but can be clearly observed in Figure 20, which shows the percentage differences between the two sets of values (calculated with respect to the cFSM ones): the cFSM values are always higher than their GBT counterparts for long columns/beams – since global buckling controls for this length range, these differences have some practical relevance. Moreover, one notices that the differences (ii_1) remain practically constant, at *9%*, for the column F buckling and (ii_2) decrease with the length for column FT and beam LT buckling (*4%* and *6%*, for a *10 m* length) – this is due to the growing relevance of the shear stresses (in comparison with the longitudinal normal ones).

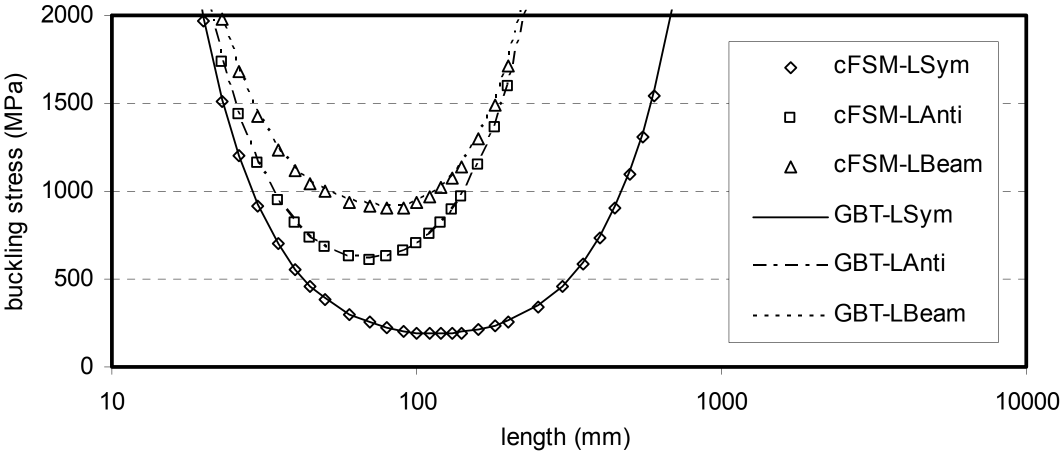

Figure 19. Buckling Stresses Associated with Column and Beam Local Buckling

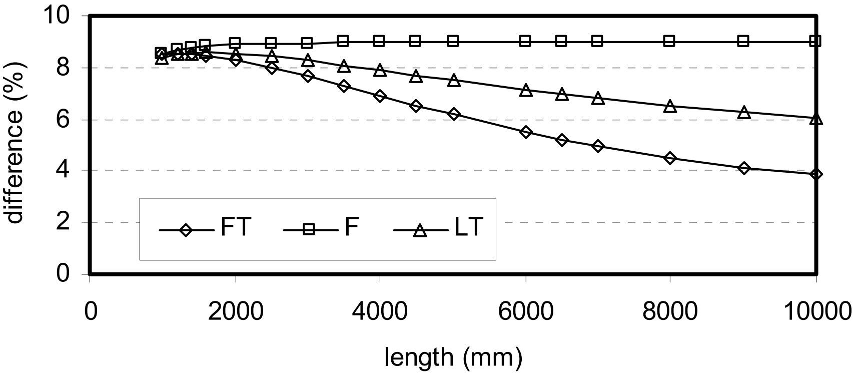

Figure 20. Percentage Difference Between the GBT and cFSM Global Buckling Stresses

(iii) The buckling stress curves displayed in Figure 18 concern the column symmetric (first) and anti-symmetric (second) distortional modes, as well as the beam only distortional mode. As correctly anticipated, the cFSM buckling stresses are always higher than the GBT ones. The percentage differences (again calculated with respect to the cFSM values) are shown in Figure 21 and one observes that they decrease with the column/beam length – a fairly abrupt drop (*8%* to *1%*) in the *150-800 mm* length range, followed by a much smoother one (*1%* to about *0%*) up to a length close to *1600 mm*.

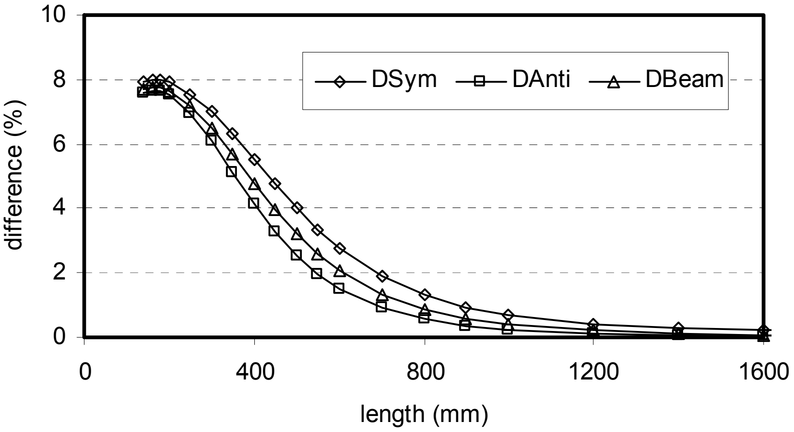

Figure 21. Percentage Difference Between the GBT and cFSM Distortional Buckling Stresses

(iv) As in the distortional case, the buckling stress curves displayed in Figure 19 concern the column symmetric and anti-symmetric (first and second) local modes, together with the beam only one. Once more as predicted, the differences between the cFSM and GBT buckling stresses are very small, regardless of the column/beam length – they never exceed *1%* and would probably be even lower if one considered more refined discretisations (*i.e.*, more sub/intermediate nodes). Note that the interpretation of intermediate nodes (GBT) and sub-nodes (cFSM), as well as the associated base functions, are slightly different – this implies that GBT and cFSM discretisations involving the same number of intermediate/sub nodes do not provide exactly the same approximation. Since, in theory, the GBT and cFSM buckling stresses should be identical (the differences would stem only from numerical reasons), it is a bit surprising to observe that the GBT values are consistently higher than the cFSM ones. This is most likely due to the fact that the GBT local-plate deformation modes are not as "purely local" as the cFSM ones (the GBT orthogonalisation procedure slight spoils their "purity" [1]) – this may be viewed as "additional constraints" that lead to a (minute) increase in the member wall transverse bending stiffness.

6. CONCLUSION

It is well known that unbranched open thin-walled members are generally prone to three types of instability: global, distortional and local (or local-plate) buckling. The proper identification of a given (pure or mixed) buckling mode nature is crucial, since the member post-buckling behaviour, imperfection-sensitivity and ultimate strength strongly depend on it – moreover, the design methods to estimate the member load-carrying capacity also rely heavily on its buckling behaviour nature. Currently, there are two approaches to analyse the buckling behaviour of unbranched open thin-walled members that are able to formally decompose and identify the different buckling phenomena: Generalised Beam Theory (GBT) and the constrained Finite Strip Method (cFSM).

GBT originated as an extension of classical beam theory that was enhanced to include (i) additional warping displacement fields consistent with distortional buckling (first) and (ii) transverse bending displacement fields consistent with local-plate buckling (later). On the other hand, the cFSM has its roots in the semi-analytical FSM, whose plate strips were subsequently constrained to "force" the buckling mode nature – it is based the same mechanical assumptions adopted by GBT (to enhance its displacement fields), which are treated as constraints applied to the FSM general displacement fields. While the GBT formulation does not depend on the longitudinal displacement fields, which makes it applicable to members exhibiting a variety of end support conditions, the cFSM is a specialisation of the semi-analytical FSM method (and not of a general purpose finite element) and, therefore, only provides solutions for simply supported members.

The GBT solution is embodied in a generalised version of the member differential equation system (see (4)) and the simultaneous diagonalisation of two of its matrices (**C** and **B**) constitutes a key step in the GBT derivation – it makes it possible to transform the solution from a nodal space to a *modal* one (see (18)). A very important consequence of these formulation and transformation is the generalisation of the cross-section geometrical properties beyond A (area), I (second moment of area) and C_w (warping constant) to cover distortional and local-plate buckling – this is a unique GBT feature. After performing the above simultaneous matrix diagonalisation, the ensuing **C**, **D** and **B** matrices describe the cross-section mechanical behaviour (linear elastic stiffness), while the geometric stiffness matrix **X** depends on the applied stresses.

The cFSM follows from a typical FSM stability solution (see (21)), where the linear elastic stiffness ($\mathbf{K_e}$) and geometric ($\mathbf{K_g}$) stiffness matrices are formulated on the basis of plate strips containing in-plane membrane (plane stress) and classical Kirchhoff plate bending behaviours. The associated general deformation fields may be constrained, as shown in Eqs. 23 and 24, thus providing a decomposition of the general solution space into G, D, L, and O sub-spaces. A full transformation to a modal basis, analogous to the GBT one, can be applied through the consideration of orthogonal modes for a member of unit length – this procedure was described in subsection 4.10 but not employed to obtain the numerical results presented in this work.

Both GBT and the cFSM provide means to assess the contributions (or participation factors) of the various deformation modes in the member buckling mode shapes – while GBT uses the average of the modal amplitudes along the member length, various options are possible within the cFSM – among them, the one similar to GBT quantifies the contribution of a given mode family as the ratio between the work done by a unit axial force on that mode family and the total work of the same unit force associated with the member buckling mode under consideration. The illustrative numerical results presented and discussed in the paper showed that both GBT and the cFSM are able to decompose the buckling modes and identify the associated modal contributions – as far as the buckling analysis of simply supported thin-walled members, GBT and cFSM offer essentially the same capabilities. Although the numerical results yielded by the two approaches were shown to correlate very well, the small differences detected prompted a further investigation aimed at understanding their origin. It was found that the (fairly minute) discrepancies stem from the different modelling of (i) the kinematic (strain-displacement) relation dealing with the longitudinal extensions and (ii) the plane stress constitutive (stress-strain) relationship − the most relevant effect is the change in membrane axial stiffness from E (GBT) to $E/(1-\nu^2)$ (cFSM). Moreover, it was possible to predict, and validate numerically, how these modelling differences influence the various member buckling stresses − the effect (i) is most prominent in column flexural buckling (buckling stress differences of *9%* in steel members), (ii) is also felt (but to a lesser extent) in column flexural-torsional, beam lateral-torsional and column/beam distortional buckling, and (iii) practically does not exist in column/beam local buckling.

ACKNOWLEDGEMENTS

The research work reported in this paper was conducted under the financial support of the TéT Port-5/2005 Hungarian-Portuguese Intergovernmental Science and Technology Cooperation Program, the OTKA K62970 project of the Hungarian Scientific Research Fund and the János Bolyai Research Scholarship of the Hungarian Academy of Sciences − this financial support is gratefully acknowledged.

REFERENCES

[1] Schardt, R., “Verallgemeinerte Technische Biegetheorie”, Springer Verlag, Berlin, 1989, (German).

[2] Camotim, D., Silvestre, N., Gonçalves, R. and Dinis, P.B., “GBT Analysis of Thin-Walled Members: New Formulations and Applications”, Thin-Walled Structures: Recent Advances and Future Trends in Thin-Walled Structures Technology, J. Loughlan (Ed.), Canopus Publishing, Bath, 2004, pp. 137-168.

[3] Camotim, D., Silvestre, N., Gonçalves, R. and Dinis, P.B., “GBT-based Structural Analysis of Thin-walled Members: Overview, Recent Progress and Future Developments”, Advances in Engineering Structures, Mechanics and Construction (SMCD 2006 − Waterloo, 14-17/6), Pandey, M., Xie, W.-C., Chu, L. (Eds.), Springer, pp. 187-204, 2006.

[4] Ádány, S. and Schafer, B.W., “Buckling Mode Decomposition of Single-Branched Open Cross-Section Members via Finite Strip Method: Derivation”, Thin-Walled Structures, 2006, Vol. 44, No. 5, pp. 563-584.

[5] Ádány, S. and Schafer, B.W., “Buckling Mode Decomposition of Single-Branched Open Cross-Section Members via Finite Strip Method: Application and Examples, Thin-Walled Structures, 2006, Vol. 44, No. 5, pp. 585-600.

[6] Ádány, S. and Schafer, B.W., “A Full Modal Decomposition of Thin-Walled, Single-Branched Open Cross-Section Members via the Constrained Finite Strip Method, Journal of Constructional Steel Research, 64 (1), pp. 12-29, 2008. (doi:10.1016/j.jcsr.2007.04.004).

[7] Ádány, S., Silvestre, N., Schafer, B.W. and Camotim, D., “Buckling Analysis of Unbranched Thin-Walled Members: Generalised Beam Theory and Constrained Finite Strip Method”, Book of Abstracts of III European Conference on Computational Mechanics: Solids, Structures and Coupled Problems in Engineering (III ECCM − Lisboa, 5-9/6), C.A.M. Soares, et al. (Eds.), Springer, Lisboa, 2006, Vol. 679 (Full Paper in CD-ROM Proceedings).

[8] Ádány, S., Silvestre, N., Schafer, B.W. and Camotim, D., “Buckling Analysis of Unbranched Thin-Walled Members Using cFSM and GBT: A Comparative Study”, Proceedings of International Colloquium on Stability and Ductility of Steel Structures (SDSS 2006 − Lisboa, 6-8/9), Camotim, D. Silvestre, N. Dinis, P.B. (Eds.), IST Press, 2006, pp. 205-212.

[9] Ádány, S., Silvestre, N., Schafer, B.W. and Camotim, D., “On the Identification and Characterisation of Local, Distortional and Global Buckling Modes in Thin-Walled Members Using the cFSM and GBT Approaches”, Proceedings of the 6th International Conference on Steel & Aluminium Structures (ICSAS’07 – Oxford, 24-27/7), Beale, R. (Ed.), 2007. pp. 760-767.

[10] Silvestre, N., “Generalised Beam Theory: New Formulations, Numerical Implementation and Applications, Ph.D. Thesis, IST-Technical University of Lisbon, 2005. (Portuguese)

[11] Cheung, Y.K. and Tham, L.G., The Finite Strip Method, CRC Press, Boca Raton, 1998.

[12] Papangelis, J.P. and Hancock, G.J, Cross-Section Analysis and Finite Strip Analysis and Direct Strength Design of Thin-Walled Structures – THIN-WALL (version 2.1), Center for Advanced Structural Analysis, School of Civil and Mining Engineering, University of Sydney, 2005. (Its website is http://www.civil.usyd.edu.au/case/thinwall)

[13] Schafer, B.W., “Elastic Buckling Analysis of Thin-Walled Members (FSM) – CUFSM (Version 2.6), Johns Hopkins University, 2003. (Freely Available at the Website http://www.ce.jhu.edu/bschafer/)

[14] Schafer, B.W., “Elastic Buckling Analysis of Thin-Walled Members (cFSM) – CUFSM (Version 3.12), Johns Hopkins University, 2006. (Freely Available at the Website http://www.ce.jhu.edu/bschafer/)

[15] Schafer, B.W. and Ádány, S., “Buckling Analysis of Cold-Formed Steel Members Using CUFSM: Conventional and Constrained Finite Strip Methods”, Proceedings of 18th International Specialty Conference on Cold-Formed Steel Structures (Orlando, 26-28/10), 2006, LaBoube, R., Yu, W.W. (Eds.), pp. 39-54.

[16] Silvestre, N. and Camotim, D., “Non-Linear Generalised Beam Theory for Cold-Formed Steel Members”, International Journal of Structural Stability and Dynamics, 2003, Vol. 3, No. 4, pp. 461-490.

[17] Mathworks Inc., MATLAB Users Guide (Version 7), Natick, USA, 2005, (http:/www.mathworks.com)

[18] Ádány, S., Silvestre N., Schafer, B.W. and Camotim, D., “Buckling Mode Identification of Thin-Walled Members: A Comparison Between cFSM and GBT Approaches”, Fifth International Conference on Coupled Instabilities in Metal Structures (CIMS 2008 – Sydney, 23-25/6), 2008, pp. 249-256

[19] Ádány, S., “Flexural Buckling of Thin-Walled Columns: Discussion on the Definition and Calculation”, Proceedings of International Colloquium on Stability and Ductility of Steel Structures (SDSS 2006 – Lisboa, 6-8/9), Camotim, D., Silvestre, N., Dinis, P.B. (Eds.), IST Press, pp. 249-258, 2006.